ABSTRACT

Title of dissertation: QUANTIFYING THE ORGANIZATION AND DYNAMICS OF EXCITABLE SIGNALING NETWORKS

Leonard Joseph Campanello
Doctor of Philosophy, 2020

Dissertation directed by: Professor Wolfgang Losert
Department of Physics

The transmission of extracellular information through intracellular signaling networks is ubiquitous in biology—from single-celled organisms to complex multicellular systems. Via signal-transduction machinery, cells of all types can detect and respond to biological, chemical, and physical stimuli. Although studies of signaling mechanisms and pathways traditionally involve arrays of biochemical assays, detailed quantification of physical information is becoming an increasingly important tool for understanding the complexities of signaling. With the rich datasets currently being collected in biological experiments, understanding the mechanisms that govern intracellular signaling networks is becoming a multidisciplinary problem at the intersection of biology, computer science, physics, and applied mathematics.

In this dissertation, I focus on understanding and characterizing the physical behavior of signaling networks. Through analysis of experimental data, statistical modeling, and computational simulations, I explore a characteristic of signaling networks called excitability, and show that an excitable-systems framework is broadly

applicable for explaining the connection between intracellular behaviors and cell functions.

One way to connect the physical behavior of signaling networks to cell function is through the structural and spatial analyses of signaling proteins. In the first part of this dissertation, I employ an adaptive-immune-cell model with a key activation step that is both promoted and inhibited by a microns-long, filamentous protein complex. I introduce a novel image-based bootstrap-like resampling method and demonstrate that the spatial organization of signaling proteins is an important contributor to immune-cell self regulation. Furthermore, I use the bootstrap-like resampling to demonstrate that the location of contact points between signaling proteins can provide mechanistic insight into how signal regulation is accomplished on the single-cell level. Finally, I probe the excitable dynamics of the system with a Monte Carlo simulation of nucleation-limited growth and degradation. Using the simulations, I show that careful balance between simulation parameters can elicit a tunable response dynamic.

The spatiotemporal dynamics of signaling components are also important mediators of cell function. One key readout of the connection between signaling dynamics and cell function is the behavior of the cytoskeleton. In the second part of this dissertation, I use innate-immune-cell and epithelial-cell models to understand how a key cytoskeletal component, actin, is influenced by topographical features in the extracellular environment. Engineered nanotopographic substrates similar in size to typical extracellular-matrix structures have been shown to bias the flow of actin, a concept known as esotaxis. To measure this bias, I introduce a generaliz-

able optical-flow-based-analysis suite that can robustly and systematically quantify the spatiotemporal dynamics of actin in both model systems. Interestingly, despite having wildly different migratory phenotypes and physiological functions, both cell types exhibit quantitatively similar topography-guidance dynamics which suggests that sensing and responding to extracellular textures is an evolutionarily-conserved phenomena.

The signaling mechanisms that enable actin responses to the physical environment are poorly understood. Despite experimental evidence for the enhancement of actin-nucleation-promoting factors (NPFs) on extracellular features, connecting texture-induced signaling to overall cell behavior is an ongoing challenge. In the third part of this dissertation, I study the topography-induced guidance of actin in amoeboid cells on nanotopographic textures of different spacings. Using optical-flow analysis and statistical modeling, I demonstrate that topography-induced guidance is strongest when the features are similar in size to typical actin-rich protrusions. To probe this mechanism further, I employ a dendritic-growth simulation of filament assembly and disassembly with realistic biochemical rates, NPFs, and filament-network-severing dynamics. These simulations demonstrate that topography-induced guidance is more likely the result of a redistribution, rather than an enhancement, of NPF components.

Overall, this dissertation introduces quantitative tools for the analysis, modeling, and simulations of excitable systems. I use these tools to demonstrate that an excitable-systems framework can provide deep, phenomenological insights into the character, organization, and dynamics of a variety of biological systems.

QUANTIFYING THE ORGANIZATION AND DYNAMICS OF EXCITABLE SIGNALING NETWORKS

by

Leonard Joseph Campanello

Dissertation submitted to the Faculty of the Graduate School of the
University of Maryland, College Park in partial fulfillment
of the requirements for the degree of
Doctor of Philosophy
2020

Advisory Committee:
Professor Wolfgang Losert, Advisor and Chair
Professor John T. Fourkas, Dean's Representative
Professor Michelle Girvan
Professor Brian C. Schaefer
Professor Arpita Upadhyaya

Dedication

For Dad and Poppop. I miss you very much.

Acknowledgments

I owe my deepest gratitude to many people who have made this thesis possible. You have all played important roles in my life during my career as a graduate student, and I will cherish our experiences together forever.

Thank you to my advisor, Professor Wolfgang Losert. Your enthusiasm for science is contagious and inspirational. Thank you for providing support and guidance over the past several years, and for giving me the opportunity to work on challenging and interesting projects. It has been a pleasure to work with you.

Thank you to members of my thesis committee: Professor John Fourkas, Professor Michelle Girvan, Professor Arpita Upadhyaya, and Professor Brian Schaefer. John, thank you for your guidance at our weekly subgroup meetings. Michelle, thank you for your fervent support of students in the COMBINE program and for your dedication to teaching, especially PHYS 615. Brian, thank you for collaborating with me and Wolfgang on interesting problems over the past several years.

Thank you to all past and present members of the Losert Lab. Thank you especially to Dr. Rachel M. Lee for your dedication to good scientific practice; Qixin Yang for helpful and fun conversations; Professor Gabriel Frank for your example of balancing work and life; Drs. B. U. Sebastian Schmidt and Kate M. O'Neill for your post-doctoral guidance; Drs. Joshua Parker and Can Guven for your help; Dr. Yang Shen, Dr. Desu Chen, and Zackery Benson for being the best officemates; Abby Bull and Matt Hourwitz for our collaborations; and Sylvester Gates, Nick Mennona, Corey Herr, and Stephanie Noel for all the fun and camaraderie. Thank

you also to non-Losert-lab members, especially Dr. Maria Traver for your guidance.

Thank you to all of my friends whose continuous support and encouragement I frequently relied on. Thank you especially to Alexander, Amanda, Ava, and Abigail Proctor; Allen, Anna, and April Tan; Yidan Wang; Mikel and Erik Marshall; Marco Sagliocca; Prahalad Reddy; Bob Scherne and family; and Ark Latt.

Thank you also to the Auteri, Ferguson, and Gallagher families for your support and encouragement, especially Jim, Irene, Jimmy, Ashley, Sean, and Brayden.

Thank you to my siblings: Christine, Anthony, and Richard. You have each inspired me in one way or another to continue working towards completing this goal. I am incredibly proud of all that you continue to achieve and I look forward to celebrating your continued success.

Thank you to my grandparents: Alfio and Elaine Scammacca. Your support of academic achievement from a very early age was inspirational, and it continues to play an important role in the success of your children and grandchildren.

Thank you to my parents: Leonard and Pauline Campanello. This would have not been possible without your dedication and encouragement, and I am very grateful for you providing the four of us with the best life that you possibly could.

Finally, thank you so much to my wife, Alexis. Your love, encouragement, and support were essential all of these years. I cannot imagine being able to finish graduate school without you. Also, I would be remiss if I didn't mention our dog, Cora. You keep us on our toes, literally. We appreciate that you don't let us sit still for more than 1–2 hours at a time. Your companionship could not be repaid even with a lifetime of dog treats, but we will try anyway.

Table of Contents

List of Figures

List of Abbreviations

Dicty	*Dictyoselium Discoideum*
cAMP	Cyclic adenosine monophosphate
TCR	T-cell receptor
NF-κB	Nuclear factor kappa-light-chain-enhancer of activated B cells
Bcl10	B-cell lymphoma/leukemia 10
Carma1	Caspase-recruitment-domain-containing membrane-associated guanylate kinase protein-1
Malt1	Mucosa-associated lymphoid tissue lymphoma translocation protein 1
CBM	Carma1/Malt1/Bcl10
NPFs	Nucleation-promoting factors
ECM	Extracellular matrix
FHN	FitzHugh-Naguno model
iSIM	Instant-Structured-Illumination Microscope
IVM	Intravital microscopy
LoG	Laplacian of Gaussian
MAP	Multiphoton Absorption Polymerization
PIV	Particle Image Velocimetry
STICS	Spatiotemporal Image Correlation Spectroscopy

Chapter 1: Introduction

Cells actively detect and respond to physical, chemical, and biological cues in the extracellular environment. Amoeboid *Dictyostelium discoideum* (Dicty) sense chemical gradients to migrate towards nutrients [1], and immune cells respond to biochemical agonists and collagen structures in the extracellular matrix to respond to potential sites of pathogen invasion [2].

The transmission of extracellular information is carried out by complex intracellular signaling networks. In Dicty, membrane sensors detect increased cross-cell concentrations of the chemoattractant cAMP (cyclic adenosine monophosphate) and the internal signal-transduction machinery reorients the cytoskeleton towards the direction of highest cAMP concentration [3]. Similarly, bioelectric sensors in epithelial cells sense wound-induced electric fields that override other guidance cues to close the wound [4]. Although mechanisms by which cells detect, transmit information, and respond to extracellular stimuli are often studied at a biochemical level, biophysical information regarding intracellular signaling networks, such as the geometry, organization, and spatiotemporal dynamics of network components, can also provide testable, and often simpler, explanations of cell behavior.

Many intracellular signaling networks exhibit properties of an excitable sys-

tem. Excitability is the phenomenon in which the behavior of a system can rapidly transition between different dynamic states, such as steady-state equilibrium, oscillations, and propagating waves. Excitable behavior is often observed in biological systems across spatiotemporal scales, from multicellular, microsecond-long neuron-firing patterns [5], to micron-scale, minute-long polymerization and depolymerization of cytoskeletal proteins [6].

The excitable nature of biochemical signaling pathways can lead to complex, nonlinear relationships between input signals and cell function. On the whole-cell scale, T-cell-receptor activation in immune cells results in digital responses (i.e., the cell responds in an all-or-nothing manner) [7], and competing excitatory and inhibitory signals in Dicty result in whole-cell polarization [3]. Within these cells, the nonlinear dynamics of biochemical signaling networks play a role in response dynamics: amplification of T cell receptor (TCR) signals in immune cells occurs via interactions between signaling proteins [8], which may be responsible for digital responses, and the polymerization-depolymerization dynamics of the cytoskeleton can be modulated by slight changes in biochemical concentrations [9].

Coupled with the excitable behavior of signaling networks, the ability of cells to quickly and efficiently respond to stimuli indicates that signaling networks are at or near critical points between two or more dynamic states. Indeed, criticality-induced behavior may be responsible for cytoskeletal organization [10] and dynamics [11], and can also induce structural changes to intracellular protein complexes via phase separation [12]. This tendency towards criticality could allow for the maximum amount of information to be encoded in the network [13].

The self-organized critical states of intracellular signaling networks also make cells sensitive to subtle changes in the extracellular environment. Dicty can detect and respond to changes in cAMP concentration as small as 10^{-3} nM/μm [14], and cytoskeletal dynamics can be tuned via the texture of the extracellular environment [15, 16] or small changes to chemical concentrations of signaling proteins [9]. Cell sensitivity to extracellular conditions also extends beyond nearby physical and chemical perturbations. For example, numerous ion pumps and gap junctions build up a potential difference across the cell membrane, and make the cell sensitive to the external electrical environment [17]. This capability plays a role in physiological functions such as adaptive immunity [18]. Changes to the dynamic behavior of cells before and after small extracellular perturbations have many similarities with systems undergoing a phase transition, such as the adjustment of parameters in a forest-fire model near a critical point [19].

The sensory mechanisms within excitable intracellular signaling networks can be harnessed in a variety clinical applications. Potential differences across the cell membrane can help accelerate wound healing [4] and can be engineered to control diabetes upon stimulation from bioelectronic devices [20]; chemical activation or inhibition of immune-cell signals can help inform the development of cancer immunotherapies [21]; and extracellular textures can steer the function of stem cells [22, 23] and help to reveal metastatic potential in cancers [24].

Biochemical models of signaling networks provide frameworks to understand cell behavior. Gene-inactivation studies have elucidated the necessity of different signaling proteins for the activation of immune cells [25], and drug-induced changes

to biochemical feedback loops modulate the cytoskeleton during migration [9]. Further, more physical inputs can be integrated into biochemical models to explain changes in signal transduction. For example, substrate stiffness leads to changes in immune-cell activation [26, 27], substrate-fiber density can modulate stem-cell differentiation [23] and morphology [28], and extracellular nanostructures can guide cell migration [29] and facilitate more efficient cytoskeletal polymerization [16].

Understanding the mechanisms that govern the integrated physical and biochemical characteristics of intracellular signaling networks is now a multidisciplinary problem at the intersection of biology, computer science, physics, and applied mathematics. In this dissertation, I focus on the spatial organization, excitable self assembly and disassembly mechanisms, and multiscale spatiotemporal dynamics of excitable signaling networks. Integrating physical characteristics with biochemical models of signaling networks requires detailed quantification of physical information; thus, I introduce a variety of quantitative measures and techniques to shed light on spatial and dynamic characteristics of physical information.

One important system that operates in a highly critical state with a signaling network that integrates both biochemical and physical information is the effector T cell. Within the immune system, effector T cells actively respond to pathogenic stimuli to activate other immune cells, attack virus-infected cells, and suppress ongoing activation and autoreactivity (the cause of autoimmune diseases). The activity of individual effector T cells is regulated by a complex biochemical signaling network that is initiated at the membrane-bound TCR and results in the nuclear translocation of the transcription factor NF-κB. Termination of NF-κB activation is a crucial

mechanism to maintain healthy homeostasis; improper NF-κB regulation has been associated with primary immunodeficiency disorders [30–32], cancer [33], and autoimmune diseases [34, 35]. Thus, the TCR-to-NF-κB signaling pathway contains many regulatory mechanisms [36, 37]. In Chapter 3, I assess the spatial organization, assembly, and degradation of a key protein in the TCR-to-NF-κB signaling network and discuss how spatial colocalization between signaling components and an excitable-systems framework can help elucidate the mechanisms that ensure rapid immune responses yet prevent ongoing immune-system activation.

Spatial organization, assembly-disassembly characteristics, and excitability are also important aspects of the mechanical machinery within the cytoskeleton. Cells, including immune cells, encounter a range of physical conditions in the extracellular environment while carrying out normal functions. These conditions have been shown to influence cell signaling and function. However, cell responses to extracellular environments *in vivo* are difficult study systematically due to issues of consistency and reproducibility. In contrast, *in vitro* studies designed to elucidate the influence of the extracellular environment on cell signaling can be more carefully controlled and replicated. For example, nanoscale ridges and sawteeth can modulate cell migration [24, 29, 38], morphology [28], and signaling [39], and the stiffness of the substrate can influence TCR activation [40] and T-cell signaling [27]. In Chapter 4, I introduce a novel quantification method to systematically analyze the spatiotemporal dynamics and assembly-disassembly mechanisms of the cell cytoskeleton across length scales and timescales. Although this method was initially developed to study assembly and disassembly mechanisms, the model is generalizable for the quantifi-

cation of the spatiotemporal dynamics of cytoskeleton-associated signaling proteins that are both upstream to and downstream from actin in the signaling network.

Despite the ubiquity of extracellular textures *in vivo* and experimental evidence that textures modulate cytoskeletal dynamics, the mechanisms by which texture can bias both small-scale signaling networks and cell-scale behaviors is not well understood. One way to probe changes in cytoskeletal signaling on extracellular topography is through computational simulations. In Chapter 5, I employ the quantitative tools from Chapter 4 for the systematic comparison of experimentally derived actin dynamics in Dicty with those in a dendritic-growth model of filament assembly and disassembly with realistic biochemical rates, nucleation-promoting factors (NPFs), and filament-network-severing dynamics [41]. To probe real actin dynamics, Dicty is imaged on differently spaced nanoridges centered around the characteristic length scale of actin protrusions ($\sim$2 μm) [29]. Recent evidence has shown that the activity of cytoskeletal signaling components can be enhanced on high-curvature substrates [15, 16]; thus, nanotopographic ridges in the simulations are mimicked via the enhancement of nucleation-promoting factors in striped patterns. I show that systematic experiments and simulations of topography-induced guidance provides a robust framework for the probing the mechanisms which lead to texture sensing.

The tools that I developed to characterize and quantify structures and dynamics of intracellular signaling networks can also be applied to the analysis of dynamic systems *in vivo*. In Chapter 6, I measure and characterize actin activity during the epithelial-to-mesenchymal transition *in vivo*, a key step in cancer metastasis. I

demonstrate that cells that detach from cancerous tumors, which are thus suspended in collagen-rich matrices, exhibit highly variable and protrusive dynamics compared to cells which remain attached to the tumor.

The tools that I developed for measuring and characterizing spatial organization, waves and oscillations, and excitable-systems dynamics are broadly applicable to other systems. For example, the methods I introduce in Chapters 4 and 5 to study assembly and disassembly mechanisms can be generalized to quantify the spatiotemporal dynamics of cytoskeleton-associated signaling proteins that are both upstream and downstream from actin in the cytoskeletal signaling network. In Chapter 7, I discuss the different quantification techniques presented in this dissertation and provide an outlook regarding how these methods could be applied in future studies of excitable signaling networks.

Chapter 2: Background

2.1 Excitable Systems

2.1.1 Mathematics of Excitable Systems

Excitability is observed in a wide variety of biological systems across spatiotemporal scales, from intracellular and minutes-long cascades in biochemical signaling networks to multicellular and microseconds-long firing in neurons. Excitability is characterized by the rapid switching of system evolution between different dynamic states such as a "rest"state, an "excited"state (e.g., periodic excitations or traveling waves), and a refractory period during which excitations cannot occur [42].

The FitzHugh-Nagumo (FHN) model is an instructional example of how excitable behavior can be induced in media that must undergo a quiescent recovery period between excitations [43]. For a given excitation readout $v(t)$ (e.g., membrane voltage in neurons, filament length of signaling complexes, speed or position of cytoskeletal waves), and recovery or refractory variable $w(t)$, an FHN system evolves

according to the coupled differential equations

$$\begin{aligned} \dot{v}(t) &= v(t) - \frac{1}{3}v^3(t) - w(t) + V_{ext} \\ c\dot{w}(t) &= v(t) + a - bw(t). \end{aligned} \tag{2.1}$$

The constants a, b, and c are chosen empirically and V_{ext} is an external perturbation on $v(t)$.

An FHN system can dynamically evolve in a variety of ways, including steady-state equilibrium, a single-spike dynamic, and an oscillatory dynamic state (all seen in Figure 2.1). The excitability characteristic of the system is contained within the balance among parameters. If the external activation of the system is not sufficiently large then the system will not reach an excited state (Figure 2.1A), a concept known as "digital activation". Conversely, if the system undergoes slight changes due to external perturbations, dynamic evolution of the system can rapidly change character, such as the transition from a single-spike dynamic to an oscillatory state (Figure 2.1B).

Excitability is indicative of a system being near a phase transition, referred to as the system being at or near a critical point. Noncritical systems can still display complex dynamics, but a perturbation on a noncritical system may cause a response to differ in strength but not in character. Meanwhile, a critical system that is perturbed in slightly different ways can evolve in drastically different manners. As a result, excitable systems allow for highly nonlinear relationships to arise between system inputs (e.g., signals, perturbations, textures) and outputs (e.g., cell

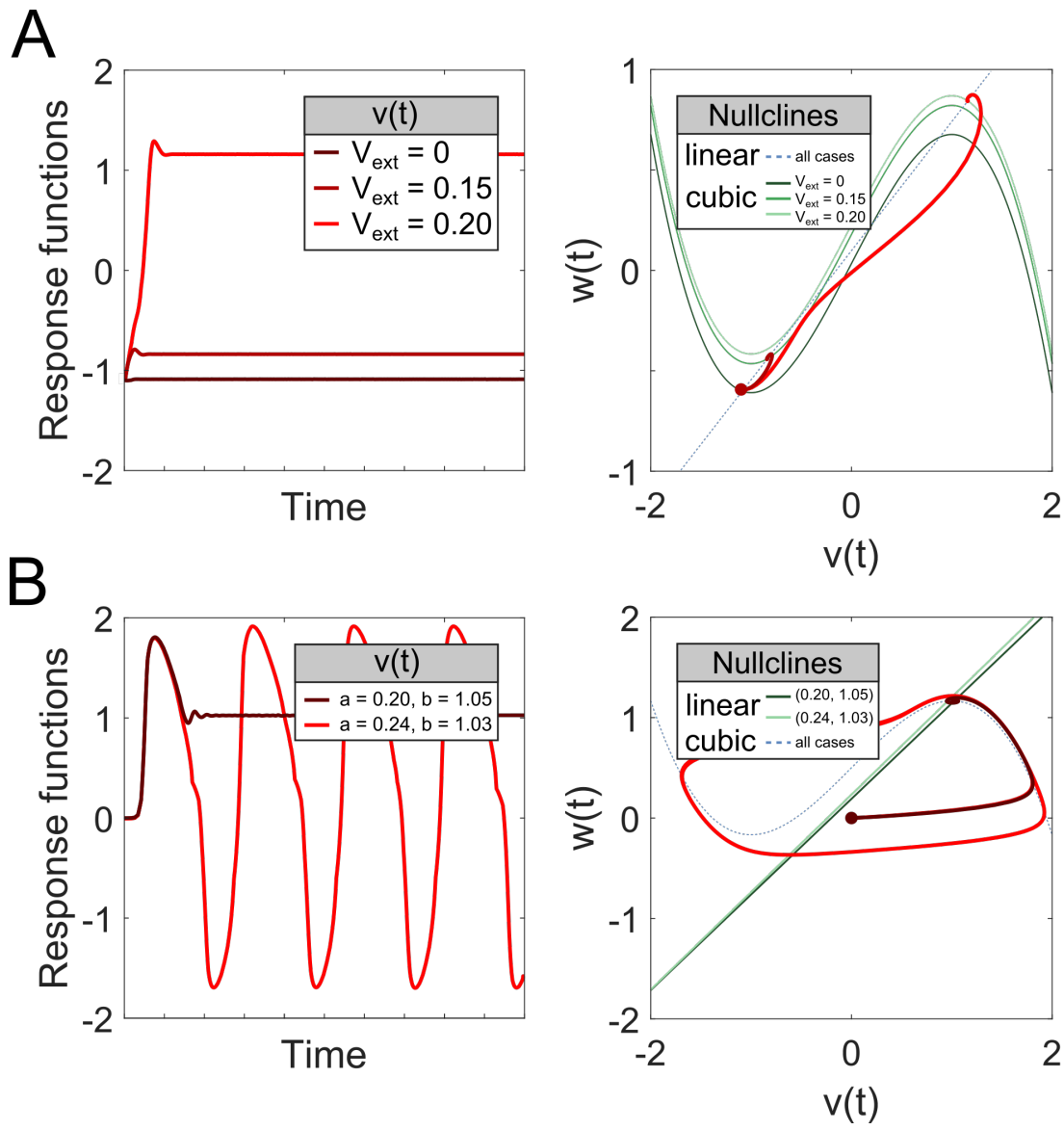

Figure 2.1: Excitability in the FitzHugh-Naguno model. (A) An FHN model with parameters $a = 0.1$, $b = 1.5$, and $c = 1.6$. External perturbations were set at $V_{ext} = 0$, 0.15, and 0.20. $V_{ext} = 0$ and 0.15 were insufficient to switch the system into an excited state whereas $V_{ext} = 0.2$ was, a concept known as digital activation. (B) Two FHN models with slightly different parameters. Dark red: $a = 0.2$, $b = 1.05$, $c = 10$, and $V_{ext} = 0.5$, which has a single-spike dynamic evolution. Light red: $a = 0.24$, $b = 1.03$, $c = 10$, and $V_{ext} = 0.5$, which has an oscillatory-state dynamic evolution. The images were created by Leonard Campanello for use in this dissertation.

function).

2.1.2 Models and Simulations of Excitable Systems

Models and simulations of dynamic systems can capture excitable and critical behavior. A cellular automaton that is instructional in studies of criticality is the Abelian sandpile model [44]. Although Abelian sandpiles display complex dynamics such as fractal-pattern generation, these models are not amenable to recreating biologically-relevant time-series phenomena.

Another class of models that exhibit self-organized criticality and phase transitions are forest-fire models. First introduced as one- or two-parameter models that exhibit self-organized criticality [45], forest-fire models contain a grid of locations (i.e., pixels) that represent "trees"or small coarse-grained regions of a forest: 0 is empty and 1 represents the presence of a tree. If a tree is on fire, the tree will "burn"(the value will be switched from 1 to 0) and the fire will also spread to nearby trees. Thus, the typical rules of a forest fire model are: (1) all cells containing burning trees are set to 0; (2) fire from a burned tree spreads to all neighboring trees; (3) infrequently and randomly there is a "lightning strike"in a random cell and, if occupied by a tree, that tree is set on fire; and (4) empty cells have a probability of growing into a tree.

Standard forest-fire models are capable of displaying different dynamic characteristics based on small changes to control parameters (Figure 2.2A). Furthermore, modified forest-fire models have also been adapted to undergo phase transitions near

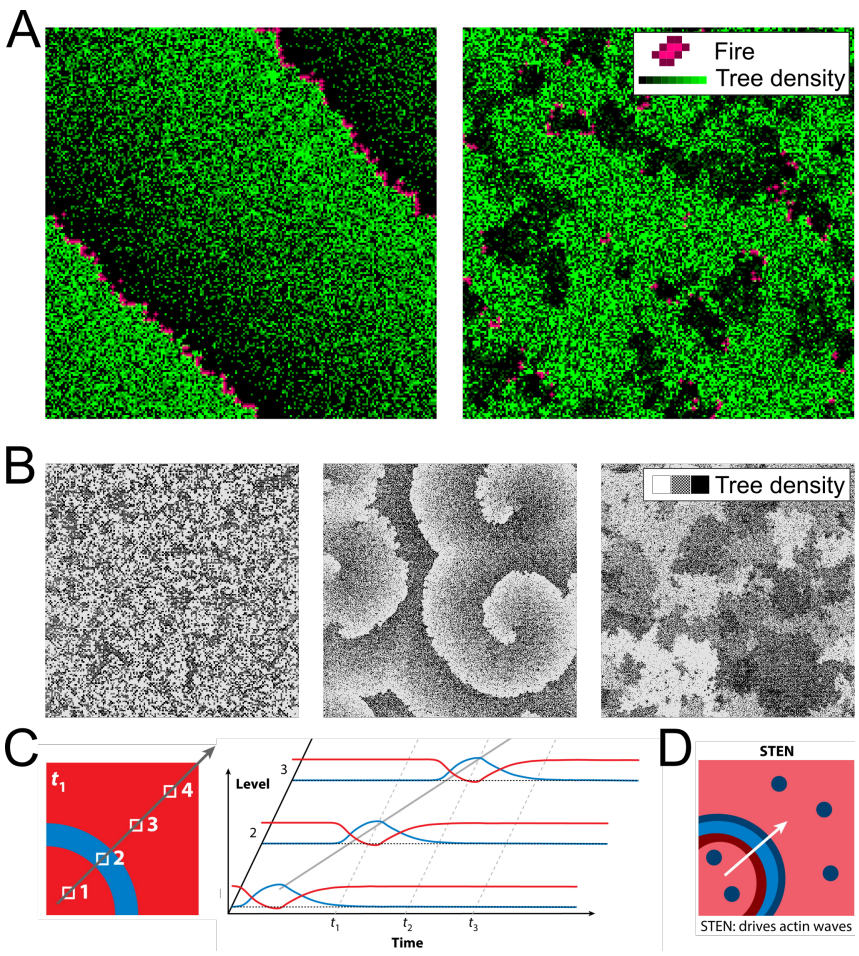

Figure 2.2: Dynamic phases of forest-fire models exhibit similar behaviors to biophysical models of cytoskeletal dynamics. (A) Different phases in a standard forest-fire model: global traveling waves (left); and local isolated patches of activity (right). (B) Phases in a conserved forest-fire model (constant density of trees): increasing the density beyond the first critical point, $\rho^{(1)}_{critical} = 0.547$, causes the transition from small-scale patches to spiral waves (left to middle); and increasing the density beyond the second critical point, $\rho^{(2)}_{critical} = 0.592$, causes the transition from spiral waves to large-scale patches (middle to right). (C) Schematic of a traveling wave through an excitable medium (blue) that must undergo a refractory period before subsequent excitations. (D) The signal-transduction excitable network (STEN) model of cytoskeletal waves. The excitable cytoskeletal medium has occasional burst of actin activity (blue puncta) but also facilitates large-scale spiral waves. The images in A were adapted with permission from forest-fire models by Ms. Melissa Kissling, images in B were adapted from [19] with permission by the American Physical Society, and C and D were adapted from [3] with permission by Annual Reviews.

critical values of control parameters [19] (Figure 2.2B). For the two snapshots in Figure 2.2A, the left side has a higher probability of tree growth but lower lightning probability than the right side, causing different behavior phenotypes. The modified forest fire in Figure 2.2B is constrained by two conditions: (1) lightning will strike in one random location only if there is no other fire in the simulation; and (2) there is a fixed number of trees in the field of view (i.e., when a tree is burned then a new tree will populate elsewhere to replace it).

The models presented in Figure 2.2A–B are simple, but capture essential qualities of signal transduction through excitable media, e.g. wave-like propagation. During biological signal transduction, cascades of biochemical and biophysical interactions are triggered in sequence. In forest-fire models, these sequential signal-transduction events are recapitulated via local communication between neighboring pixels. To put Figure 2.2A–B in context, current biophysical models of cytoskeletal dynamics incorporate traveling waves and refractory periods (Figure 2.2C). Moreover, the transition from patches of local activity (i.e., puncta) to traveling waves in Figure 2.2B upon small perturbations to the system almost exactly mirrors the excitable puncta-to-traveling-waves transition observed in the cytoskeleton (Figure 2.2D).

The connection between experimentally observed cytoskeletal dynamics and physical models of excitability is introduced in Subsection 2.3.2.

2.2 Signal Transduction During Immune Response

2.2.1 Basic Operations of the Immune System

The immune system defends the body against pathogens via two complimentary mechanisms: rapid innate immunity and pathogen-specific adaptive immunity. Cells involved in innate immunity detect chemical signatures of homeostatic imbalances caused by pathogen infection and rapidly respond within several hours. Innate-immune responses have no memory of prior infections, so the anti-pathogen capabilites of this response are one-size-fits all and are limited in strength and scope. Thus, one additional and crucial function of the innate immune system is to activate the adaptive immune system [46].

Adaptive immunity is the potent and highly specific response to pathogens. Upon recognition of pathogenic material (e.g., antigens), the adaptive immune system initiates a multicellular signaling cascade leading to the clonal expansion of adaptive immune cells. Whereas the innate immune system responds within several hours, the adaptive immune systems requires several days to mobilize (Figure 2.3). Although adaptive immune response is slower than innate immune response, its anti-pathogen capabilities are extremely potent. Due to its potency, adaptive immunity must be carefully regulated [46], but can also be engineered and controlled for clinical applications.

Activation and regulation of adaptive immunity are of interest to prevent or treat diseases. Activating the adaptive immune system to recognize and fight can-

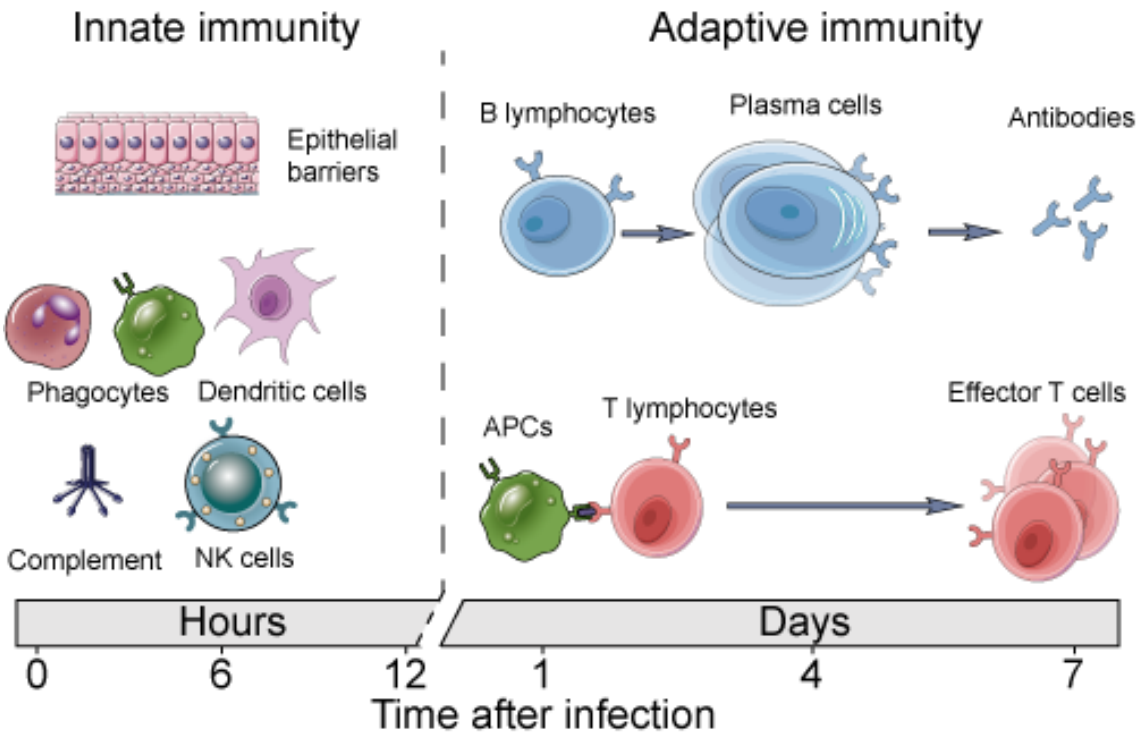

Figure 2.3: Innate immune cells respond to pathogens within several hours of the initial infection (left). Adaptive immune cells respond to pathogens within several days of infection (right). This figure was adapted from Science Online under a Creative Commons Attribution 4.0 International License.

cer has long been a goal for immunologists and oncologists, and work over the past decade has demonstrated the promise of stimulating an immune response to fight cancer via immunotherapies [47, 48]. On the other hand, overactive and uncontrollable adaptive immune responses have been implicated in the development of some cancers [49], autoimmune diseases [50], and allergies [51–53]. Although the body has multiple programmed shutdown mechanisms to combat the deleterious consequences of an overactive adaptive immune response, these mechanisms can also be harnessed to treat disease [54].

2.2.2 Signal Transduction in Effector T Cells

One important component of the adaptive immune system is effector T cells, which are terminally differentiated T cells that can generate rapid anti-pathogen responses. Effector T cells engage in a wide variety of behaviors, including immune regulation to prevent auto-reactivity (i.e., preventing autoimmune disorders), helping in the maturation and activation of other leukocytes (i.e., accelerating immune response), and destroying pathogen-infected cells. Effector T cells are activated via an internal signal-transduction pathway that begins at the T-cell receptor (TCR) and results in the nuclear translocation of several transcription factors, including NF-κB (nuclear factor kappa-light-chain-enhancer of activated B cells), ultimately leading to cell activation and function [55].

Tightly controlled regulation of NF-κB activation is relevant to human health. Improper regulation of TCR-to-NF-κB signaling is associated with primary immun-

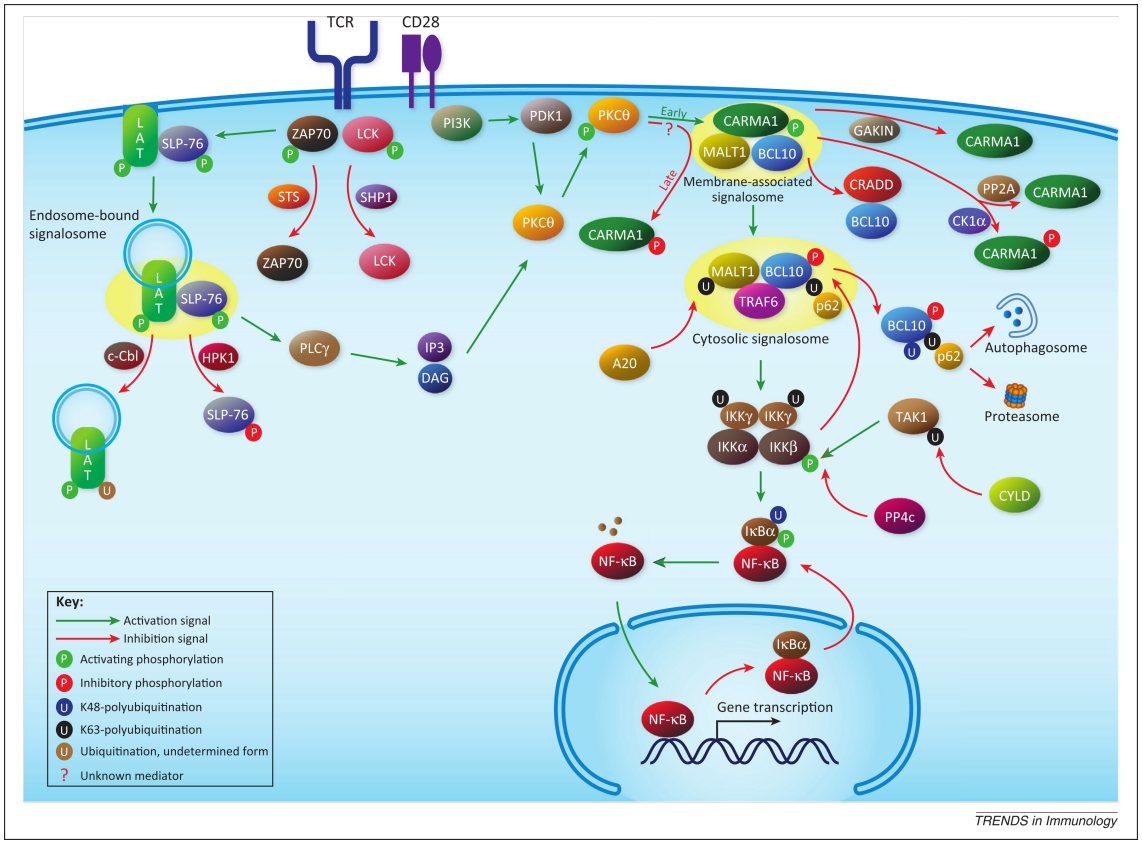

Figure 2.4: Positive and negative regulation of the TCR-to-NF-κB signaling pathway. Reproduced from [37] with permission from Elsevier.

odeficiency disorders [30–32], cancer [33], and autoimmune diseases [34, 35]. Thus, the TCR-to-NF-κB signaling pathway is subject to numerous positive and negative feedback mechanisms [37] (Figure 2.4).

One important protein that participates in both positive and negative regulation of NF-κB is Bcl10 (B-cell lymphoma/leukemia 10) [56]. Gene inactivation studies have shown that T cells without Bcl10 are highly impaired in their response to TCR stimulation [25]. Interestingly, although Bcl10 is critical for the transmission of activation signals through the TCR, it also participates in the self regulation

of T cell activation via several self-limiting mechanisms. Stimulation of the TCR (i.e., the initiating step for cell activation) has also been shown to induce Bcl10 degradation [36, 57–60], and this degradation plays a role in downstream signaling processes [61]. This dual purpose in both the activation and regulation of NF-κB make Bcl10 of interest for its role in controlling system-wide immune response.

2.2.3 Bcl10 Self-Assembly During Signal Transduction

One component of Bcl10-mediated NF-κB activation is Bcl10 self-assembly in microns-long filaments during signal transduction. Upon TCR engagement, Bcl10 polymerizes into filament structures [62] that are nucleated by Carma1 (caspase recruitment domain-containing membrane-associate guanylate kinase protein-1) and scaffolded by Malt1 (Mucosa-associated lymphoid tissue lymphoma translocation protein 1) [8, 63, 64] (Figure 2.5). Bcl10, together with Carma1 and Malt1 (referred to as the CBM complex), form the core of a micron-scale assembly called the POLKADOTS signalosome, which is the site of the final steps of the NF-κB signaling cascade [7, 8, 36, 37]. The structure of Bcl10 is important for its role in the activation of the T-cell signaling network. For example, the polymerization of Bcl10 accelerates the growth of the CBM complex [64], and the scaffold structure of Bcl10 and Malt1 allow for downstream signal transduction such as Traf6 recruitment [8, 65].

Although Bcl10 is essential for signal activation, the structural and kinetic features that limit and ultimately reverse Bcl10-filament polymerization are unclear.

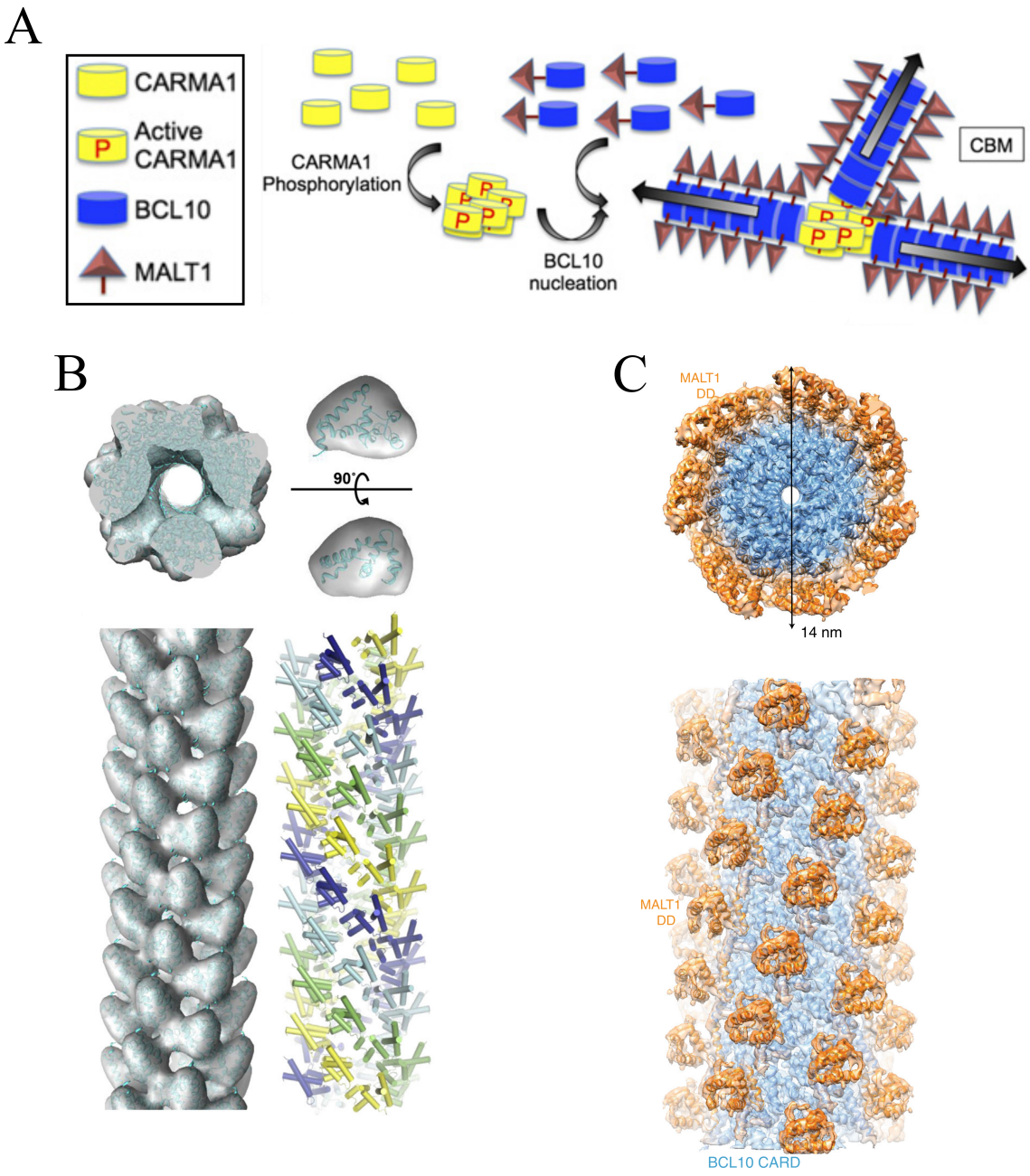

Figure 2.5: Formation of filamentous Bcl10. (A) The biochemical mechanism for Bcl10-Malt1 filament formation: active Carma1 nucleates the Bcl10-Malt1 filaments. (B) Bcl10 core of filaments. (C) Bcl10 core with Malt1 on the surface. A and C were derived from [8] under a CC BY-NC-ND license and B was derived from [62] with permission from Elsevier.

Bcl10 is selectively degraded within the multi-protein complex [36] despite its assembly into filaments decorated with other CBM and POLKADOTS components [8]. One possible mechanism for the degradation of Bcl10 is autophagy via autophagosomes [36]. The traditional models of autophagosome-led autophagy involve complete envelopment of intracellular cargo. Notably, such a mechanism could not be reasonably applied to Bcl10 degradation due to geometric limitations (i.e., Bcl10 are much larger and thus cannot be enveloped by a much smaller autophagosome). Despite the limitations, autophagosome-led degradation of Bcl10 is still considered valid [36,37,56]. Thus, the biophysical and biochemical mechanisms that participate in the self-limiting properties of Bcl10 cannot only be assessed using biochemical approaches and must also include geometry, self-assembly, and organization of protein complexes.

In Chapter 3, simulations and analysis of super-resolution micrographs are used to gain mechanistic insights into this self-limiting process. Further, we discuss how components of the T-cell-activation pathway, including Carma1 nucleation of Bcl10 filaments and Bcl10 degradation, indicate that the TCR-to-NF-κB pathway forms an excitable system.

2.3 Cytoskeletal Excitability and Signal Transduction

2.3.1 Actin and Cell Functions

The cytoskeleton is a dynamic network of proteins responsible for the structural and mechanical properties of the cell. Through the formation of an interlocking

and interconnected filament network, the cytoskeleton exerts forces to participate in cell and physiological functions such as polarization and migration [3], immune-cell activation [39, 66], and wound healing [67].

One important and abundant component of the cytoskeleton is actin. Through continuous polymerization and depolymerization, actin, together with actin-binding proteins such as the Arp2/3 complex and cofilin, facilitates the formation of membrane protrusions and the generation of intracellular forces. The dynamic behavior of actin has been linked to many cytoskeleton-driven phenomena such as the formation of focal adhesions [68], immune-cell activation [27], and protrusions and cell polarization [3]. Thus, understanding the dynamic rearrangements and organization of actin is essential to developing a complete picture of many cellular processes.

The continuous polymerization and depolymerization of actin can manifest wave-like propagations. Through polymerization on the leading edge and depolymerization of from trailing edge, propagating actin waves enable cell functions such as chemotaxis in Dicty [69] and polarization of dendritic cells in search of pathogens [70]. Current perspectives on the mechanisms that enable actin waves are shown in Figure 2.2C. An activation wave of actin (blue) inhibits an inhibition wave (red). If, for some reason, the blue actin wave were to encounter an obstacle or run out of polymerization material (i.e., monomers), then the inhibition wave would "catch up"and cause all polymerization activity to cease.

Actin waves are excitable. As introduced in Section 2.1, excitability enables the dynamic behavior of a system to rapidly change character either spontaneously or due to external perturbation. The STEN (signal transduction excitable network)

model of actin-network dynamics in Figure 2.2D predicts a critical point above which puncta of actin activity can manifest of wave-like propagations. Recently, it was demonstrated that the excitability of actin and actin-associated signaling proteins can enable switching between migratory modes in Dicty from chemical stimulation [9].

2.3.2 Models and Simulations of Actin Excitability

Models and simulations of actin excitability can be used to gain qualitative and quantitative insights into the coupling of actin and cell behavior. For example, the switching between migratory modes in Dicty shown in [9] can be explained using an excitable-signal-transduction network model (shortened to "STEN"in the figure) [3, 71] (Figure 2.6).

Signal-transduction events (red) promote actin polymerization (green), leading to propagation of actin-polymerization waves (blue) (Figure 2.6A). Importantly, the polymerization of actin is a postive feedback mechanism for further signal-transduction events, which in turn leads to further actin polymeriation. In typical (i.e., wild-type) cells, these waves could propagate over time in any direction. Conversely, if impeded or subjected to depletion of available actin, waves in one or both directions could terminate (Figure 2.6B). Furthermore, chemical perturbations can modify the character of actin-wave propagation and the shape of membrane protrusions (Figure 2.6C).

Other computational models and simulations also capture actin-wave dynam-

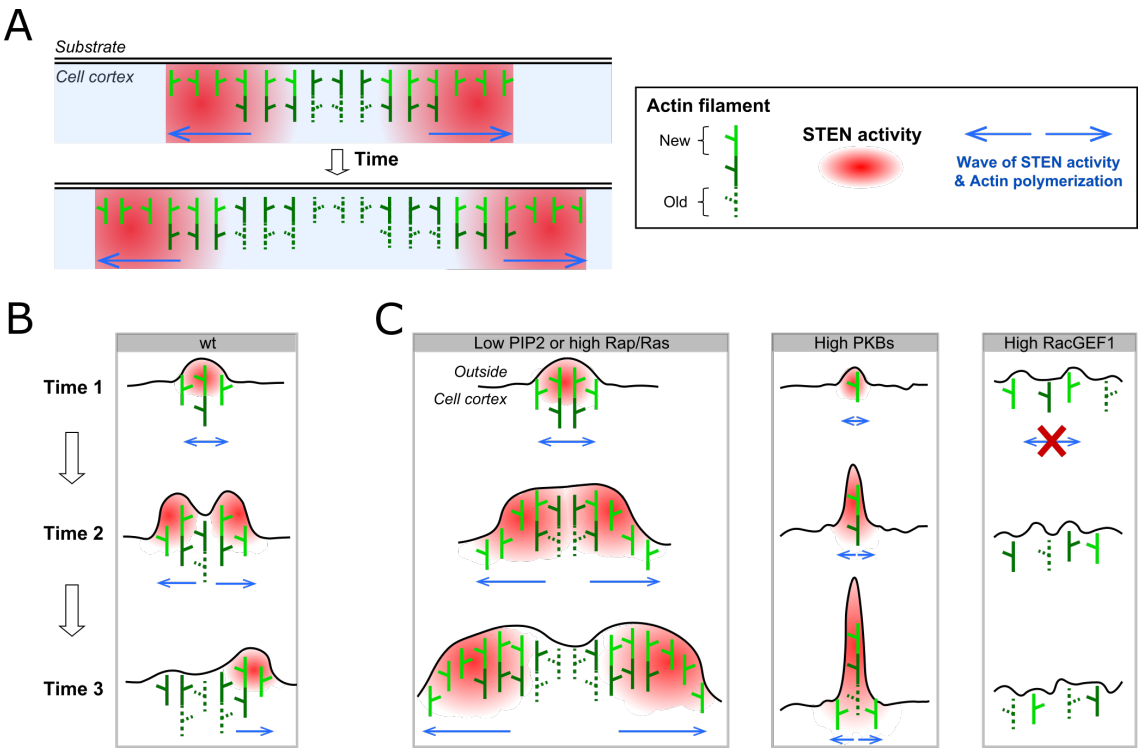

Figure 2.6: Biochemical Model of Cytoskeleton Excitability. (A) A propagating wave of actin and actin-associated signaling proteins. Actin polymerization (green) leads to increased signaling (red), which in turn promotes further actin polymerization. (B) Baseline over-time schematic of typical actin-polymerization waves. If, for some reason, signaling or actin polymerization is inhibited (e.g., depletion of monomers, physical boundary), then signaling and polymerization will terminate. (C) Chemical perturbations modify the character of actin-polymerization waves and propagation of signals. Representative repercussions include broad, actin-rich protrusions, narrow and sharp protrusions, or a semistable actin cortex without any dynamics. This figure was derived from [71] under an Open Access License by Molecular Systems Biology.

ics. One-dimensional models of actin and signaling proteins have been used to connect actin flow to polarity, persistence, and migration [72], two- and three-dimensional simulations of coupled phase and auxiliary fields can recapitulate cell-migration phenotypes without explicit cytoskeletal components [73], and fine- and coarse-grained simulations of the cytoskeleton have shown that actin force generation can cause large-scale reorganization via force amplification [11] and bundling dynamics [74].

2.3.3 Actin Sensing of the Physical Environment

The actin cytoskeleton can detect and respond to physical properties of the extracellular environment. Textures much smaller than the size of the cell can influence actin-mediated behaviors. Symmetric and uniformly spaced nanotopographic ridges bidirectionally bias actin-driven migration [29] and modulate actin-driven B-cell activation [39]. Asymmetric surface textures (e.g., sawteeth patterns) can induce unidirectional bias of cell migration in pitch-dependent [38] and cell-type-specific manners [24]. Furthermore, the stiffness of cell substrates can modulate T-cell activation via actin-generated forces [27].

Biochemical components involved in waves of actin polymerization are impacted by features in the extracellular environment. High-curvature textures in the extracellular environment can facilitate Arp2/3 branching [15] and upregulate the activity of N-WASP, Cortactin, and Arp2/3 [16].

Despite the connection between actin-polymerization dynamics and the ex-

citability of actin and actin-associated signaling proteins, we currently do not have a detailed understand of the connection between actin-based texture sensing, cytoskeletal signaling, and whole-cell behavior. In Chapter 5, I link the frameworks of cytoskeletal excitability with physical models of cytoskeletal dynamics to address this open question.

2.4 Quantitative Measurements of Biological Images

2.4.1 Connecting Bioimage Data and Cell Behavior

Quantitative measurements of dynamic cellular processes are crucial for the full understanding of cell behavior. Although genomics and proteomics have led to connections between molecular signatures and cell function, these efforts have not produced a complete biological mapping between transcription and behavior. In fact, it has been argued that if all molecular measurements inside of a cell are available, the complexity of the data may make their integration and interpretation impossible [75].

One prominent tool for building a quantitative understanding of cellular processes is through image analysis. Integrating quantitative computer vision techniques with a variety of imaging modalities has exposed the mechanisms behind actin-driven protrusions [76] and membrane fluctuations in amoeboid cells during collective streaming [77]. Additionally, image-analysis techniques from physics have been an important tool for extracting biological information from images. Particle image velocimetry (PIV) originated in fluid dynamics, and is now implemented in

many bioimage-analysis workflows [78, 79]. Particle tracking that was designed to study flows in colloids is now ubiquitous in studies ranging from the tracking of f-actin speckles [76] to the swarming of fruit flies [80].

2.4.2 Image-Based Measurements of Biological Flows

The flow of biological material during cellular processes is ubiquitous, including during development [81] and wound healing [67], and in cytoskeletal dynamics [82]. The measurement of biological flows from image data typically relies on information contained within a single-pixel or few-pixel region. One widely-used pixel-scale technique is PIV, which was originally designed by physicists to study fluid flows. PIV uses correlations within a few-pixel region to create a spatial mapping between two sequential images in a time-series. If the frame rate of the time-series is sufficiently high, this mapping theoretically converges on the ground-truth-deformation field that frames undergo in the time series.

PIV also enables a variety of downstream analysis capabilities in studies of biological behavior. For example, PIV-driven analysis of chaos in flow fields can distinguish between benign and malignant breast-cancer cells [79]. Although PIV is a powerful technique, it's effective use requires a series of conditions to be met, including an abundance of features in the time-series (which is not typical in fluorescence imaging) and small changes between frames. Thus, PIV is typically limited to phase-contrast and DIC images in which there is an abundance of features and rapid imaging frame rates are available. Although extensions of PIV, e.g. spatiotempo-

ral image correlation spectroscopy (STICS), can provide better performance at a higher computational cost [83], PIV is still correlation-based, and thus is limited to the analysis of images with an abundance of features.

One technique that outperforms correlation-based reconstruction of flow fields from fluorescent time-series of biological images is optical flow [84]. Originally developed for applications in robotics and stereo vision, optical flow is currently used in a variety of modern technologies, such as self-driving cars [85] and facial-recognition algorithms [86].

Optical flow uses spatial and temporal gradients in sequential images to create a mapping between adjacent frames [87]. In a $(2+t)$-dimensional time-series of images, a moving object that is originally located at voxel with indices (x, y, t) will translate to some new voxel with indices $(x + \Delta x, y + \Delta y, t + \Delta t)$. If the intensity of the object is the same at both coordinates in the time-series then

$$I(x, y, t) = I(x + \Delta x, y + \Delta y, t + \Delta t). \tag{2.2}$$

The primary objective of optical flow is to solve for translation fields Δx and Δy that provide the spatial mapping between each pair of adjacent frames in the time-series. If $I(x, y, t)$ represents a continuous field of (2D+t)-dimensional voxels, then a Taylor-expansion of the RHS of Equation 2.2 yields

$$\frac{\partial I}{\partial x}\frac{\Delta x}{\Delta t} + \frac{\partial I}{\partial y}\frac{\Delta y}{\Delta t} + \frac{\partial I}{\partial t} = 0 \tag{2.3}$$

and, if $\vec{v} =< \frac{\Delta x}{\Delta t}, \frac{\Delta y}{\Delta t} >$, then

$$\vec{\nabla} I \cdot \vec{v} = -\frac{\partial I}{\partial t} \tag{2.4}$$

where $\vec{v}$ is a vector-field of velocities.

Equation 2.4 is a manifestation of the aperture problem: a class of computer-vision problems in which a small subsection of a field is visible. In Figure 2.7, there are infinitely many ways to interpret the motion of the black and white pattern if you are restricted to looking only through the inner circle. In the case of optical flow, only having one set of gradients for a voxel provides similar limitations—there are infinitely many solutions to Equation 2.4. Thus, solving the optical-flow equation requires additional constraints.

There are many solution to Equation 2.4 that add additional constraints to acquire an estimate for optical flow. Global methods maximize the smoothness of the field [87], or minimize shear [88]. However, such approaches produce dense and continuous flow fields that are not realistic in biological applications (i.e., flow in one part of a field likely does not depend upon or affect flow at distant locations). An alternative set of approaches to estimating optical flow is through local, gradient-based methods. Local methods integrate information from small regions of interest. One popular method and foundational local methos was developed by Lucas and Kanade [89]. Specifically, for a local region of n pixels there are n linear equations

that must be solved to estimate optical flow:

$$\begin{bmatrix} (\frac{\partial I}{\partial x})_1 v_{x_1} + (\frac{\partial I}{\partial y})_1 v_{y_1} \\ (\frac{\partial I}{\partial x})_2 v_{x_2} + (\frac{\partial I}{\partial y})_2 v_{y_2} \\ \vdots \\ (\frac{\partial I}{\partial x})_n v_{x_n} + (\frac{\partial I}{\partial y})_n v_{y_n} \end{bmatrix} = - \begin{bmatrix} (\frac{\partial I}{\partial t})_1 \\ (\frac{\partial I}{\partial t})_2 \\ \vdots \\ (\frac{\partial I}{\partial t})_n \end{bmatrix}. \tag{2.5}$$

For the purposes of solving for the central pixel in the local region, the Lucas-Kanade method assumes that all $\vec{v_i}$ are equal, thus

$$\begin{bmatrix} (\frac{\partial I}{\partial x})_1 & (\frac{\partial I}{\partial y})_1 \\ (\frac{\partial I}{\partial x})_2 & (\frac{\partial I}{\partial y})_2 \\ \vdots & \vdots \\ (\frac{\partial I}{\partial x})_n & (\frac{\partial I}{\partial y})_n \end{bmatrix} \begin{bmatrix} v_x \\ v_y \end{bmatrix} = - \begin{bmatrix} (\frac{\partial I}{\partial t})_1 \\ (\frac{\partial I}{\partial t})_2 \\ \vdots \\ (\frac{\partial I}{\partial t})_n \end{bmatrix}. \tag{2.6}$$

The resulting system of equations is overdetermined (two variables for n equations), and thus a typically good solution minimizes the sum of the inner product of the residuals (i.e., least-squares minimization). Notably, despite having more equations than degrees of freedom, the Lucas-Kanade formulation could still suffer from the aperture problem if all spatial gradients are parallel. In such a case, the $A^T A$ matrix will be singular (i.e., not invertible) and not yield a solution.

In Chapters 4 and 5, I use the Lucas-Kanade optical-flow formulation in an image-analysis workflow to quantify and characterize actin-wave dynamics from fluorescent time series.

A

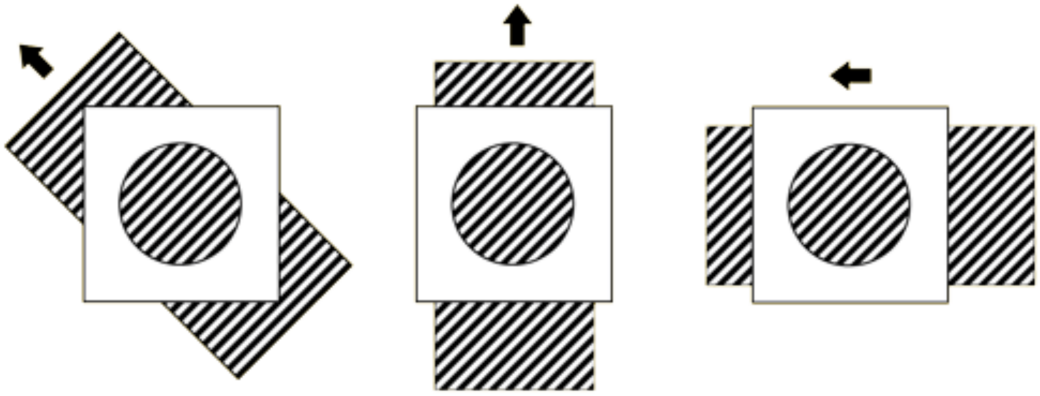

Figure 2.7: (A) A schematic representation of the aperture problem. If the field-of-view is confined to the interior cut-out circle, it is impossible to distinguish the different types of motion in the schematic. Adapted from [90].

Chapter 3: Signaling Through Polymerization and Degradation: Analysis and Simulations of T-Cell Activation Mediated by Bcl10

This chapter was adapted from Campanello, Traver, Shroff, Schaefer, and Losert [91]. Maria Traver performed the experiments, Leonard Campanello performed the analysis, Leonard Campanello built the simulations, and Leonard Campanello and Maria Traver wrote the paper.

3.1 Overview

The adaptive immune system serves as a potent and highly specific defense mechanism against pathogen infection. One component of this system, the effector T cell, facilitates pathogen clearance upon detection of specific antigens by the T-cell receptor (TCR). A critical process in effector T cell=activation is transmission of signals from the TCR to a key transcriptional regulator, NF-κB. The transmission of this signal involves a highly dynamic process in which helical filaments of Bcl10, a key protein constituent of the TCR signaling cascade, undergo competing processes of polymeric assembly and macroautophagy-dependent degradation. Through com-

putational analysis of three-dimensional, super-resolution micrographs, we quantitatively characterize TCR-stimulated Bcl10 filament assembly and length dynamics, demonstrating that filaments become shorter over time. Additionally, we develop an image-based, bootstrap-like resampling method to demonstrate quantitatively the preferred association between autophagosomes and either Bcl10-filament ends or punctate-Bcl10 structures, implying that autophagosome-driven macroautophagy is directly responsible for Bcl10 filament shortening. We probe Bcl10 polymerization-depolymerization dynamics with a stochastic Monte-Carlo simulation of nucleation-limited filament assembly and degradation, and we show that high probabilities of filament nucleation in response to TCR engagement could provide the observed robust, homogeneous, and tunable response dynamic. Furthermore, the speed of autophagic degradation of filaments preferentially at filament ends provides effective regulatory control. Taken together, these data suggest that Bcl10 filament growth and degradation act as an excitable system that provides a digital response mechanism and the reliable timing critical for T-cell activation and regulatory processes.

3.2 Background

The vertebrate adaptive immune system consists of billions of T and B lymphocytes, which serve as a potent and highly specific host defense mechanism against pathogen infection. Once an antigen, an immune-activating component of a pathogen, has been recognized by the T-cell receptor (TCR), an intracellular signaling cascade is initiated that leads to the clonal expansion of T cells responsive to this

antigen. This anti-pathogen immune response, including the T-cell component, will cause damage to healthy tissue if not temporally limited [49]. Indeed, unregulated adaptive immune responses have been implicated in the development of certain cancers [49] and autoimmune diseases [50]. Thus, adaptive immune responses include programmed shutdown mechanisms to maintain homeostasis and prevent damage to host tissues [50,54]. In this study, we introduce novel image-analysis tools for the robust analysis of a component signaling pathway of the adaptive immune response from a biophysical perspective, specifically focusing on the spatial organization of a key signaling structure that contributes to adaptive immunity.

The many classes of effector T cells are the main cell types that control adaptive immunity. Effector T cells are terminally differentiated T lymphocytes with previous antigen exposure, and can generate rapid anti-pathogen responses. Antigen engagement of the TCR in effector T cells initiates an internal signal-transduction pathway that leads to the translocation of NF-κB from the cytoplasm to the nucleus. NF-κB is a heterodimeric protein complex in both vertebrates and invertebrates [92] that controls gene transcription in response to a diverse array of receptors [93]. In effector T cells, the nuclear translocation of NF-κB results in the *de novo* or increased expression of a large number of genes involved in T-cell proliferation and immune response mechanisms [92, 94]. Improper regulation of NF-κB signaling in T cells is mechanistically associated with primary immunodeficiency [30–32] and autoimmune disease [34, 35]. Thus, the regulation of the TCR-to-NF-κB pathway is critically important for proper immune function.

A key signaling protein in the TCR-to-NF-κB pathway is Bcl10 [56]. Upon

TCR stimulation, Bcl10 assembles with its signaling partners Carma1 and Malt1 to form the micron-scale CBM complex [8, 37, 65, 95, 96]. In effector T cells, the CBM complex forms the core of a filamentous assembly called the POLKADOTS signalosome, which serves as the cytoplasmic site of the terminal steps of the NF-κB-activation cascade [7,8,36,37,62,64]. At the same time that Bcl10 is being assembled into microns-long filaments, it is also being degraded [37,57–61]. We have previously shown that proteolysis of Bcl10 occurs within the POLKADOTS signalosome via TCR-dependent selective autophagy [36]. In this degradative process, autophagosomes associate with POLKADOTS filaments, resulting in selective destruction of Bcl10 and thus terminating signals to NF-κB. Data suggest that the balance between assembly of filamentous Bcl10 in POLKADOTS and proteolytic degradation of Bcl10 via selective autophagy determines the extent of NF-κB activation [36,37].

Notably, many outputs of TCR signaling exhibit nonlinear response profiles, including all-or-nothing (i.e., digital) responses. Although not every T cell response has digital characteristics [97], studies have demonstrated that specific TCR-triggered events are digital, including activation of the extracellular regulated kinase-mitogen activated protein kinase (ERK-MAPK) signaling cascade [98–100], signaling via the Protein kinase D2-protein kinase C (PKD2-PKC) cascade [101], release of cytokines [102], and activation of cytolytic capacity [103]. Additionally, we have previously shown that TCR activation of NF-κB is digital in nature, with formation of and signal transmission by the POLKADOTS signalosome occurring in an all-or-nothing manner [104]. Mechanistically, how nucleation, growth and eventual autophagic degradation of POLKADOTS filaments are connected to the digital nature

of the NF-κB cascade is unclear. In this manuscript, we link the nonlinear character of the signaling cascade to the spatial organization, assembly, and degradation of filamentous Bcl10. We propose that highly nonlinear self-assembly and degradation processes comprise an excitable system, enabling a rapid yet self-limiting response.

Several key details of this polymerization process are known: recent cell-free cryo-electron-microscopy studies revealed that Bcl10 polymerizes into filaments with a geometrically confined, helical arrangement with other POLKADOTS components [8, 62, 64]. Although the core of the POLKADOTS filament is composed primarily of Bcl10, polymerization of Bcl10 is nucleated by short oligomers of Carma1, and the Carma1-driven nucleation of Bcl10 can act as an amplifier of activation signals from the T-cell receptor to NF-κB [8]. In contrast to the above parameters driving filament growth and signal propagation, autophagic degradation of Bcl10 opposes this amplification process. However, the geometric and kinetic features that limit, and ultimately reverse, filament growth in living T cells are unclear. These opposing effects on filament growth and degradation are not well understood, and cannot be assessed via traditional biochemical approaches and signaling pathway models, which exclude spatial organization.

In this study, we quantify the spatial arrangement of Bcl10, its colocalization with autophagosomes, and the randomness of their relative spatial distributions. Our analysis introduces a novel computational workflow that combines bootstrap-like resampling methods adapted for image features and medial-axis-thinning skeletonization for the robust analysis of the structure and organization of Bcl10 filaments in relation to autophagosomes. The methods we present are broadly applicable to

studies of biologically encoded spatial colocalizations and self-assembly, such as toll-like receptor-stimulated assembly of the myddosome, RIG-I-like receptor triggering of mitochondrial antiviral-signaling protein oligomerization, and activation of the various sensor proteins that promote assembly of micron-scale inflammasomes [105]. To gain further mechanistic insights into the assembly and degradation dynamics of POLKADOTS filaments, we complement the analysis of super-resolution images with stochastic Monte Carlo simulations of POLKADOTS dynamics that include the nucleation, growth, and degradation of Bcl10. In sum, we show that spatial assembly and degradation of protein complexes in the TCR-to-NF-κB-activation cascade are key design elements to ensure a rapid response while preventing ongoing immune activation. These elements may also contribute to the digital nature of this crucial signaling pathway.

3.3 Results

3.3.1 Measuring Bcl10 Filament Lengths

Utilizing a long-term murine-effector-T-cell clone, D10.G4.1 (henceforth referred to as D10), we engineered a cell line that stably expressed GFP-tagged Bcl10. Using the D10 cell line, we imaged Bcl10 filaments in cells fixed at 20- and 40-min post-TCR activation using a super-resolution instant structured illumination microscope (iSIM) [106] (Figure 3.1A). The earliest evidence of formation of POLKADOTS structures is at 10 min post-TCR activation. These polymers are maximally evident by 20 min post-activation, at which point initial activation with autophago-

somes is also apparent. Association with autophagosomes and degradation of Bcl10 persists through 2 hr post-stimulation, by which time Bcl10-containing polymers can no longer be found in any cells. Indeed, these polymers are rare even by 60 min post-activation [37, 95]. Thus, 40 min post-activation is a reasonable time point at which to assess intermediate consequences of autophagosome association with Bcl10 filaments.

To analyze these data, we developed a semiautomatic segmentation and skeletonization algorithm based on medial-axis thinning, and used the resultant skeletons to obtain various structural measurements (Methods). Bcl10-rich regions with skeleton lengths less than 150 nm (the approximate spatial resolution of the iSIM) were designated as punctate structures, labeled by "P"in these data. The punctate structures were analyzed separately from micron-scale filaments (Figure 3.1B), the latter of which ranged in length from 0–5 μm (Figure 3.1C). Between 20 min and 40 min post-activation, the relative number of Bcl10 puncta increased, and the number of long Bcl10 filaments correspondingly decreased (Figure 3.1D).

We define a correlation measure ρ to assess the relationship between the number of Bcl10 puncta and distribution of Bcl10-filament lengths. At both time points, a moderate negative correlation ($\rho < -0.6$) existed between the overall number of Bcl10 puncta and the distribution of Bcl10-filament lengths. Thus, cells with fewer puncta were more likely to have long filaments, and cells with more puncta were more likely to have shorter filaments (Figure 3.1D). The negative correlation between the average number of puncta and average filament length was statistically significant at the single-cell level: cells at 40 min post-stimulation were more likely to have both

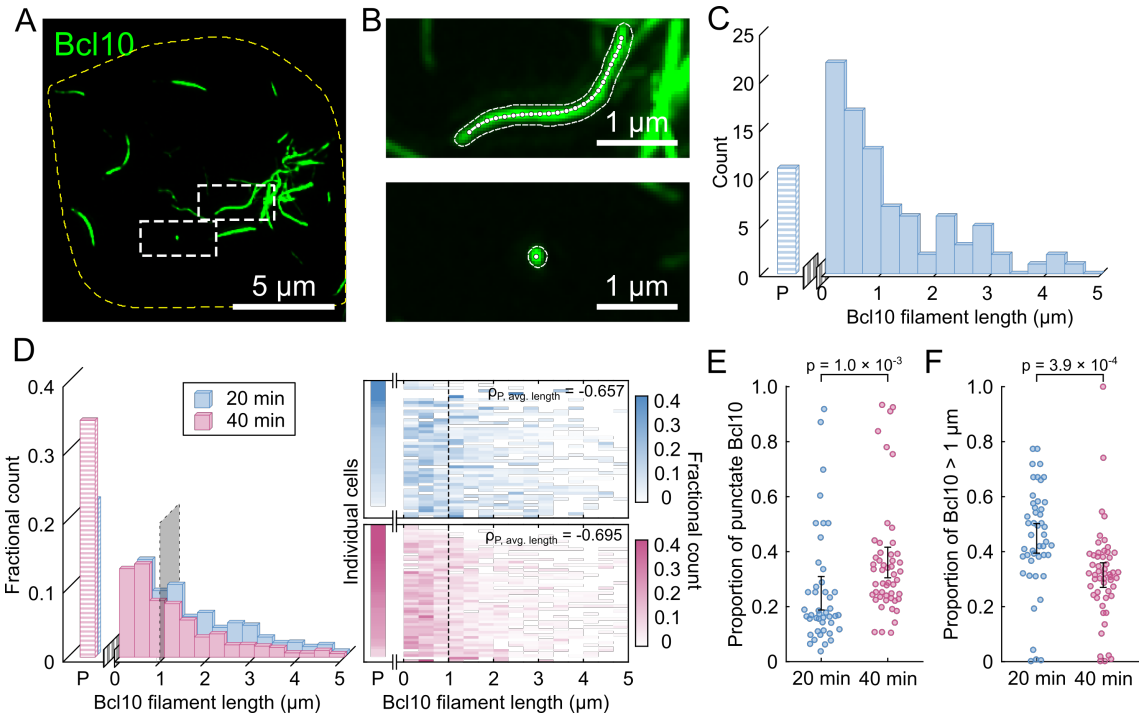

Figure 3.1: Bcl10 filaments shorten between 20 min and 40 min post-T cell receptor activation. (A) Representative image of an activated T cell 20 min after TCR stimulation. (B) Representative Bcl10 filaments within the activated T cell. Filament outlines and skeletons were calculated using a semiautomatic segmentation method and medial axis thinning. The upper image exemplifies the filamentous form of Bcl10 and the lower image is representative of punctate Bcl10. (C) Representative distribution of Bcl10 lengths from all Bcl10 filaments from (A). Punctate Bcl10 structures were separately counted and binned as P. (D) Cumulative length distributions of Bcl10 filaments from all T cells at 20 min (47 cells from 2 experiments) after TCR stimulation and 40 min (53 cells from 2 experiments). Each row is a length distribution for a cell sorted by the percentage of punctate Bcl10 structures in each cell. The correlations between the number of punctate structures and average filament lengths are -0.657 and -0.695 at 20 min and 40 min post-activation, respectively. (E) Scatter plot of the proportion of punctate Bcl10 structures at 20 and 40 min after TCR stimulation. (F) Scatter plot of the proportion of Bcl10 filaments longer than 1 μm at 20 min and 40 min after TCR stimulation. Correlations are the Pearson product-moment correlation. Error bars are the 95% confidence interval of the mean. p-values were calculated using a two-sample t-test were considered significant if less than 0.05.

a larger relative proportion of punctate structures (Figure 3.1E, p = 0.0010), and a decrease in the relative number of Bcl10 filaments longer than 1 μm (Figure 3.1F, p = 0.00039). Taken together, these results are consistent with the interpretation that between 20 min and 40 min post-activation Bcl10 filaments decrease in length and the proportion of punctate structures increases. This increase in the number of punctate structures and decrease in the number of long filaments could indicate: (i) ongoing nucleation of new filaments; (ii) disassembly or end-directed degradation of existing filaments; (iii) scission of existing filaments, which would create two daughter filaments with each scission event; or (iv) some combination of the above processes.

3.3.2 Examining Autophagosome-Bcl10-Filament Interactions

Our previous work has demonstrated that Bcl10 within the filamentous POLKA-DOTS signalosome is targeted for degradation by macroautophagy (henceforth referred to as autophagy) [36], an intracellular degradative process involving the envelopment of cargo by double-membraned vesicles called autophagosomes. Autophagic degradation of Bcl10 leads to a dampening of NF-κB activation and NF-κB-dependent T-cell responses [36]. To examine whether autophagy is responsible for the observed decrease in Bcl10 filament length, we expressed an RFP-tagged form of the autophagosome membrane protein LC3 in our Bcl10-GFP-expressing D10 cell line, then imaged static interactions between Bcl10 filaments and LC3-labeled autophagosomes at 20 min and 40 min post-TCR activation (Figure 3.2A).

Consistent with our previous data [36], these experiments indicated that filamentous Bcl10 and LC3-positive autophagosomes existed simultaneously in activated T cells. A large number of autophagosome contacts with Bcl10 filaments were observed. Thus, independent semiautomatic segmentation of Bcl10 filaments and autophagosomes was used to determine the number and location of contacts (Figure 3.2B). Interestingly, we observed that activated T cells have significantly fewer Bcl10-autophagosome contacts at 20 min post-TCR stimulation than at 40 min post-stimulation (Figure 3.2C, $p = 0.000145$). However, this fact alone is not sufficient to conclude that contact formation is preferred. To assess whether autophagosome contacts with Bcl10 filaments form preferentially or randomly, we developed an image-based-resampling method analogous to statistical bootstrapping (Methods). We randomly rearranged the segmented autophagosomes throughout the cell cytosol and recalculated the resulting filament-autophagosome contacts (Figure 3.2D). The cell-averaged number of colocalizations in these rearrangements was significantly fewer than the number in the experimental observations (Figure 3.2E). As an additional test, we conducted 100 rearrangements of each individual cell and constructed a confidence interval for the number of randomized contacts. The actual number of autophagosome contacts in 45 of 47 cells at 20 min post-activation, and 52 of 53 cells at 40 min post-activation, was greater than the 95% confidence interval for random LC3 contacts (3.2F). Thus, we concluded that contact between Bcl10 and autophagosomes was non-random, and that there were indeed more Bcl10-autophagosome interactions at 40 min post-activation.

Our results thus far indicate that at 40 min post-activation, Bcl10 filaments

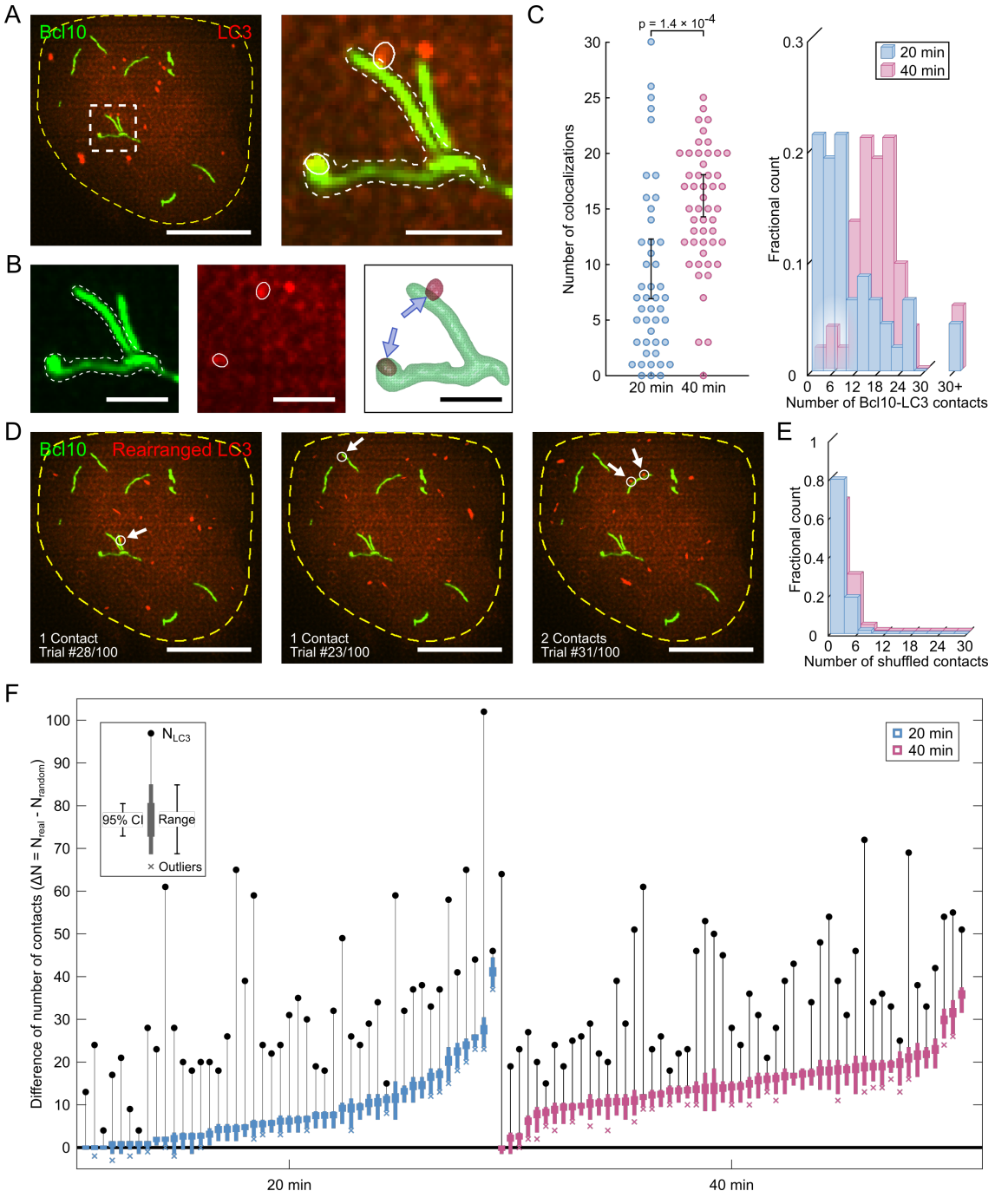
A
Bcl10
LC3
B
C
p = 1.4 × 10^-4
Number of colocalizations
20 min
40 min
Fractional count
Number of Bcl10-LC3 contacts
D
Bcl10
Rearranged LC3
1 Contact
Trial #28/100
1 Contact
Trial #23/100
2 Contacts
Trial #31/100
E
Fractional count
Number of shuffled contacts
F
Difference of number of contacts (ΔN = N_real - N_random)
N_LC3
95% CI
Range
Outliers
20 min
40 min

Figure 3.2: Bcl10 filaments are preferentially in contact with autophagosomes relative to a random null model. (A) Representative image of an activated T cell 20 min after TCR stimulation. Bcl10 filaments (green) and LC3 vesicles (autophagosomes, red) are within the yellow cell boundary. The outlined ROI contains a Bcl10 structure with two in-contact autophagosomes. (B) Representative Bcl10 filament-autophagosome contacts. Segmentation and skeletonization analyses identify the number and location of contacts highlighted by blue arrows. (C) Cumulative number of contacts in all T cells (20 min: 47 cells from 2 experiments; 40 min: 53 cells from 2 experiments). There is a statistically significant difference in the number of Bcl10-autophagosome contacts at 20 min and 40 min post-stimulation ($p = 0.00014$). (D) Three representative trials of the resampling from the cell in (A). Contacts that formed after resampling are highlighted with arrows. (E) The cumulative distribution of the number of Bcl10 filament-autophagosome contacts in the random rearrangement trials. (F) Difference between the true number of Bcl10 filament-autophagosome contacts and the number of contacts found in each of the 100 trials per cell. Positive values indicate a greater number of true contacts than found in the trials. There is statistically significant difference in the number of contacts between the true and rearranged data in 45 of 47 T cells imaged 20 min post-activation, and 52 of 53 T cells imaged 40 min post-activation. Error bars are the 95% confidence interval of the mean and were calculated independently for each cell. p-values were calculated using two-tailed t-tests. p-values less than 0.05 were considered significant.

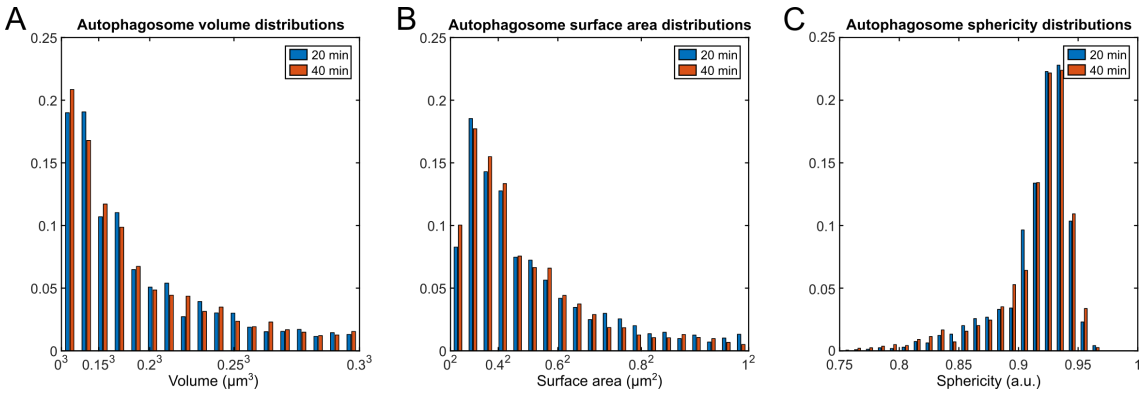

Figure 3.3: Shape and size statistics of autophagosomes 20 min and 40 min post-activation. (A) Distribution of autophagosome 3-D volumes. (B) Distribution of autophagosome 3-D surface areas. (C) Distribution of autophagosome sphericities. A sphericity of 1 corresponds to a sphere and sphericity of 0 corresponds to a flat disk.

are both shorter and have increased contact with autophagosomes, consistent with the interpretation that autophagosomes degrade the filaments over time. However, a mechanistic problem arises from these data: autophagy occurs when double-membraned vesicles completely surround and envelop intracellular cargo, yet Bcl10 structures are larger than autophagosomesthe majority of autophagosome structures are smaller than $(0.2\ \mu\text{m})^3$ in volume at both 20 min and 40 min post-activation (Figure Figure 3.3).

The traditional biophysical understanding of mechanisms of autophagy may not be viable as an explanation for Bcl10-filament degradation. To examine the mechanism whereby autophagosomes degrade Bcl10 filaments, we examined the location of autophagosome colocalizations along each filament. Biochemical and structural studies have demonstrated that Bcl10 filaments have two distinct end points and no junctions along the main body [8]. However, due to the resolution

limits of this imaging method, some filaments appear joined. Thus, employing the same super-resolution dataset used for Figure 3.2, we extracted Bcl10 filament skeletons and fragmented them to eliminate high-degree junctions such that the resulting skeleton configurations minimized the total bending energy (Figure 3.4A, Methods). After processing the skeletons, each Bcl10 filament was segmented based on the distance from the nearest skeleton endpoint (Figure 3.4B). Finally, we examined each colocalization event between an autophagosome and a Bcl10 structure. If the Bcl10 structure was punctate, the event was designated P, and if the Bcl10 structure was filamentous, the event was characterized by the shortest distance between the autophagosome and the skeleton endpoint (Figure 3.4C). Excluding puncta, the distance-from-end distributions at 20 min and 40 min were not statistically distinguishable (Figure 3.4C, $p = 0.085$), and we found a marked preference for autophagosomes to localize near filament ends at both time points. Interestingly, a greater proportion of autophagosomes were in contact with Bcl10 puncta (as opposed to filaments) at 40 min post-activation than at 20 min post-activation (Figure 3.4C, $p = 2.03 \times 10^{-9}$). Although the proportion of punctate Bcl10 approximately doubled between 20 and 40 min post-activation (Figure 3.1E), the proportion of autophagosomes that localized to puncta approximately quadrupled over the same period (Figure 3.4C), indicating a distinct preference for autophagosomes to localize with punctate Bcl10 at the later time point.

Our observations thus far indicate that autophagosomes are more likely to localize to the ends of filaments and, by 40 min post-activation, to Bcl10 puncta. To assess whether these localizations are truly preferred, as opposed to random, we

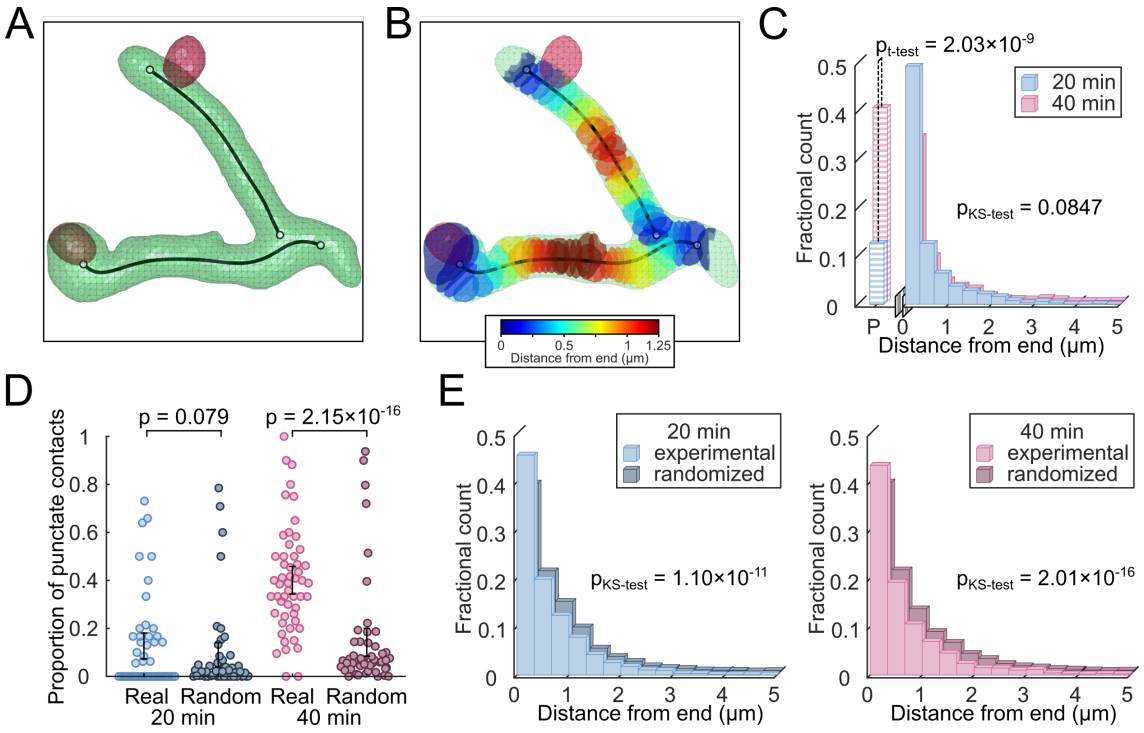

Figure 3.4: Autophagosomes preferentially localize to Bcl10-filament ends and, at later timepoints, to Bcl10 puncta relative to a random null model. (A) Representative segmented Bcl10 filaments (green) and autophagosomes (red) after post-processing, overlaid with the pruned medial-axis skeleton of Bcl10 (black). Filament skeletons were fragmented to minimize the bending energy at junctions. (B) Using the skeleton of the representative Bcl10 filament, the filament volume was segmented into sections based on the nearest distance from skeleton ends. (C) Distribution of autophagosome-Bcl10 contacts by distance from endpoint (filamentous Bcl10) or punctate Bcl10 (P). (D) Scatter-bar plot of the proportion of Bcl10 puncta per cell in contact with an autophagosome in experimental and randomized data. (E) Distribution of autophagosome-filamentous Bcl10 colocalizations by distance from endpoint in experimental and randomized data. p-values in C and E were calculated using two-sample KS tests and p-values in D were calculated using paired two-sample t-tests. p-values less than 0.05 were considered significant.

again employed the randomized images from the image-based resampling shown in Figure 3.2D. First, we compared the number of colocalizations of Bcl10 puncta with autophagosomes in the true versus the randomized images (Figure 3.4D). At 20 min post-activation, the true and random distributions of contacts were indistinguishable (Figure 3.4D, $p = 0.079$), indicating that autophagosome-puncta contacts could be the result of random co-localization. However, at 40 min post-activation, the number of true puncta contacts was greater than the number of such contacts in the randomized images, and this enrichment was statistically significant (Figure 3.4D, $p = 2.15 \times 10^{-16}$), indicating that punctate Bcl10 structures were preferentially in contact with autophagosomes at this time point. Next, we compared the distance-from-end distributions of autophagosome-filament contacts for the experimental versus randomized data at both time points (Figure 3.4E). The randomized distributions at both time points demonstrated fewer end-localizations and increased numbers of contacts along the body of the filament in comparison to quantification of localization data from true images (Figure 3.4E, $p = 1.10 \times 10^{-11}$ and 2.01×10^{-16} at 20 min and 40 min, respectively). These results indicate that the preference for autophagosomes to localize at or near filament ends is non-random.

Taken together, the results from Figure 3.2 and Figure 3.4 indicate that following TCR engagement and activation, autophagosomes formed attachments with Bcl10 filaments, the number of attachments increased over time, and these attachments occurred near the ends of Bcl10 filaments. Furthermore, by 40 min post-activation, autophagosomes also formed attachments with Bcl10 punctate structures in a biologically targeted (i.e., non-random) manner. Together, these results

are consistent with the hypothesis that autophagosomes are responsible for the progressive shortening of Bcl10 filaments over time, and that this process is directed by a biologically encoded targeting process. Further, the accumulation of punctate Bcl10 structures at 40 min post-activation may be the result of the degradation of longer Bcl10 filaments. Complete degradation of Bcl10 may follow nonlinear kinetics, with the final remnant, visualized as puncta, undergoing slower degradation than filamentous regions of these structures.

3.3.3 Modeling Bcl10 Filament Dynamics

Our previously published observations demonstrate that macroautophagy contributes to Bcl10 filament degradation [36], and the above analysis of imaging data supports and extends these conclusions. This degradation occurs simultaneously with Bcl10 polymerization, and the interplay between these processes serves to control T-cell activation states. However, our understanding of the dynamics of filament polymerization and degradation, and the interaction between these processes, remains limited.

To explore the interplay between simultaneous Bcl10 polymerization and degradation further, as well as the implications of this interplay, for control of T-cell activation states, we designed a stochastic Monte Carlo simulation to model Bcl10 polymerization (Methods). Previous studies have indicated that growth of Bcl10 filaments is nucleated by short cytosolic oligomers of Carma1 [8, 62], and that this nucleation is the rate-limiting step for filament growth [8]. Thus, we used nucleation-

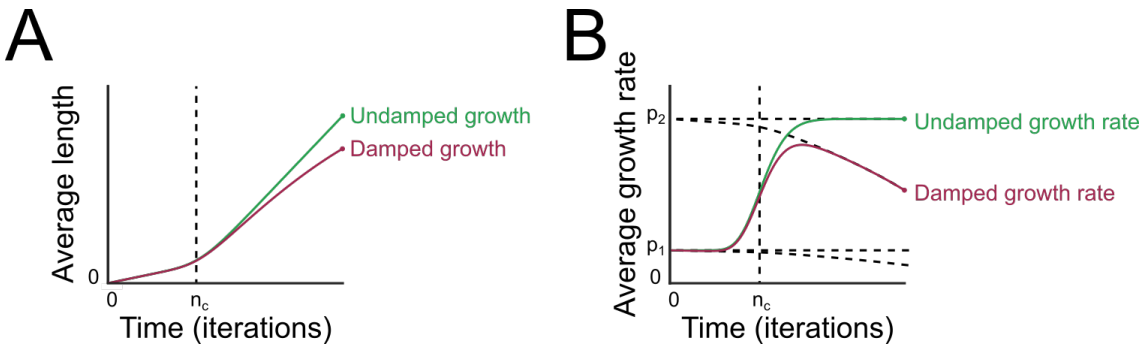

Figure 3.5: Theoretical predictions of nucleation-limited growth. (A) Expected length of filaments undergoing nucleation-limited growth in damped (red) and undamped (green) environments. (B) Expected growth rate of of filaments undergoing nucleation-limited growth in damped (red) and undamped (green) environments.

limited filament assembly as the basis for our simulation. The growth rates of filaments that undergo nucleation-limited growth are governed by whether filament lengths are less than or greater than the nucleation barrier. Short filaments grow slowly until they reach the critical length.. In effect, growth rates of such filaments can be understood as a sequence of Bernoulli processes whose probability parameter is modified based on current filament length. Under these conditions, theoretical predictions of filament growth rate indicate a dramatic transition between slow, initial growth, to fast, steady-state growth, as outlined in Equation 3.1 and Figure 3.5.

$$P(x|n) = \begin{cases} \binom{n}{x} p_{attach}^{x} q_{attach}^{n-x} & x < L_0 \\ \sum_{i=L_0}^{n-(x-L_0)} \binom{i-1}{L_0-1} p_{attach}^{L_0} q_{attach}^{i-L_0} \binom{n-i}{x-L_0} p_{grow}^{x-L_0} q_{grow}^{(n-i)-(x-L_0)} & x \geq L_0 \end{cases} \tag{3.1}$$

Filament growth is further mediated by a kinetic process whereby monomers

collide with, or are recruited to, the site of the growing filament. Our simulation began with the generation of cells, which were each given a random size that was used to generate the initial conditions, including numbers of monomeric nucleation-site components (mimicking monomeric Carma1), Bcl10, autophagosomes, and the size of the immunological synapse (i.e., the portion of the cell membrane with the potential to activate the Bcl10-nucleation sites). As this cell evolved in time over each iteration of the simulation, the growth of Bcl10 filaments was governed by three independent and tunable parameters (visually represented in Figure 3.6A): the activation probability of the nucleation sites ($p_{activate}$), the growth probability of the initial layer of Bcl10 monomers before the nucleation barrier has been overcome (p_{attach}), and the steady-state growth probability after the filament overcomes the nucleation barrier (p_{grow}).

We first sought to determine whether the value of each parameter should remain constant throughout each iteration of the simulation, or whether the results of each iteration would affect parameter values. For instance, if the concentration of free Bcl10 monomers decreases over time (i.e., if resynthesis of Bcl10 monomers is outpaced by their degradation), the probability of monomer collisions with the growing filament end decreases over time, thus decreasing p_{grow}, in a process known as damping. To determine whether Bcl10 filament growth is damped, we tested 100 simulated T cells, each with a different size, and thus initialized with a unique number of nucleation sites and Bcl10 monomers, representing the evolution of a heterogeneous population of T cells with varying initial conditions (Figure 3.6B). When our simulation were employed in an undamped environment, growth contin-

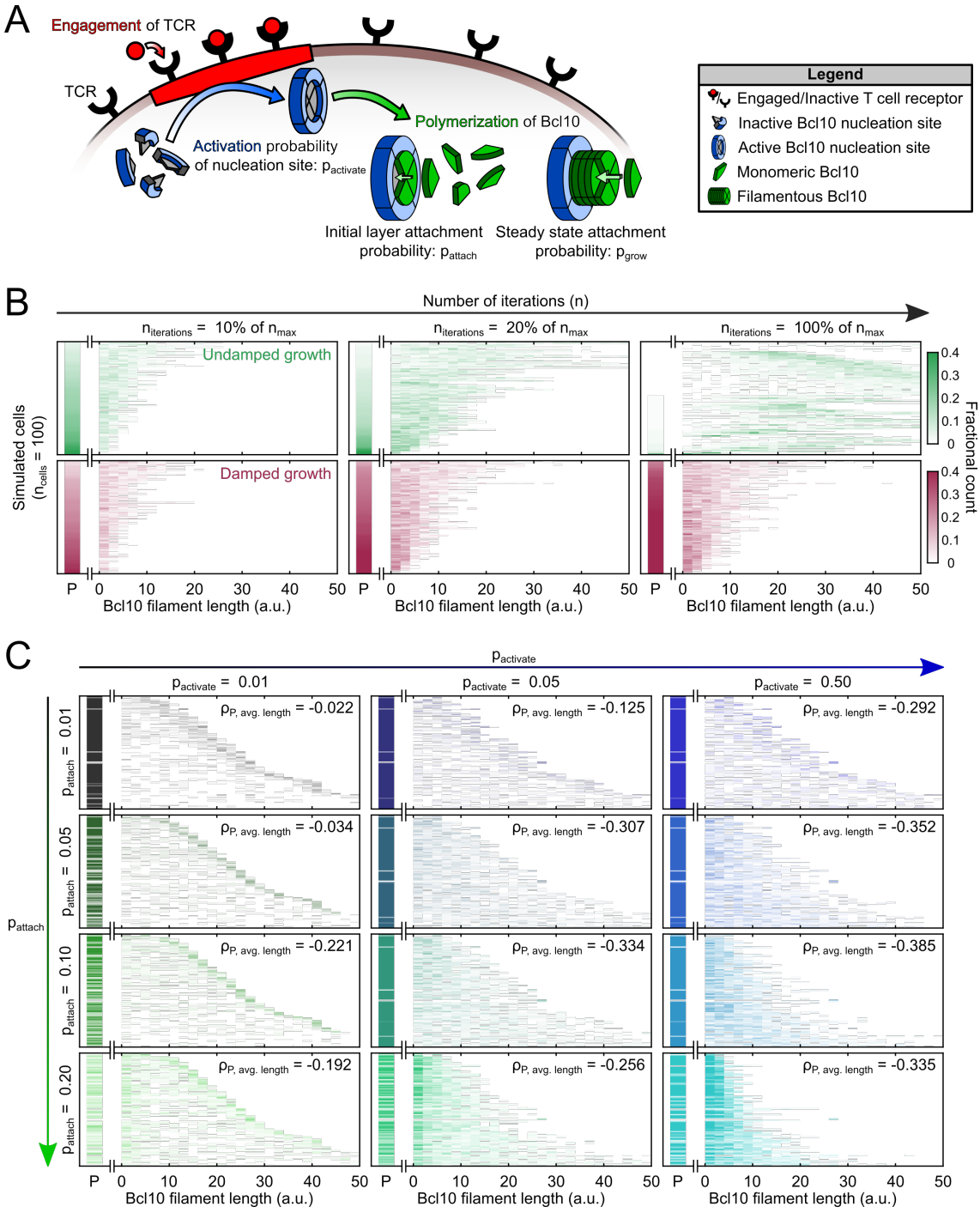
A
Engagement of TCR
TCR
Activation probability of nucleation site: $p_{activate}$
Polymerization of Bcl10
Initial layer attachment probability: p_{attach}
Steady state attachment probability: p_{grow}
Legend
Engaged/Inactive T cell receptor
Inactive Bcl10 nucleation site
Active Bcl10 nucleation site
Monomeric Bcl10
Filamentous Bcl10
B
Number of iterations (n)
$n_{iterations}$ = 10% of n_{max}
$n_{iterations}$ = 20% of n_{max}
$n_{iterations}$ = 100% of n_{max}
Undamped growth
Damped growth
Simulated cells (n_{cells} = 100)
Fractional count
Bcl10 filament length (a.u.)
C
$p_{activate}$
$p_{activate}$ = 0.01
$p_{activate}$ = 0.05
$p_{activate}$ = 0.50
p_{attach}
p_{attach} = 0.01
p_{attach} = 0.05
p_{attach} = 0.10
p_{attach} = 0.20
$\rho_{P, avg. length}$ = -0.022
$\rho_{P, avg. length}$ = -0.125
$\rho_{P, avg. length}$ = -0.292
$\rho_{P, avg. length}$ = -0.034
$\rho_{P, avg. length}$ = -0.307
$\rho_{P, avg. length}$ = -0.352
$\rho_{P, avg. length}$ = -0.221
$\rho_{P, avg. length}$ = -0.334
$\rho_{P, avg. length}$ = -0.385
$\rho_{P, avg. length}$ = -0.192
$\rho_{P, avg. length}$ = -0.256
$\rho_{P, avg. length}$ = -0.335
Bcl10 filament length (a.u.)

Figure 3.6: Simulations of Bcl10 filament growth reveal properties of real Bcl10 nucleation rates and concentrations, but fail to match observed values for ρ. (A) Representative segmented Bcl10 filaments (green) and autophagosomes (red) after post-processing overlaid with the pruned medial-axis skeleton of Bcl10 (black). Filament skeletons were fragmented to minimize the bending energy at junctions. (B) Using the skeleton of the representative Bcl10 filament, the filament volume was segmented into sections based on the nearest distance from skeleton ends. (C) Distribution of autophagosome-Bcl10 contacts by distance from endpoint (filamentous Bcl10) or punctate Bcl10 (P). (D) Scatter-bar plot of the proportion of Bcl10 puncta per cell in contact with an autophagosome in experimental and randomized data. (E) Distribution of autophagosome-filamentous Bcl10 colocalizations by distance from endpoint in experimental and randomized data. p-values in (C) and (E) were calculated using two-sample K-S tests and p-values in (D) were calculated using paired two-sample t-tests. p-values less than 0.05 were considered significant.

ued perpetually and, by the end of the simulation, punctate structures all grew into filaments and all Carma1-mimicking nucleation sites were filled. The same simulation in a damped environment, with a finite supply of Bcl10 monomers, led to a heterogeneous distribution of Bcl10 puncta and filaments of varying lengths. The results of the damped growth simulation were more representative of observed Bcl10 filament lengths (Figure 3.1D), leading us to conclude that Bcl10 filament growth is limited by Bcl10 monomer supply. This conclusion is supported by biochemical analyses of Bcl10 levels over time in activated T cells [36]. Thus, in all subsequent simulations, we allowed the decreasing availability of monomeric Bcl10 to cause an effective stochastic reduction in the Bcl10-nucleation probabilities, p_{attach} and p_{grow}, because fewer monomeric Bcl10 will lead to a reduced number of attempted attachments.

Next, we tested whether changes in the value of p_{grow} would provide useful information regarding the response dynamics. Previous work by David et al. [8] indicated that nucleation ($p_{activate}$) and/or the initial attachment of Bcl10 filaments (p_{attach}) is the rate-limiting step in filament growth. Thus, varying the value of p_{grow} would likely provide little in the way of relevant biological information. Furthermore, increasing the growth rate would more quickly deplete the monomer concentration, thus ending the simulation after fewer iterations and limiting the sampling of the activation and attachment probabilities. Thus, we chose to assign p_{grow} a fixed value that allowed the simulations to run for a reasonable number of iterations (here, we chose p = 0.4 as described in the Methods), and we only modulated $p_{activate}$ and p_{attach}.

Finally, we examined the effect of various values for $p_{activate}$ and p_{attach} on filament lengths resulting from the simulation (Figure 3.6C). The observed filament lengths in our cell images (Figure 3.1D) demonstrate a moderately negative correlations between the relative numbers of puncta and length of Bcl10 filaments, ρ ¡ -0.6. We therefore explored which combinations of parameters applied to the same heterogenous population of 100 simulated T cells could generate an equivalent correlation. Each simulation was repeated 10 times, and each trial was terminated when the number of free monomers of Bcl10 reached zero. The filament-length distributions we report represent the cumulative distribution from each of the 10 trials. There is a complex interplay between $p_{activate}$ and p_{attach}: when $p_{activate}$ is small, there are few simulated filaments, and simulated filament length distributions appear to be unchanged with increasing p_{attach} (Figure 3.6C left). On the other hand, when $p_{activate}$ is large, there are many activated nucleation sites in each simulated cell, which results in heterogeneity in the preferred filament length. Increased p_{attach} results in decreased average-filament length (Figure 3.6C right). Interestingly, intermediate values of $p_{activate}$ in the simulations results in nonlinear behavior (Figure 3.6C center). In particular, the preferred filament length appears to be independent of p_{attach} for small p_{attach}, similar to Figure 3.6C left, but decreases for large p_{attach}, similar to Figure 3.6C right. Careful tuning of simulations parameters resulted in correlations between ρ = [-0.5, -0.4] in subsections of the simulation's parameter space in which $p_{activate}$ was 0.5, and p_{attach} was 0.075. However, the minimum ρ value in the simulation was unable to reach observed levels of ρ less than -0.6. This failure to match the model to experimental observations points to a need

to include Bcl10 degradation in the simulations.

To understand the effect of degradation on Bcl10 filament size, we added a process in the simulation in which an autophagosome attaches to a filament and cause degradation with probability $p_{degrade}$ (Figure 3.7A). As in Figure 3.6, we simulated 100 cells with random initial conditions and repeated each simulation 10 times. A comparison of twelve representative parameter sets is instructive for determining the effects of each individual parameter, as well as of the interplay among the parameters, on the concentration of filamentous Bcl10 (Figure 3.7B). For this set, we chose a small vs a large value for both p_{attach} (Figure 3.7B, top vs bottom) and $p_{activate}$ (Figure 3.7B, left vs right). For each of these four parameter subspaces, we compared a small, medium, and large value for $p_{degrade}$, which was varied over the same range as p_{attach}. As expected, increasing values of $p_{degrade}$ in each parameter space led to a smaller concentration of filamentous Bcl10. Interestingly, an increase in the rate of nucleation-site generation (represented by a greater $p_{activate}$) led to a faster decline in filamentous Bcl10 (Figure 3.7B, left vs right). This result makes intuitive sense, as a greater number of activation sites would lead to a greater number of filaments, and thus a greater number of sites where degradation can occur. In contrast, a lower activation barrier (represented by a greater p_{attach}) had a much smaller effect on the rate of decline in filamentous Bcl10, promoting only a slight increase in filament stability. When combined, a lower activation barrier and a greater activation of nucleation sites created a dynamic in which slight variations in degradation had a large effect on the concentration of filamentous Bcl10.

We further explored how each of the three parameters in our simulation af-

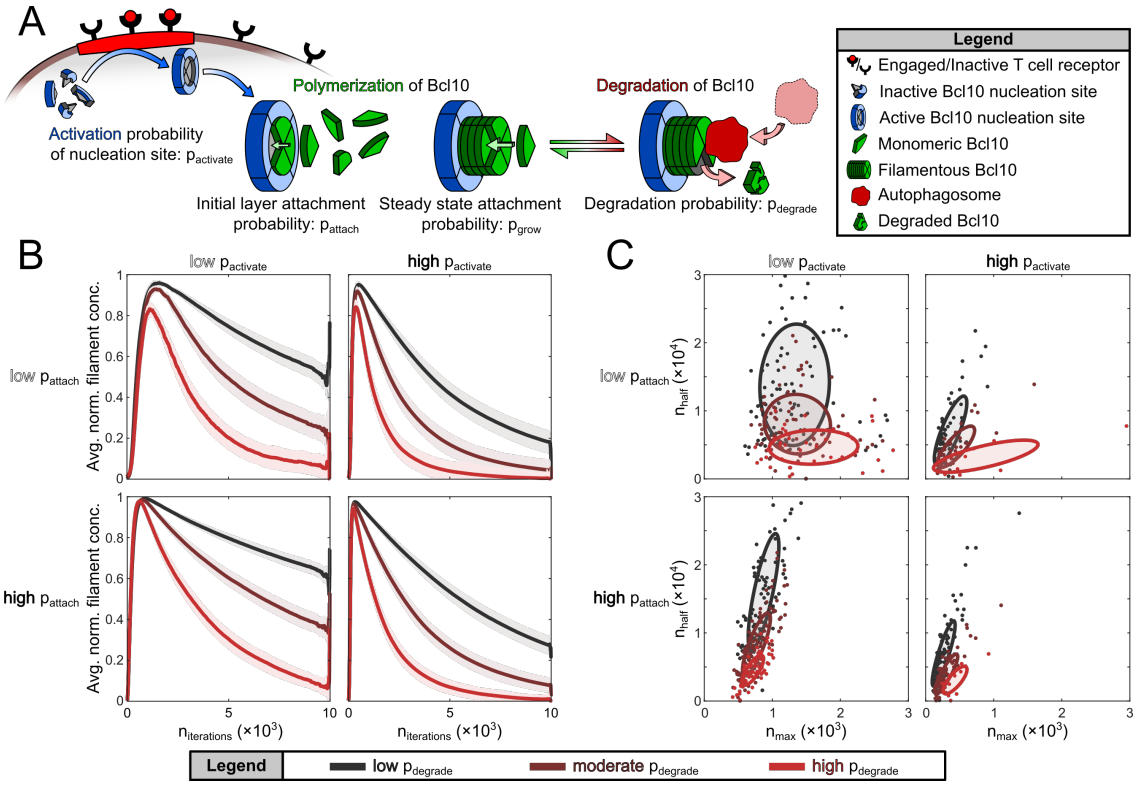

Figure 3.7: Simulations of Bcl10-filament growth and decay demonstrate that changes in the response dynamic due to increasing degradation by autophagy were stabilized by increasing p_{attach} but emphasized by increased $p_{activate}$. (A) Bcl10-filament degradation was simulated in conjunction with filament growth. Degradation was modulated by $p_{degrade}$, the probability of degradation by an autophagosome. (B) The average normalized concentration of filamentous Bcl10 as simulations evolved. Concentration is relative to the maximum-average concentration of all simulations with the same parameters. Each line represents the average of 100 cells, repeated 10 times each, and shaded bars are the 95% CI of the mean. Simulations were repeated with small and large values for $p_{activate}$ and p_{attach}. (C) The number of iterations needed to reach the maximum relative concentration vs. the number of iterations to reach half of the maximum concentration due to degradation. Each entry represents the average n_{max} and n_{half} for the 10 trials of each of the 100 cells. Low $p_{degrade}$ is 0.05, moderate $p_{degrade}$ is 0.10, and high $p_{degrade}$ is 0.20. Ellipses represent one standard error of the mean.

fected the variability of the response across the heterogeneous initial population of cells (Figure 3.7C). For each of the 100 cells, we calculated the average number of iterations for the filament-length distribution to reach its maximum average size, n_{max}, and compared this to the average number of iterations required for the average size to be half of the max, n_{half} (Figure 3.7C), for each of the twelve parameter configurations. Increasing the value of p_{attach}, $p_{activate}$, or $p_{degrade}$ independently of the others led to decreased variability in outcomes, with a lower nucleation barrier (an increase in p_{attach}) having the greatest effect on variability in the response to an activation signal (i.e., heterogeneity in the time to peak response), and an increase in $p_{activate}$ emphasizing changes in $p_{degrade}$. The introduction of degradation into the simulations reduced the already negative correlations ρ between the number of puncta and average filament length. Each of the simulations reached values of $\rho \approx$ -0.5 during system evolution, close to the experimental value of $\rho < -0.6$.

In summary, we have developed a refined model of a critical TCR signaling process that quantitatively captured the growth and decay dynamics of Bcl10 filaments and their heterogeneous length distribution. We determined that a high activation potential of nucleation sites can, when combined with a low Bcl10-nucleation barrier, provide the most predictable and homogeneous response to T-cell activation. Furthermore, we found that the rate of degradation of Bcl10 filaments had the largest effect on the percentage of Bcl10 in filamentous form when nucleation sites have a high activation potential and Bcl10 has a low nucleation barrier. These conditions ultimately allow the response dynamic to be maximally tunable via changes in the degradation rate. These data offer a mechanistic explanation for the opposition of

Bcl10 polymerization by simultaneous autophagic degradation of Bcl10 polymers.

3.4 Discussion

In this work, we explored the mechanism and dynamics of Bcl10 filament degradation, a process that is a key regulatory element in the T cell receptor-to-NF-κB signal transduction pathway. Through computational analysis of super-resolution images, we demonstrated that Bcl10 filaments are shorter in length at 40 min post-TCR engagement than at 20 min, with an increase in punctate Bcl10 and a decrease in filaments longer than 1 μm. We demonstrated that autophagosomes were preferentially in contact with Bcl10 filaments, that these contacts increased over time, that at both 20 min and 40 min post-TCR engagement there was a preference for the contacts to occur near filament ends, and that by 40 min post-TCR engagement, autophagosomes colocalize with Bcl10 puncta in non-random, significant manner. Together, these findings, along with our previous biochemical studies [36], imply that autophagosomes drive a degradative process that progressively shortens Bcl10 filaments, leaving behind remnants visualized as puncta that undergo slower degradation. Furthermore, we developed a stochastic Monte Carlo simulation of nucleation-limited filament growth and degradation, which we used to probe aspects of regulatory control of filamentous signal transduction bodies.We ascertained that the rate of degradation was the most important element controlling the magnitude and dynamics of the response function, particularly when the homogeneity of the response has been maximized via a high activation potential and a

low nucleation barrier.

Importantly, these results shed light on possible mechanisms of autophagic degradation in the poorly understood scenario in which the structures to be degraded are larger than the autophagosomes performing the degradation. We found that increased contact between autophagosomes and Bcl10 filaments corresponded to a progressive shortening of Bcl10 filament length, implying that autophagosomes degrade these large structures through a piecewise mechanism rather than by enclosure of the entire volume of a given cargo. Furthermore, we determined that filaments to which autophagosomes attached were more likely to experience attachment near filament ends, and that degradation models that target the ends of filaments rather than the mid-region best fit the experimental observations. However, we were unable to establish whether this degradation might occur via end-based disassembly at the molecular scale, or via scission of larger regions near the end. The observation that the number of punctate structures in contact with autophagosomes increases significantly at 40 min vs 20 min could not be recapitulated in our model, indicating that the final degradation of Bcl10 filaments once they reach lengths less than 150 nm, and thus appear as punctae, is inhibited or occurs by an independent mechanism.

The analysis methods that we developed for this study have broad applicability to computational image analysis and the study of dynamic signaling processes. Typically, radial-distribution functions are used to measure and statistically assess contacts and/or colocalizations between structures. However, because contacts between Bcl10 filaments and autophagosomes involve close-range contact and significant vol-

umetric overlap, such an analysis was not suitable. Our image-based bootstrap-like method of random rearrangement and reanalysis of segmented objects could prove to be widely applicable in assessing colocalizations between structures in an image. Furthermore, filamentous signaling structures, particularly those whose core constituent protein contains a death domain superfamily element (as Bcl10 does), are a common motif in immunological signal transduction pathways [107–109], and many are downregulated via macroautophagy [110–112]. Thus, our model of nucleation-limited filament growth and degradation, with its multiple tunable parameters that can be used to fit the model to observed imaging data, may be applicable to a variety of autophagy-regulated signal transduction pathways and reveal common mechanistic principles of immune regulation.

The simulations we developed offer intriguing insight into the regulatory control of T cell activation states. Higher values of $p_{activate}$ in the model led to increased heterogeneity in filament lengths. Because our experimental observations include heterogeneous filament lengths, it is implied that the probability of activation of Carma1 in response to TCR engagement is realistic biologically. Furthermore, higher values of $p_{activate}$ in the model led to increased responsiveness to variations in degradation speed, along with decreased variability of the response from a variety of initial states; outcomes that are both beneficial to the overall control of T cell activation. Thus, it appears that in activated T cells, Carma1 in the vicinity of the immunological synapse has a high likelihood of promoting Bcl10 filament nucleation, and further regulatory control of the activation potential of Carma1 would provide little overall benefit. In contrast, variations in the size of the nucleation

barrier (represented by p_{attach}) had little effect on the dynamics of the response, although a smaller nucleation barrier (higher p_{attach}) led to slightly stabilized filaments over time and increased homogeneity of the response dynamic. Regulatory control of the nucleation barrier does not appear to provide substantial benefit to the response dynamic. Interestingly, based on the results of the simulations, governing the rate of filament degradation via control of autophagy has the greatest effect on the response dynamic. Indeed, autophagy has many regulatory control points and processes feedback from a wide variety of signaling pathways [113], providing myriad opportunities for crosstalk among T-cell signaling inputs.

The results of our simulations indicate that POLKADOTS filament growth and degradation exhibit the characteristics of an excitable system. Excitability is a phenomenon by which a system can undergo dramatic changes in behavior in response to small perturbations. Components of such a system typically include nonlinear thresholded/digital activation that initiates a fast, amplifying, positive feedback loop, and a slower, delayed, response-limiting negative feedback loop [3]. Excitable systems characteristics are observed in a variety of biological processes, including in the polymerization and depolymerization of cytoskeletal proteins during migration [9], and in ion channels during neuronal firing cascades [114]. Further, excitability is often observed when signaling networks reach a critical, near-phase-transition state [5,13], which induces dramatic changes to system dynamics, including the oligomerization of protein complexes via phase separation [12]. We have previously reported that the Bcl10-dependent TCR-to-NF-κB signaling pathway is characterized by digital activation, with increased stimulus beyond a certain thresh-

old having little effect on the signaling response of individual T cells [104]. Thus, the predictions of behavior of POLKADOTS filament growth and degradation resulting from these simulations are consistent with our previous observations of the biological behavior of these signaling elements in T cells.

Our analysis of Bcl10 filament formation and degradation suggest that this self-limiting, all-or-nothing response is enabled by nucleation-limited filament assembly with a high probability of Carma1 activation in response to even minimal TCR engagement and a low nucleation barrier. The system is self-limiting via autophagy operating on filament ends, which extends the lifetime of filaments and thus signal activation (a result not inconsistent with autophagy limiting the intensity of the signal by limiting the amount of Bcl10 in POLKADOTS filaments [36]). Disassembly via autophagy results in a long refractory period due to protein degradation. More broadly, our results, when considered in combination with existing structural data [105], offer the possibility that spatial organization of signaling components, specifically filament assembly and degradation, may be used in other biological signaling networks to enable robust all-or-nothing responses and/or self-limiting dynamics.

3.5 Materials and Methods

3.5.1 T-Cell Stimulation and Imaging

D10.G4.1 T cells were transduced with retroviruses-expressing Bcl10-GFP and TagRFP-T-LC3 (referred to as RFP-LC3) as previously described [115]. Following

antibiotic selection, cells were subcloned to ensure uniform imaging characteristics. The resultant D10 cell line was activated via plating on coverslips coated with anti-CD3 antibody (clone 145-2C11, BioXCell). Cells were fixed with 3% paraformaldehyde after the indicated incubation times and mounted for imaging on a custom-built instant structured illumination microscope (iSIM) with a 1.45 NA oil-immersion objective [106]. Images were collected as z-stacks inclusive of the entire volume of the cells with a 200 nm distance between z planes. Following collection, images were deconvolved using the Richardson-Lucy algorithm as previously described [106] and converted to a new isotropically-distributed 3-D coordinate grid via 3-D spline interpolation.

3.5.2 Segmentation of Bcl10 and LC3

Fluorescent iSIM images of Bcl10 and LC3 were binarized using an intensity threshold on a cell-by-cell and channel-by-channel basis due to fluctuations in expression and intensity. Each binarized image was convolved with a $3 \times 3 \times 3$ kernel with values $\frac{1}{3^3}$ and again binarized with a threshold of $(\frac{2}{3})^3$ so that pixels with at least 8 occupied nearest neighbor locations were considered. All small binary pixel-noise was removed. Colocalizations between Bcl10 and LC3 were determined by identifying the voxels which directly overlap in the two binary channels.

3.5.3 Skeletonization and Skeleton Measurements of Bcl10

Each of the structures in the binary Bcl10 images was individually skeletonized using a MATLAB implementation of medial-axis thinning skeletonization [116,117]. Bcl10 skeletons sometimes contained erroneous spurs due to fluctuations in the volume from sensitivity to the intensity threshold. Thus, filament skeletons were processed by iteratively removing spurs less than 6 voxels (150 nm) in end-to-end length, the approximate optical resolution of the iSIM. Structurally isolated skeletons less than 6 pixels (150 nm) in length were labeled as punctate as indicated in Figure 3.1.

Where multiple Bcl10 filaments overlapped, skeletons developed high-degree nodes in which multiple filament branches converged or intersected at a single branch point. This type of Bcl10 filament structure is inconsistent with current perspectives [8], and was treated as an imaging artifact. To estimate the appropriate skeleton segmentation in these regions, we instituted a minimum-bending-energy scheme under the assumption that filaments are less likely to develop large curvature, and thus chose the configuration that resulted in the smallest net bending energy. Bending energy for a simple elastic beam is proportional to $\frac{1}{R^2}$, where R is the radius of curvature of the bent region. Thus, we fit an 11-pixel segment centered at the high-degree junction between multiple skeletons to the surface of a sphere to calculate R for the segment.

Measurements from the ends of skeletons were calculated using the Floyd-Warshall algorithm where the reference point was the nearest degree-one node. Colocalizations between Bcl10 and LC3 were assigned the end-distance value from

the nearest skeleton points in all overlapping voxels.

3.5.4 Random Rearrangement and Resampling of Segmented Structures for Statistical Assessment

Bootstrapping is a statistical resampling procedure that allows for the estimate of a sampling distribution. Because resampling of a single fixed T cell at 20 min or 40 min post-activation is impossible, we developed an image-based resampling method to assess the sample distributions for the number and location of Bcl10-autophagosome contacts if the underlying biological processes are driven by randomness.

To implement the procedure, we identified three relevant cell structures from the 3-D super-resolution iSIM image: the cell boundary, binary Bcl10, and binary autophagosomes. For the resampling, we kept the location of the cell boundary and Bcl10 fixed. Then, we removed all autophagosomes from the image and separately saved each individual 3-D structure. Each 3-D autophagosome was then rotated by three randomly generated angles between 0 degrees and 360 degrees about the x-, y-, and z-axes. Finally, each randomly rotated autophagosome was placed one at a time in a random location within the cell boundary. If any voxel in the currently selected autophagosome fell outside of the boundary or overlapped with an existing autophagosome, then a new location was chosen. The procedure was repeated until all autophagosomes were placed. Upon completion, the contact calculations were repeated, including the number of Bcl10-autophagosome contacts per cell, and the

location of each of the contacts along connected Bcl10-filament skeletons.

3.5.5 Simulations of Bcl10 Filament Growth and Degradation

Simulated cells were initialized with a variable amount of monomeric Bcl10, monomeric Carma1, and autophagosomes. To determine initial levels, each cell was assigned four random radii, R_1, R_2, R_3, and R_4, from a normal distribution with parameters $\mu = 1$ and $\sigma = 0.2$. The initial amount of Carma1 was $a_0 \times R_1^3$, Bcl10 was $b_0 \times R_2^3$, autophagosomes were $c_0 \times R_3^3$, and the size of the immunological synapse was $d_0 \times R_2^2$, where $a_0 = 10$, $b_0 = 500$, $c_0 = 5$, and $d_0 = 0.2$, were each chosen empirically.

The simulated evolution of filament growth and degradation was controlled by the activation of Carma1 by the engaged TCR, the nucleation of Bcl10 filaments by an active Carma1, the attachment of monomeric Bcl10 to nucleated Bcl10 filaments, the attachment of autophagosomes to Bcl10 filaments, and the degradation of Bcl10 filaments by autophagosomes. Each step in the evolution was mediated by both fixed and variable probabilities.

1. Activation of Carma1 by the engaged TCR.
   (a) Probability that Carma1 will collide with the TCR, $p_{collide} = 0.1$.
   (b) Probability that the TCR was part of the immunological synapse, $p_{synapse} = d_0 \times R_4^2$.
   (c) Probability of Carma1 activation, $p_{activate}$ (variable).
2. Growth of Bcl10 on activated Carma1.

(a) Probability that Bcl10 will collide with Carma1, $p_{collide} = 0.01$.

(b) Probability of attachment before the nucleation barrier has been reached, p_{attach} (variable).

(c) Size of the nucleation barrier (i.e., the number of attachments before the attachment probability switches from p_{attach} to p_{grow}), $n_{barrier} = 20$.

(d) Probability of attachment after the nucleation barrier has been reached, $p_{grow} = 0.4$.

3. The degradation of Bcl10 by an attached autophagosome.

(a) Probability of autophagosomes colliding with a Bcl10 filament, $p_{collide} = 0.01$.

(b) Probability of autophagosomes attaching to a Bcl10 filament, $p_{attach} = 0.1$.

(c) Probability of autophagosomes degrading attached-to filaments, $p_{degrade}$ (variable).

(d) If attached autophagosomes do not degrade, the probability that they fall off the attached-to filament, $p_{detach} = 0.1$

We used physical properties of Carma1 and Bcl10 to inform the interaction probabilities in the simulations. Bcl10 has a mass of 33 kDa and its cytosolic diffusion constant is on the order of $D_{Bcl10} \approx 10\frac{\mu m^2}{s}$, whereas Carma1 has a mass of 130 kDa, and thus has a cytosolic diffusion constant on the order of $D_{Carma1} \approx 1\frac{\mu m^2}{s}$ [118]. The time required to traverse some mean-squared displacement d via diffusion

is $t \approx \frac{d^2}{6D}$. T-cell diameters are on the order of $d_{Tcell} \approx 10\mu m$, and thus the time it takes for Bcl10 and Carma1 molecules to traverse the cytosol are approximately 0.2 sec and 2 sec, respectively. Thus, the collision probability for Bcl10 was chosen to be 10× larger than that of Carma1. The other rate constants, such as p_{grow} and p_{attach}, have not been determined experimentally, to our knowledge.

Simulations from Figure 3.6 were performed without autophagosomes and terminated upon monomeric Bcl10 being completely converted to filamentous Bcl10. Simulations from Figure 3.7 were performed for either 10,000 iterations or when the number of monomeric and filamentous Bcl10 reached zero, whichever came first.

Chapter 4: Quantifying Topography-Guided Actin Dynamics Across Scales Using Optical Flow

This chapter was adapted from Lee*, Campanello*, Hourwitz, Alvarez, Omidvar, Fourkas, and Losert [6]. Text and figures were reproduced under a Creative CommonsNoncommercialShare Alike 3.0 Unported license. Rachel Lee, Matt Hourwitz, and Phillip Alvarez performed the MCF10A experiments, Matt Hourwitz and Ava Omidvar performed the HL60 experiments, Leonard Campanello designed and performed the optical-flow analysis, and Rachel Lee and Leonard Campanello wrote the paper.

4.1 Overview

The dynamic rearrangement of the actin cytoskeleton is an essential component of many mechanotransduction and cellular force generation pathways. Here we use periodic surface topographies with feature sizes comparable to those of *in vivo* collagen fibers to measure and compare actin dynamics for two representative cell types that have markedly different migratory modes and physiological purposes: slowly migrating epithelial MCF10A cells, and polarizing, fast-migrating, neutrophil-like

HL60 cells. Both cell types exhibit reproducible guidance of actin waves (esotaxis) on these topographies, enabling quantitative comparisons of actin dynamics. We adapt a computer-vision algorithm, optical flow, to measure the directions of actin waves at the submicron scale. Clustering the optical flow into regions that move in similar directions enables micron-scale measurements of actin-wave speed and direction. Although the speed and morphology of actin waves differ between MCF10A and HL60 cells, the underlying actin guidance by nanotopography is similar in both cell types at the micron and submicron scales.

4.2 Background

Understanding the rearrangements of the cytoskeleton is essential to developing a complete picture of the dynamic forces involved in cellular processes such as migration, division, and differentiation. Cytoskeletal dynamics, and in particular actin dynamics, have been shown to be important for the growth of cell junctions and focal adhesions [68] and for immune-cell activation [27]. The formation of actin waves through directional polymerization and depolymerization of filaments drives many types of cell migration [119], and has been associated with the establishment of polarity in a variety of cell types [120].

Forces from the extracellular environment are an important modulator of actin dynamics. Physical and chemical characteristics of the extracellular environment, such as rigidity, biochemical composition, and topography, have been shown to influence actin dynamics and associated cell behavior [121–124]. One mechanism

for this modulation is mechanosensing via focal adhesions [39]. In addition, actin waves respond when cells encounter obstacles [125]. It has been established that ridges of width comparable to fibers in the extracellular matrix (ECM) can alter actin dynamics significantly [29, 38, 39] and bias the localization of focal adhesions [126, 127]. Thus, *in vivo*, the topography of the ECM, such as collagen networks [128, 129], is likely to modulate actin dynamics.

Periodic nanotopographic surfaces provide the opportunity to obtain systematic data on the modulation of such intracellular dynamics. In prior work, we have shown that actin waves can be nucleated near, and guided along, periodic nanotopography, in a phenomenon termed esotaxis. Actin-wave guidance has been observed in cell types that exhibit distinct physiological functions and migration phenotypes, including *Dictyostelium discoideum* [29,38], neutrophil-like HL60 cells [38], B cells [39], and breast-cancer cell lines [24]. However, there are clear differences in the responses of each of these cell types to nanotopography. For example, although both *D. discoideum* and HL60 cells exhibit esotaxis, these two types of cells have been found to move preferentially in different directions on specific nanoscale asymmetric sawtooth textures [38]. Furthermore, different breast cancer cell lines preferentially move in different directions on asymmetric sawtooth nanotopography [24].

Here we introduce a method for performing quantitative measurements of the influence of nanotopography on intracellular dynamics at both the submicron and the micron scales. This approach enables the detection of subtle differences in cytoskeletal dynamics, and allows for in-depth analysis of both the differences and the similarities of these dynamics across cell types and phyla. Our method of quantifi-

cation of actin dynamics across scales is based on optical flow, an image-analysis technique developed in the fields of robotics and navigation control that uses changes in pixel intensities to detect motion in image sequences [87,89]. Because of the popularity of particle image velocimetry (PIV), optical flow has seen limited use on biological images. However, PIV is poorly suited for the variety of features that can be exhibited in fluorescence images of amorphous concentration fields. Indeed, a recent study indicated that optical flow may be better suited for analysis of fluorescence images, as it provides a more accurate estimate of ground-truth flow fields [84]. Here, we use optical flow to measure the dynamics of actin polymerization with submicron precision, and we further expand the utility of optical flow by introducing modeling and fitting approaches to the analysis of optical-flow vector fields. Clustering of the optical-flow data further allows us to quantify actin dynamics on the micron scale. This optical-flow-based analysis enables the identification of similarities and differences between esotaxis in neutrophil-like HL60 cells and human breast epithelial MCF10A cells across length scales.

4.3 Results

Esotaxis has been observed in a wide range of cell types that are known to respond to their *in vivo* microenvironment through processes such as directed migration or immune-system activation [29, 38, 39]. More recently, esotaxis has also been observed in epithelial cells, which are not motile [24]. Here we contrast the actin dynamics of epithelial MCF10A cells with those of neutrophil-like HL60 cells.

LifeAct-GFP-labeled epithelial MCF10A cells were plated on a 900 μm $\times$ 900 μm region patterned with parallel nanoridges with a spacing of 1.5 μm, as well as on the surrounding flat regions. Confocal imaging near the surface revealed distinct actin morphologies on nanoridges as compared to on the flat region (Figure 4.1). On the flat regions the phenotype was a common one for MCF10A, with a broad lamellipodium at the cell front and stress fibers throughout the cell body (Figure 4.1A). In contrast, MCF10A on nanoridges exhibited actin streaks aligned with the ridges throughout the cell area (Figure 4.1B). The local nature of the responses of actin to the surface texture is illustrated in Figure 4.1C, which shows a cell that was partially on the nanoridges and partially on the flat region. On the nanoridged region, the cell showed the same types of actin streaks as a cell that was fully on a ridged surface, whereas the same cell maintained a broad lamellipodium on the flat region.

Ridged and flat regions also engender distinct actin dynamics. Kymographs were used to visualize dynamics in regions of interest in one spatial direction over time. The left side of Figure 4.2A compares an MCF10A cell on a flat region with one on a nanoridged region. The cell on the nanoridged region exhibited actin streaks that are characteristic of esotaxis. Actin kymographs from two perpendicular regions (Figure 4.2A) in an MCF10A cell on a flat surface show oscillatory dynamics in all directions at the cell boundary. These oscillations in the kymographs indicate the presence of fanlike protrusions and retractions across each region over 30 min (Figure 4.2B). In contrast, on the nanoridged region, the actin dynamics parallel and perpendicular to the ridges were different (Figure 4.2C). Parallel to the nanoridges, MCF10A cells exhibited oscillatory actin dynamics. As shown in the bottom left

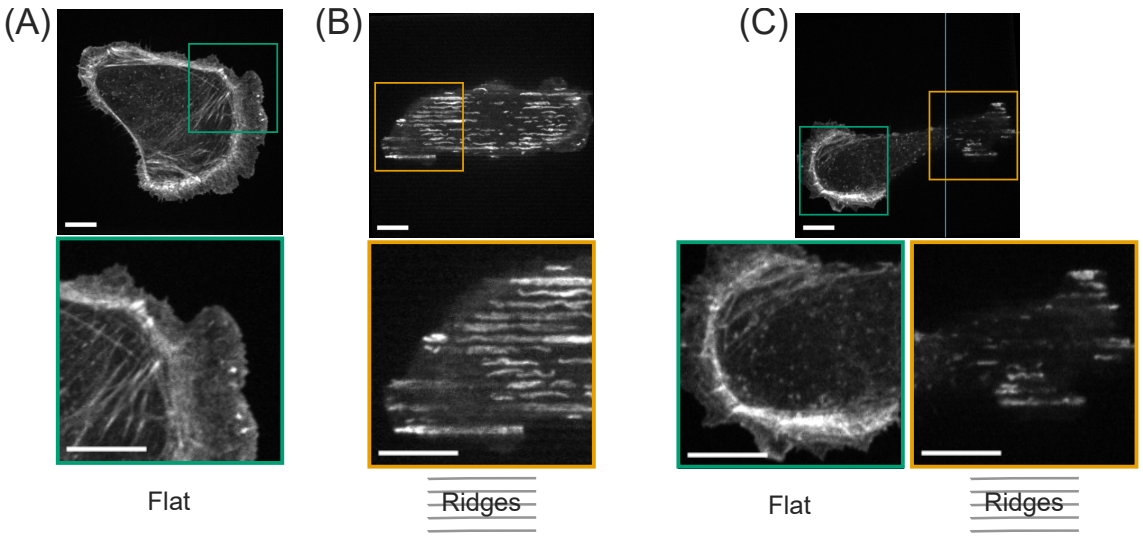

Figure 4.1: Nanotopography prompts distinct actin morphology. The actin cytoskeleton of an epithelial MCF10A cell on (A) a flat surface had an actin morphology that was distinct from that of a cell on (B) a nanoridged surface. (C) A cell that was partially on a nanoridged region and partially on a flat region exhibited local actin morphologies that were driven by the underlying topography. The blue line in (C) indicates the boundary between the flat region and the nanoridged region. All scale bars are 10 μm.

of Figure 4.2C, a representative kymograph of a region perpendicular to the ridges shows actin structures that persisted for tens of minutes and did not move perpendicular to the ridges. This behavior was typical for kymographs perpendicular to the ridges, although perpendicular motion was observed in some cases, as discussed below.

The behavior of motile, neutrophil-like HL60 cells on flat and nanoridged regions is illustrated in Figure 4.2D–F. Figure 4.2D indicates the regions from which kymographs were generated. In HL60 cells on flat regions, actin was concentrated near the cell front. This localization was largely preserved on the ridged surfaces, although the morphology of the actin changed such that streaks of actin were aligned with the ridges. On flat surfaces, the HL60 cells showed regions of protrusions and retractions (Figure 4.2E), similar to the actin dynamics seen in MCF10A cells (Figure 4.2B). We note that protrusions occured on a scale of seconds in HL60 cells and on a scale of minutes in MCF10A cells. Kymographs of the HL60 cells in the direction parallel to the nanoridges showed protrusive dynamics, although often in the form of single persistent waves (Figure 4.2F, top), in contrast to the oscillatory behavior seen on flat surfaces (Figure 4.2E). A representative kymograph of an HL60 cell in the direction perpendicular to the nanoridges shows streaks (Figure 4.2F, bottom) that indicate that actin waves did not move perpendicular to the ridges. However, the streaks were shorter in duration than those in a typical MCF10A cell (Figure 4.2C). This behavior was typical for kymographs of actin in HL60 perpendicular to the ridges. Unlike in MCF10A cells, in which actin streaks on the ridges localized throughout the cell (Figure 4.2C, bottom), in the HL60 cells the

streaks occured near the cell front (Figure 4.2F, bottom). Groups of actin streaks propagated together at the front of the HL60 cells, suggesting that there may have been a large-scale organization of actin dynamics (spanning many ridges) in these cells. It is unclear whether there was large-scale organization of actin dynamics in the MCF10A cells. The full range of actin dynamics was more complex than what was revealed by kymographs. MCF10A cells on the ridged regions exhibited actin dynamics throughout the substrate contact area, whereas actin dynamics on flat surfaces were largely confined to the cell boundary. In both cell types, nanoridges stimulated reproducible, dynamic, linear actin structures.

Time-lapse fluorescence images of actin waves are difficult to interpret by visual inspection or kymographs alone, because the observed dynamics arise from a complex spatio-temporal concentration field. To measure these wavelike dynamics quantitatively, we must first define a wave (size and shape) and then capture its propagation (e.g., splitting, recombination, and changes in direction). Here, we address these challenges by introducing an automated approach to quantify actin-wave dynamics across length scales for unbiased comparison in different cell types and extracellular environments.

Our method is based on a computer-vision algorithm from robotics and navigation control called optical flow [87, 89], which provides pixel-based information about the direction and magnitude of intensity flux in a series of time-lapse images. Fields of optical-flow vectors are calculated by integrating changes of intensity in space and time, as shown schematically in Figure 4.3. For example, two images of a migrating HL60 cell taken 8 sec apart are shown, with changes in time highlighted

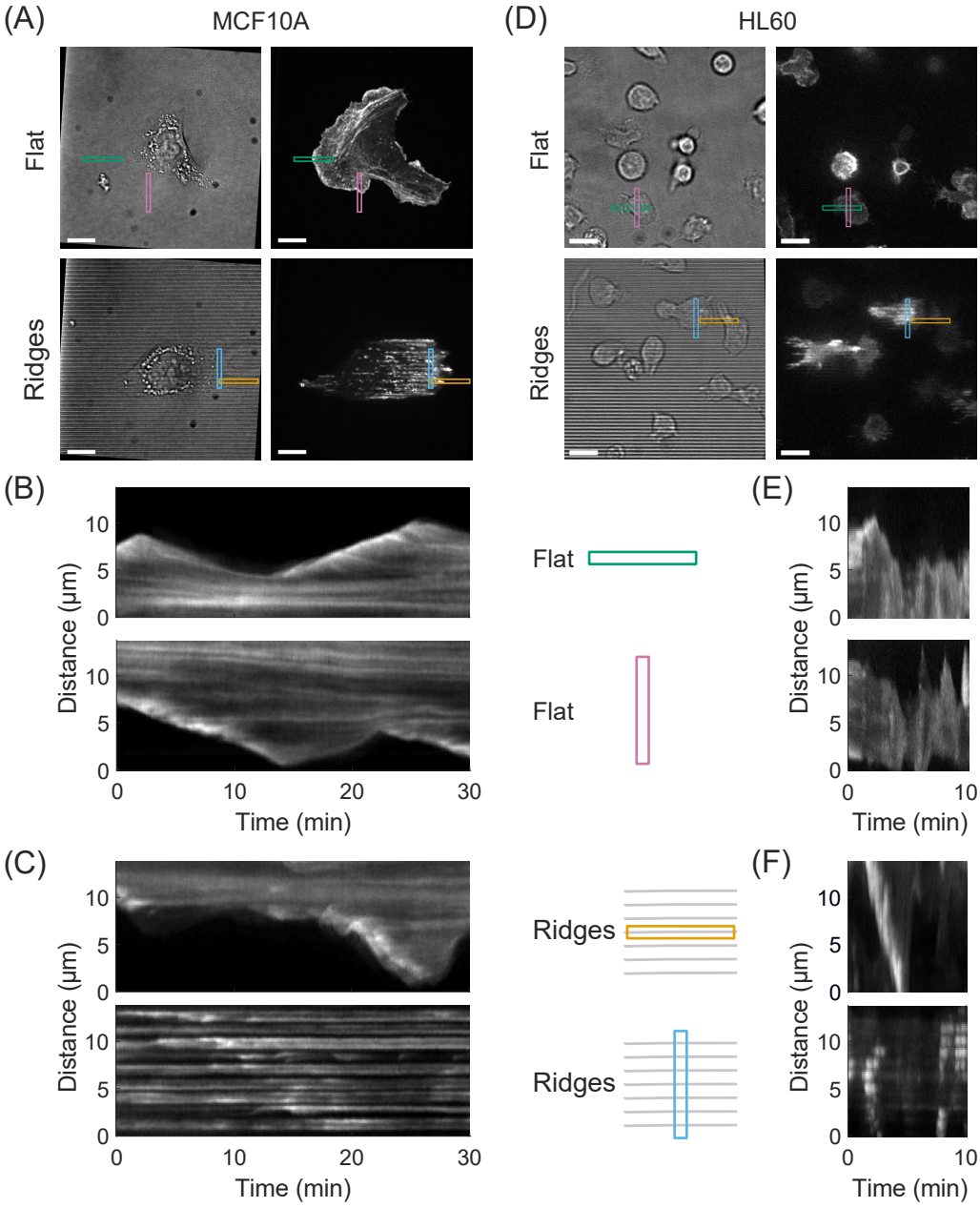

Figure 4.2: Nanotopography leads to distinct actin morphodynamics. (A) Optical micrographs of MCF10A cells in (left) bright-field and (right) fluorescence on (top) a flat region and (bottom) a nanoridged region. All scale bars are 10 μm. Kymographs for the areas denoted in A are shown in B for the flat region and in C for the nanoridges. D-F are the same as A-C, respectively, but for HL60 cells.

by a green-to-magenta montage (Figure 4.3A). The magenta region indicates growth of the actin front (which, as expected, occured at the leading edge of the cell), and the green region indicates a decrease in actin intensity.

The general objective of calculating optical flow is to solve for the unknowns Δx and Δy in Equation 2.2, where $I(x, y, t)$ represents the actin fluorescence intensity at frame t. The intensity I that exists at point (x, y) at time t translates to a new point $(x + \Delta x, y + \Delta y)$ at some future time $t + \Delta t$. Expanding about small Δx and Δy and neglecting second-order derivatives yields the master optical-flow expression in Equation 2.4. This governing equation is underdetermined, and so the Lucas-Kanade optical-flow constraint [89] was applied to calculate flow fields. This constraint prescribes that all pixels in a small window centered at (x, y) have the same translational optical-flow vector. The equation can then be solved using the least-squares criterion (an explicit derivation is given in the Materials and Methods) to yield the intensity flow, $\vec{v}$ (Figure 4.3B, center panel). Solving for $\vec{v}$ requires use of the negative spatial gradient, $-\vec{\nabla} I$ (Figure 4.3B, left panel), which forms a vector field oriented away from regions of highest local intensity, and the time derivative, $\frac{\partial I}{\partial t}$ (Figure 4.3B, right panel), as shown in Equation 2.2. Using the pair of images from Figure 4.3A as a representative example, the spatial and temporal gradients were used to calculate the optical-flow vector field, which approximated the flow of actin between the two frames. In this example, the vector field captured the translational motion on the leading edge of the cell (Figure 4.3C).

Optical-flow measurements of actin intensity translation enabled the quantification of the pixel-scale response of actin dynamics to nanoridge topographies

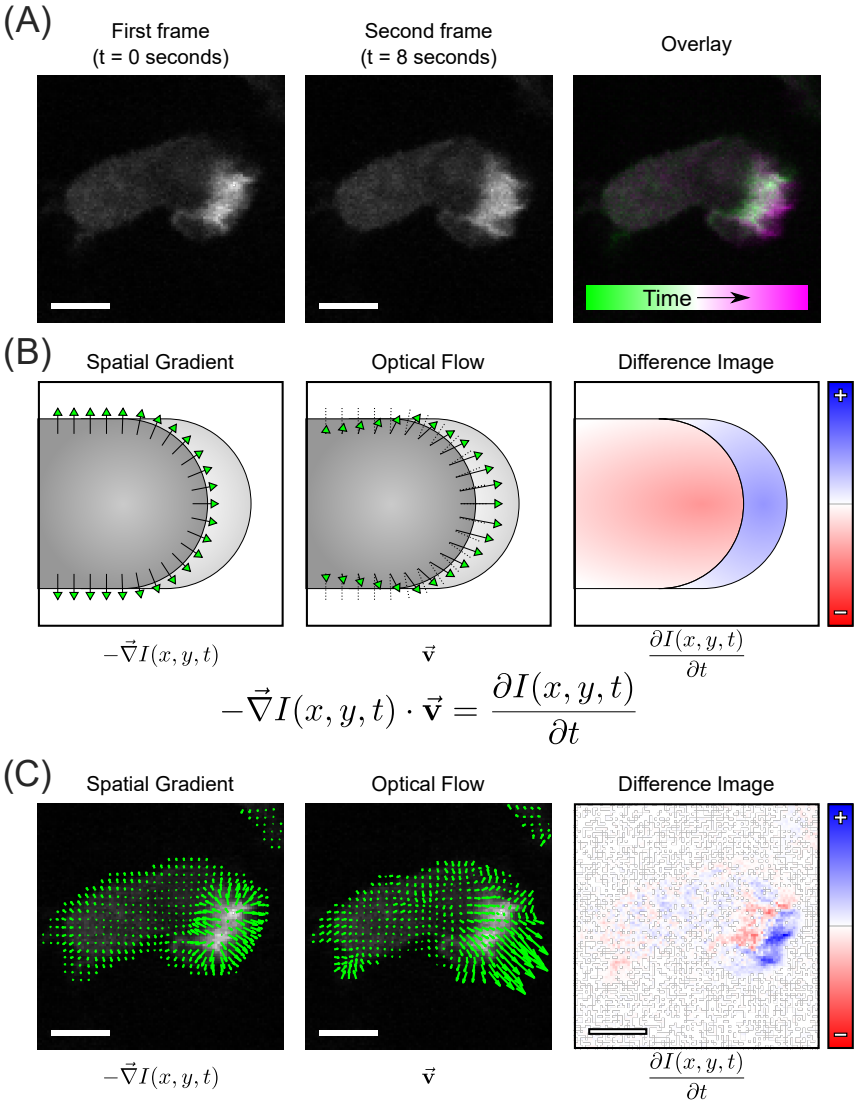

Figure 4.3: Optical flow captured the dynamics in movies of actin fluorescence. (A) Two frames of a representative HL60 cell obtained 8 sec apart and a merged image show the dynamics of cell behavior over time. (B) The procedure used to carry out optical-flow calculations combined the spatial gradient of an image (left) and the difference image/temporal gradient (right) to yield the optical-flow vector field (center). (C) Calculations from (B) were applied to the images in (A). The spatial gradient (left) and temporal gradient (right) resulted in the output optical-flow vector field (center). Blue pixels in the right panel of (C) indicate positive changes (increases) in the pixel brightness from the first frame to the second frame, and red pixels in the right panel indicate negative changes (decreases) in the pixel brightness from the first frame to the second frame. All scale bars are 5 μm.

(Figure 4.4). The green-to-magenta montages of representative HL60 and MCF10A cells show dynamic and protrusive actin behavior at the leading edge of the cell (Figure 4.4A). Coloring the calculated flow fields based on direction relative to the nanoridges (Figure 4.4B) reveals the clear bias of actin wave guidance in the direction parallel to the ridges, which is consistent with the qualitative features of the montage images in Figure 4.4A. Measurements of the optical-flow directions in all HL60 and MCF10A cells on both flat and ridged surface topographies are shown in the histograms of Figure 4.4C. In both cell types, the cumulative distribution of flow in cells on flat surfaces showed no appreciable bias in any direction. However, cells on ridges exhibited a clear preference for flow along the ridge direction.

We note that the images for the MCF10A and HL60 were obtained with different objectives (100× and 60×, respectively) and at different acquisition rates (10 and 2 sec between frames, respectively). Nevertheless, the optical-flow algorithm performed well on each set of data, emphasizing the broad applicability of this approach. The two cell types also used different actin-labeling approaches (LifeAct for the MCF10A and Actin-YFP for the HL60), which may have different overexpression effects on actin dynamics [130], but in both cases produced reliable optical-flow results that were indicative of nanotopography-guided actin dynamics.

For further quantification, we fit the distribution of flow directions from each cell to a bimodal von Mises model with a constant offset (Materials and Methods). The distribution consists of a uniform component and two peaked components that are 180° apart. The five parameters of the bimodal model are illustrated in Figure 4.4D. The angle θ_μ indicates the direction of the main component, and $\frac{1}{\kappa}$ is

proportional to the width of the distribution. The values of κ on ridged regions were significantly higher than those than on flat regions for both the MCF10A and the HL60 cells (Figure 4.4E, p = 0.0001583 and p = 0.0040), indicating that the ridges strongly guided the actin flows in a bidirectional manner. A comparison of κ and θ_μ shows that cells with a bidirectional actin flow (i.e., high κ values) were more likely to be guided along the ridge direction (Figure 4.4F).

Although the optical-flow vector field indicates preferred directions of actin flow, it does not directly yield propagation speeds of actin polymerization waves. The magnitude of an optical-flow vector incorporates both the shift of actin in space and the change in actin intensity over time. This submicron-scale (i.e., pixel-scale) flux of intensity does not translate directly into characteristics of the dynamics that are notable on the micron scale (i.e., tens of pixels), such as the organization of waves across ridges that were seen in neutrophils in Figure 4.2F or the speed of wave propagation. To quantify these micron-scale characteristics, we combined similarly oriented optical-flow vectors into clusters (Figure 4.5). To ensure that we tracked robust clusters, we applied additional constraints, such as requiring sufficiently large intensity changes (see Materials and Methods). The result of this clustering was the identification of broad regions of actin that moved collectively.

To quantify these micron-scale structures further, we applied peak-finding and tracking algorithms [131] to follow the locations of maximum alignment of these optical-flow clusters on the micron scale. Although the optical-flow results shown in Figure 4.4 followed motion on the pixel scale, by following the peak alignment of the optical flow, we were able to track larger coordinated clusters of actin. Our

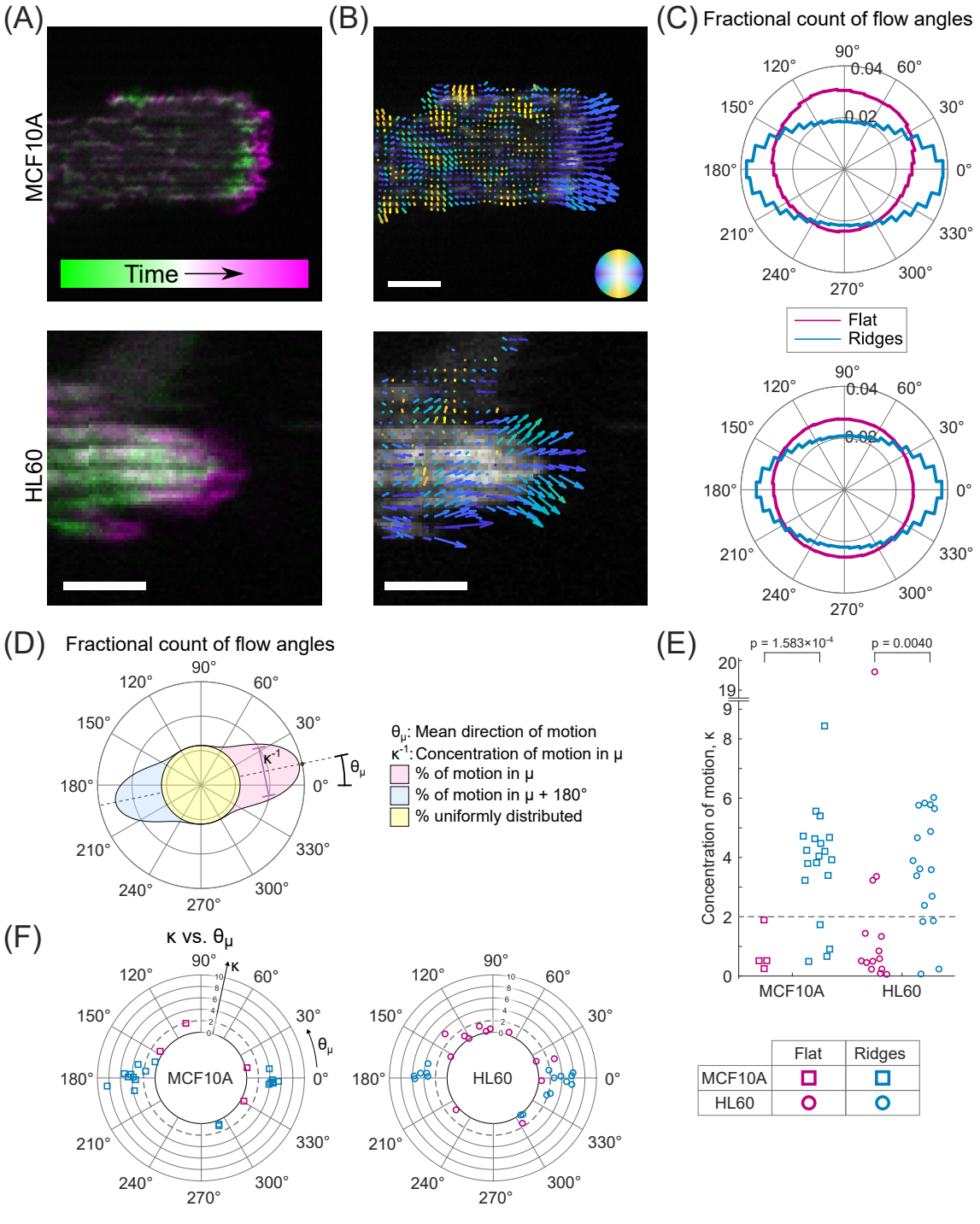
(A)
MCF10A
Time
HL60
(B)
(C) Fractional count of flow angles
90°
120°
60°
150°
30°
180°
0°
210°
330°
240°
300°
270°
0.04
0.02
Flat
Ridges
(D) Fractional count of flow angles
κ⁻¹
θμ
θμ: Mean direction of motion
κ⁻¹: Concentration of motion in μ
% of motion in μ
% of motion in μ + 180°
% uniformly distributed
(E)
p = 1.583×10⁻⁴
p = 0.0040
Concentration of motion, κ
MCF10A
HL60
Flat
Ridges
(F)
κ vs. θμ
κ
MCF10A
HL60

Figure 4.4: Using optical flow to measure pixel-scale actin dynamics. (A) Representative merged images of an MCF10A cell (top, 100 sec apart) and an HL60 cell (bottom, 8 sec apart). (B) Optical-flow vectors colored by direction relative to the horizontal ridges. All scale bars are 5 μm. (C) Cumulative distributions of the optical-flow vector directions for multiple HL60 and MCF10A cells on flat and ridged surfaces; all cells were weighted equally in the distribution. (D) The distribution of angles were fit to a mixture of two von Mises distributions with five fitting parameters: θ_μ (primary direction of motion), κ (inversely related to distribution width), and three coefficients indicating the strength of motion in the θ_μ and $\theta_\mu + 180^\circ$ directions and the strength of the uniform distribution. (E) In both MCF10A and HL60 cells, the distribution widths, parameterized by κ, were significantly different ($p = 0.0001583$ and $p = 0.0040$) on flat versus ridged surfaces. (F) θ_μ (angular axis) vs. κ (radial axis). Values of $\kappa < 2$ (indicated by the dashed line) were cells with direction distributions that are statistically indistinguishable from a uniform distribution. We note that $\kappa = 19.6$ for one HL60 cell, which is not visible in this figure.

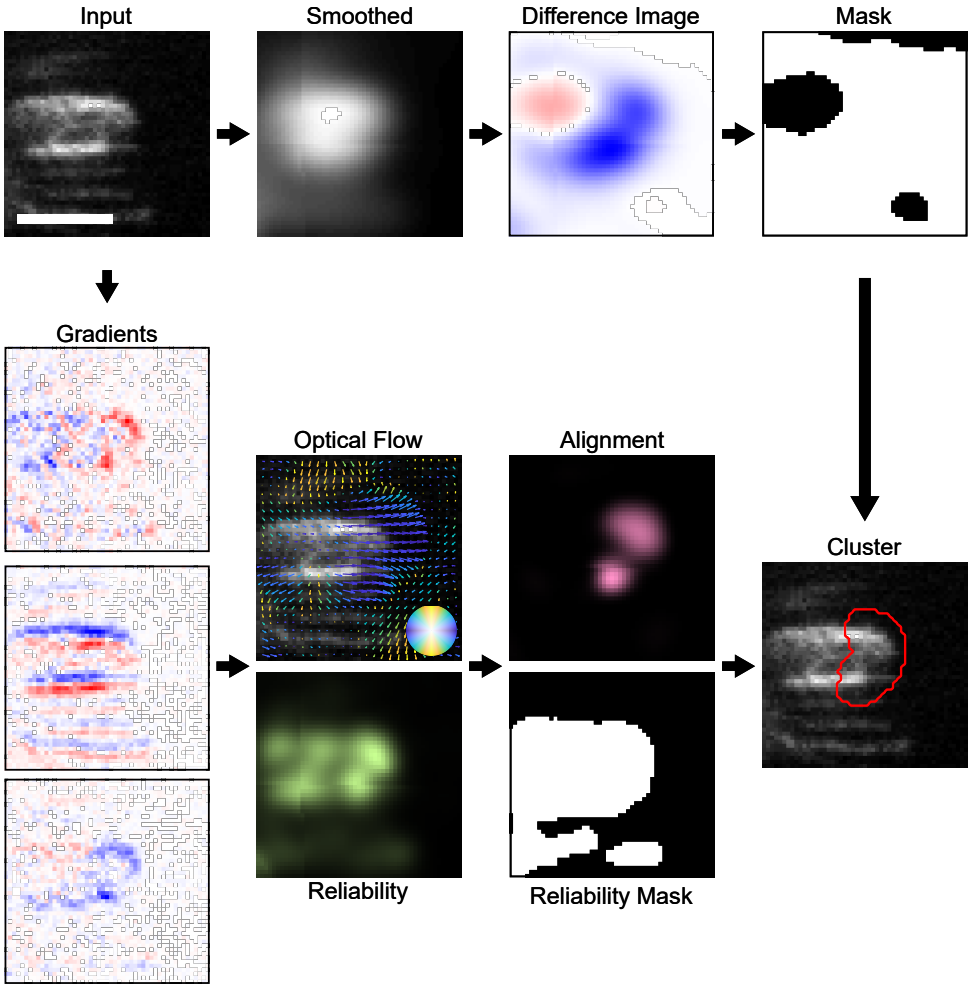

Figure 4.5: Finding clusters using optical flow. Input time-lapse images (upper left, scale bar is 5 μm.) were used to generate a series of masks along two independent work flows to generate three outputs: a difference-image mask, an alignment matrix, and a reliability mask. To generate the difference image mask, images were smoothed and subtracted from adjacent frames. The difference-image mask was calculated by applying a threshold (in this work, the threshold is 0). To generate the alignment and reliability masks, spatiotemporal intensity gradients were calculated and used to estimate optical flow and reliability. Alignment was calculated by taking the dot product between vectors and their local neighborhood (in this work, the neighborhood was a Gaussian with a standard deviation of 0.63 μm). The reliability mask was calculated by applying a threshold (in this work, the threshold was 10$\times$ the median of the reliability distribution). Taken together, the difference image mask, alignment matrix, and reliability mask were multiplied in an element-wise fashion to generate the final cluster image. In this work, the cluster image was used as an input to peak finding and tracking algorithms.

tracking is consistent with the actin dynamics seen in kymographs, as shown by the representative kymographs of MCF10A (Figure 4.6C) and HL60 (Figure 4.6D) cells overlaid with the tracked location of actin waves. Unlike kymographs, which were sensitive to motion along a chosen direction, tracks of clustered flow vectors revealed the micron-scale motion of actin in two dimensions. The benefits of our approach are illustrated in Figure 4.6C for an MCF10A cell. For the initial frames, the kymograph indicates a stationary actin structure (Figure 4.6C, left), but when the actin dynamics are viewed in two dimensions (Figure 4.6C, right), it is evident that in the early frames this wave is moving perpendicular to the ridges, a motion that cannot be captured in this one-dimensional kymograph. Thus, the combination of optical flow, clustering, and tracking allowed us to follow actin waves without being limited to tracking motion that only occured along a straight line.

The speeds of the tracked actin clusters (Figure 4.6E) were similar to speeds derived from actin kymographs (Figures 4.6C, 4.6D, and 4.7), despite an approximately order-of-magnitude difference in speed between the two cell types that is consistent with their distinct *in vivo* functions and with previously reported cell-migration speeds [79, 132]. For both cell types we found no significant difference ($p = 0.5529$ and $p = 0.0586$) between actin-wave speeds on flat and ridged surfaces (Figure 4.6E), implying that topography steered actin dynamics but did not alter wave speeds. On flat surfaces, the directions of the clusters were distributed uniformly for MCF10A cells, but showed distinct peaks in multiple directions for HL60 cells (Figure 4.6F). This observation is consistent with the polarized character of actin in several of the HL60 cells on flat surfaces, corresponding to κ values greater

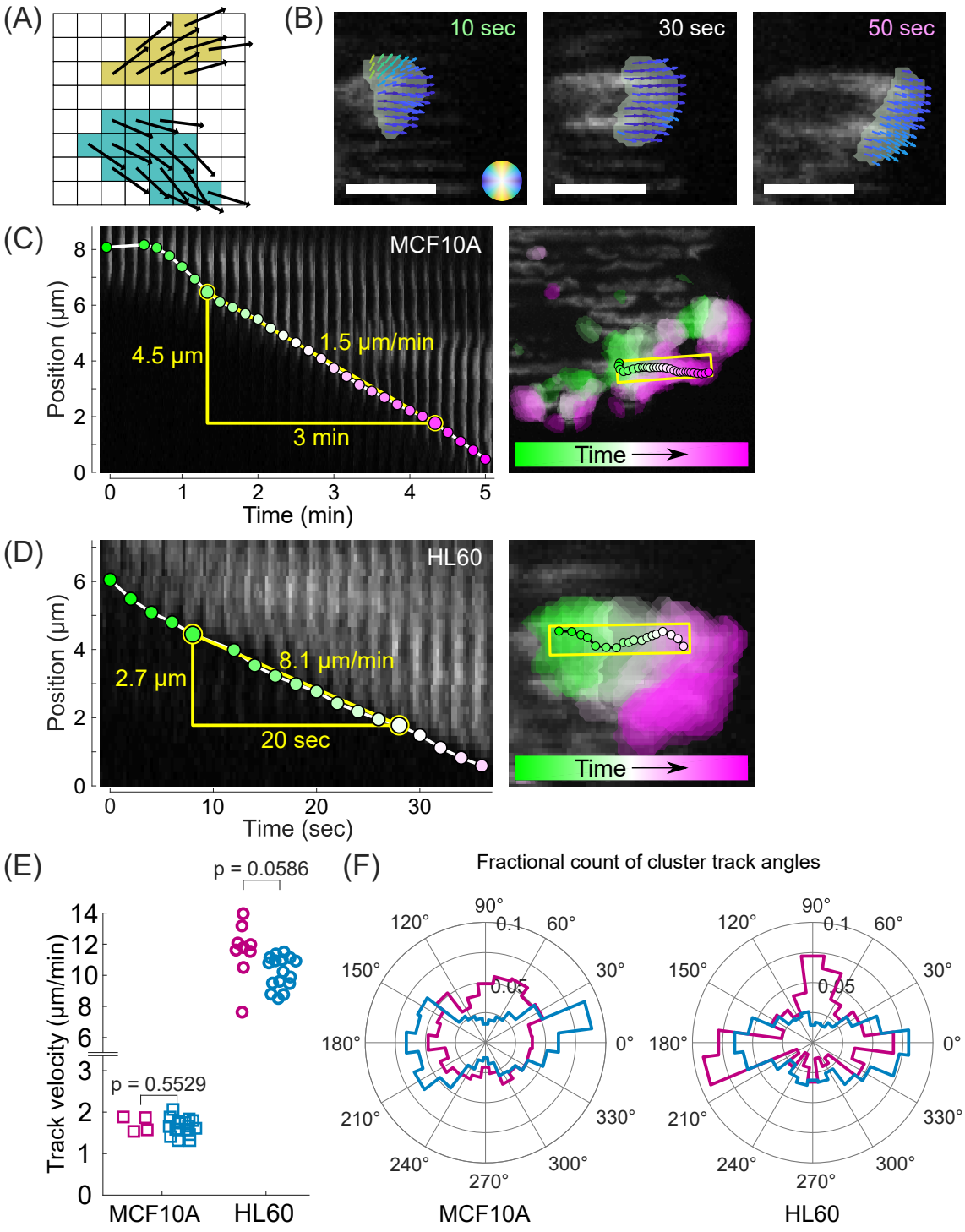
(A)
(B)
10 sec
30 sec
50 sec
(C)
MCF10A
Position (μm)
4.5 μm
1.5 μm/min
3 min
Time (min)
Time
(D)
HL60
Position (μm)
2.7 μm
8.1 μm/min
20 sec
Time (sec)
Time
(E)
p = 0.0586
p = 0.5529
Track velocity (μm/min)
MCF10A
HL60
(F)
Fractional count of cluster track angles
MCF10A
HL60

Figure 4.6: Clustering of optical-flow vectors to measure micron-scale dynamics. (A) Similar flow vectors were grouped into clusters. (B) Clusters contain optical-flow vectors with a wide array of orientations, resulting in micron-scale structures. All scale bars are 5 μm. (C, D) Particle-tracking algorithms were applied to the tracked clusters. The cluster tracks were consistent with the motion at the leading edge of the actin waves seen in the kymographs in both HL60 (C, left) and MCF10A (D, left). Panels to the right of each kymograph show the same track in the 2D context of the cells; clusters found throughout the cell over time are indicated by colored regions. (E) The cluster tracks were used to determine speed distributions of actin waves on the ridges in the MCF10A and HL60 cells, which showed no significant difference ($p = 0.5529$ and $p = 0.0586$) between flat surfaces and ridges. (F) Cumulative angle distributions of cluster track directions for multiple HL60 and MCF10A cells on flat and ridged surfaces; all cells were weighted equally in the distribution. ($N = 4$ MCF10A cells on flat surfaces from three independent experiments, $N = 17$ MCF10A cells on ridges from four independent experiments, $N = 9$ HL60 cells on flat surfaces from two independent experiments, and $N = 16$ HL60 cells on ridges from three independent experiments.)

than 2 in Figures 4.4E and 4.4F.

4.4 Discussion

Extracellular texture, which is an important component of the 3-D, *in vivo* environment, is capable of spatially patterning actin and modulating actin dynamics. Using nanoridge structures in conjunction with optical-flow analysis, we were able to probe and quantify this intracellular response to extracellular textures in a systematic manner.

Previous studies of *D. discoideum* [29,38], B cells [39], and tumor-associated fibroblasts [133] showed similarity in actin response to texture, which suggests that guidance of actin driven by texture (esotaxis) is broadly conserved across cell types. Controlled textures are thus a useful model microenvironment for the systematic, reproducible, and quantitative study of intracellular dynamics and force regulation. Here we demonstrated the analysis of time-lapse images of two cell types that have distinct physiological function. Neutrophil-like HL60 cells are polarized and highly motile, and respond to a variety of cues as they fulfill their role in the immune system, whereas epithelial MCF10A cells have a nonmotile physiological function. Nevertheless, both cell types showed clear, and quantitatively similar, actin dynamics in response to surface textures. Consistent with our and other prior results [29,133], we find that nanoridges lead to persistent streaks of actin that are not seen on flat surfaces.

Optical flow enables the quantification of both the reproducible streaks of actin

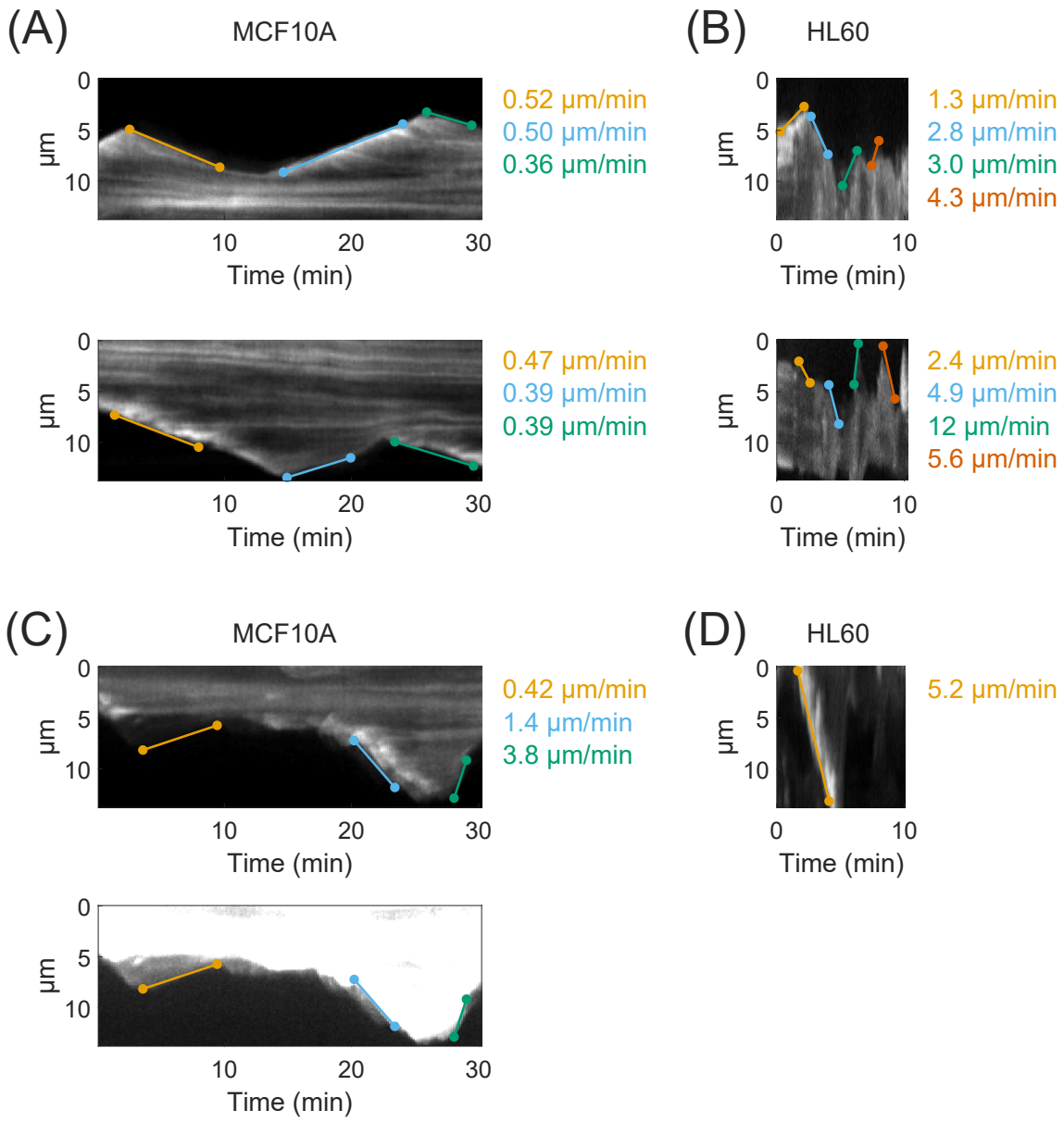

Figure 4.7: Actin-wave speeds measured by kymographs to validate optical-flow clustering. Actin-wave speeds were calculated from the kymographs shown in Figure 4.2 by manually selecting two points on the kymograph and calculating the slope between the points. The speeds shown here agreed with the distribution of speeds found using optical-flow-based tracking (Figure 4.6) for a MCF10A on a flat surface (A), an HL60 cell on a flat surface (B), a MCF10A cell on a ridged surface (C), and an HL60 cell on a ridged surface (D). The bottom panel of (C) shows a saturated version of the underlying kymograph to emphasize protrusions.

seen on nanoridged surfaces and the more chaotic actin waves seen on flat surfaces. The latter waves are typically much wider than guided actin waves. On flat surfaces the waves often change direction, and can also grow wider and split. Such motion phenotypes are not easily captured with standard techniques such as kymographs. Optical flow enables us to follow these dynamics, and thus yields insights beyond those derived from kymograph-based techniques.

We note that optical flow is suitable for comparisons of systems imaged under different conditions (e.g., 60× vs. 100× objectives), enabling comparisons of cells with widely varying sizes and migration speeds. The use of varying acquisition rates (i.e., 2 and 10 sec) in this work was based on the differences in cell migration speeds of the two cell lines studied. In general, optical flow requires a frame rate such that changes in fluorescence intensity between frames are small, but larger than noise. Our use of the Lucas-Kanade optical-flow constraint also requires that there is a smoothness to the flow field over a certain neighborhood, which is a length-scale parameter in the optical-flow analysis. This assumption is met by a wide variety of biological imaging data sets, and thus the use of our optical-flow approach is not limited to actin dynamics. Optical flow could provide insights into the motion of other cytoskeletal proteins, such as tubulin, or into the dynamics of other fluorescent markers that exhibit a spatially and temporally changing intensity field. Our use of clustering to study larger-scale actin dynamics could similarly be adapted to other fluorescent markers under the assumption that there are larger-scale dynamics that move together in similar directions. In this work, we used a spinning-disk confocal microscope for image acquisition, but our analysis pipeline

would also be appropriate for other imaging techniques, such as epifluorescence. When working with other imaging techniques or fluorescent markers, the size of the Lucas-Kanade neighborhood and the threshold for vector reproducibility (see Materials and Methods and Figure 4.5) can be adapted to only include robust results in further analysis.

Using submicron-scale optical flow and associated micron-scale analysis, we showed that both MCF10A and HL60 cells had actin flows that were biased along nanoridges. By clustering similarly oriented optical-flow vectors, we were able to measure the speed of actin waves within the cells. The measured speeds were comparable to speeds calculated from actin kymographs. Optical-flow analysis allowed us to determine that the speeds did not differ significantly on flat versus ridged regions. This finding indicates that nanotopography guides, but does not fundamentally alter the speed of, actin dynamics. We measured actin-wave speeds on the order of 1 μm/min in the MCF10A cells, consistent with previously reported cell migration speeds of approximately 0.5 μm/min [79]. In the HL60 cells we found actin speeds ranging from approximately 8 to 14 μm/min, consistent with the 8 μm/min speed for cell migration previously reported [132].

Fitting the optical-flow vectors to a bimodal von Mises distribution enabled quantification of the differences in the directionality of actin flows on flat and ridged surfaces in both cell lines. The fit parameters also showed differences in actin polarization in these two cell lines. HL60 cells occasionally exhibited coordinated and directed actin flows even on flat surfaces, whereas MCF10A cells on flat surfaces showed uniform direction distributions of actin waves. On the micron scale, actin-

wave tracks from individual HL60 cells on flat surfaces generally polarized and had a preferred direction, consistent with the behavior of immune cells, which tend to polarize and migrate in a directed manner. Tracks from MCF10A cells on a flat surface, on the other hand, were more directionally uniform for each cell. In both cell types, ridges guided actin waves in a bidirectional manner.

The quantitative actin responses in MCF10A and HL60 cells support a model in which surface texture provides a symmetry-breaking cue that leads to nucleation of actin polymerization. Under flat tissue-culture conditions, which lack symmetry-breaking cues, actin polymerization relies on spontaneous nucleation or edge effects [134]. Edge effects may lead to morphological features such as the lamellipodia seen in HL60 cells on flat surfaces in Figure 4.2B. By changing the landscape on which nucleation occurs, surface texture can lead to actin polymerization in other locations of the cell, such as the persistent streaks seen in the center of MCF10A cells on ridges in Figure 4.2A.

There are multiple mechanisms by which cells may respond to local forces and geometry [135], including sensing mechanisms that can respond to membrane curvature on a variety of scales [136]. Our finding that nanoridges changed the direction, rather than the speed, of actin waves suggests that growth of existing actin filaments away from the surface is the rate-limiting step of actin polymerization wave propagation. In some cases, sensing mechanisms may rely on the preferential formation of focal adhesions. This hypothesis is consistent with previous results on focal adhesion localization and orientation in response to surface texture [126, 127]. Although MCF10A cells form strong focal adhesions that may align with texture

cues [127], the HL60 cells form weaker adhesions, and the previously studied *D. discoideum* cells [29, 38] are known to not form integrin-mediated focal adhesions. Thus, the dominant mechanism of surface texture response likely depends on both the cell type and the extracellular environment.

Known surface-sensing mechanisms also include cytoskeletal components such as septins, which respond to micron-scale curvatures [137], and BAR domains, which sense nanoscale curvature [138]. Proteins with BAR domains have been linked to actin assembly [139], as well as to key components of actin-regulating pathways, such as WAVE and Rac [140,141]. Recent work has suggested that nucleation of new actin filaments is enhanced by nanotopography. Specifically, curved nanopillars activate the nucleation-promoting factors Arp2/3 and N-WASP through enhanced binding of an F-BAR domain containing protein [16]. Additionally, evidence suggests that topography is capable of shifting multiple gene-expression pathways [142], which implies that longer-term exposure to topography may mediate additional surface-sensing pathways. As *in vivo* microenvironments contain a variety of textures, it is likely that multiple mechanisms respond to distinct features of extracellular texture, and future work on the response of actin regulators to controlled topographies such as those investigated here will help elucidate the contributions of distinct signaling pathways in topography-guided actin dynamics.

Although the systematic modulation and interrogation of all possible molecular factors of esotaxis is beyond the scope of this chapter, our analysis yields two remarkable constraints on the molecular sources of esotaxis. First, the speed of actin waves is not altered by esotaxis. Second, the directional guidance provided

by nanotopography is comparable in the two cell types investigated, despite their disparate functions and migratory phenotypes. Quantitative analysis of esotaxis as a physical phenotype could yield crucial prognostic disease insights, especially in the case of cancer, in which changes in the texture of the microenvironment correlate with disease progression.

4.5 Materials and Methods

4.5.1 Cell culture and imaging

HL60 YFP-actin cells were a gift from Orion Weiner of the University of California, San Francisco. The cells were cultured in RPMI 1640 medium, Glutamax (Life Technologies) supplemented with 10% heat-inactivated fetal bovine serum (Gemini Bio). Cells were passaged every 2-3 days and kept between 3×10^5 and 1×10^6 cells/mL. For differentiation, cell media was additionally supplemented with 1.3% dimethyl sulfoxide Hybri-Max (Sigma Aldrich) for 5 days before imaging. Actin dynamics of HL-60 YFPactin cells were observed by confocal fluorescence and brightfield time-lapse imaging using a PerkinElmer spinning-disk confocal microscope with a water immersion 60× objective (0.21 μm/pixel). Images were recorded every 2 sec. We note that this method of plating resulted in the imaging of some multicellular clusters of HL60 cells; these clusters were not considered for further analysis.

Preparation for imaging included a 10 μg/mL coating of fibronectin on the substrates. Cells were plated and allowed to settle. After approximately 30 min,

N-Formyl-Met-Leu-Phe (fMLF; Sigma Aldrich) was added to 1 μm. HL-60 cells were imaged on flat resin and ridged nanotopographies beginning between 10 and 15 sec after fMLF stimulation. All images analyzed in this work were obtained after fMLF stimulation.

MCF10A LifeAct-EGFP cells were a gift from Carole A. Parent. These cells were cultured in DMEM/F12 media supplemented with 5% horse serum, 10 μg/mL insulin (ThermoFisher Scientific), 10 ng/mL EGF (Peprotech, Rocky Hill, NJ), 0.5 μg/mL hydrocortisone, and 100 ng/mL cholera toxin (both Sigma, St. Louis, MO). The media were additionally supplemented with 2 μg/ml puromycin dihydrochloride (ThermoFisher Scientific) to select for EGFP-positive cells. Before imaging, cells were plated on a nanoridged surface coated with collagen IV and were allowed to adhere to the surface overnight. Actin dynamics were studied by confocal fluorescence and bright-field, time-lapse imaging using a PerkinElmer spinning-disk confocal microscope with a 100$\times$ objective (0.14 μm/pixel). Images were recorded every 10 sec. For both cell types, data were collected using PerkinElmers Volocity software (version 6.4.0). The spinning-disk confocal microscope was equipped with a Hamamatsu ImagEM X2 EM-CCD camera (C9100-23B) which recorded 12-bit images. Cells used in this study tested mycoplasma negative using the MycoAlert (Lonza) testing system.

4.5.2 Surface fabrication

The nanotopographies were designed and fabricated using multiphoton absorption polymerization (MAP), as described previously [127]. A drop of prepolymer resin (1:1 wt/wt Tris [2-hydroxy ethyl] isocyanurate triacrylate [SR368]: ethoxylated (6) trimethylolpropane triacrylate [SR499], both from Sartomer; 3% Lucirin TPO-L [BASF]) was sandwiched between a coverslip and a plasma-treated microscope slide that had been functionalized with acrylate groups [127, 143, 144]. The coverslip was mounted onto the stage of an inverted microscope (Zeiss Axiovert 135). A beam of 150-fs pulses centered at 800 nm from a Ti:sapphire oscillator (Coherent Mira 900) was directed into the microscope and through a highnumerical aperture objective (Zeiss alpha-Plan Fluar 100; NA 1.45). The stage motion and shutter were controlled using a program written in LabVIEW (National Instruments). Once the pattern was fabricated, the sample was developed in ethanol and baked at 110°C for 1 h.

A replica-molding approach was then used to mold the chemically functionalized pattern [127]. This step included the initial casting of a hard-poly dimethylsiloxane (h-PDMS) layer (1000 rpm, 40 sec) for better resolution of nanoscale features of the topographical pattern. This layer was allowed to sit on the pattern at room temperature for 2 hrs and was then baked at 60°C for an additional 1 hr. Finally, Sylgard 184 was mixed (10:1 elastomer base:curing agent) and poured onto the initial h-PDMS layer. The PDMS was cured at 60degC for 1 hr 10 min.

The MAP-fabricated structure was then reproduced through a soft litho-

graphic technique. A drop of the aforementioned resin was sandwiched between the PDMS mold and an acrylate functionalized coverslip and was then exposed to UV radiation from a lamp for a desired amount of time. After the resin cured, the coverslip was peeled off the mold. This process was repeated many times to produce enough replicas to perform the necessary experiments. The replicas were soaked in ethanol for at least 4 h and subsequently baked/dried in an oven at 110°C for 1 hour. Samples used to study MCF10A cells were also soaked in UltraPure water (ThermoFisher) for approximately 12 hours.

4.5.3 Kymographs

Kymographs were created in MATLAB by manually selecting a rectangular region in an actin image. Fluorescence intensities inside the region were averaged across the short axis of the region; this process was repeated for each image in the time-lapse sequence, and the resulting intensity data were combined into the kymographs shown in Figures 4.2 and 4.7.

4.5.4 Optical flow

The Lucas-Kanade optical-flow method [89] was used to capture the direction and strength of intensity flow of fluorescent actin and to produce vector fields indicating actin motion. The optical-flow vector field of an image series is the field of apparent translation in the image plane, as is shown schematically in Figure 4.3. Calculating the optical flow for two adjacent two-dimensional images in

an image series requires solving for the unknowns Δx and Δy in Equation 2.2, which yields the optical-flow vectors $\vec{v}$ in Equation 2.4. The Lucas-Kanade method uses a least-squares regression approach to solve for the best optical-flow vector on a pixel-by-pixel basis under the assumption that all pixels within a neighborhood move in a similar direction [89]. If solving for the optical-flow vector of some point p with coordinate (x_p, y_p, τ), the master optical flow equation requires that the optical flow vector of point p and all points in the neighborhood about p (points $1, 2, \ldots, p, \ldots, N$) follow the underdetermined relation given in Equation 2.4.

Under the Lucas-Kanade assumption, the vector for point p is assigned to all points in the neighborhood given in Equation 2.6. The least-squares solution to equations of the form in Equation 2.6, namely $A\vec{x} = \vec{b}$, are generally $\vec{x} = (A^T A)^{-1} A^T \vec{b}$ when $A^T A$ is invertible (i.e., when $(A^T A)^{-1}$ is nonsingular). Furthermore, we implement a scheme using a Gaussian weight matrix centered at point p to ensure that pixels near p have more influence over the result. The general equation then takes the form $\sqrt{w}A\vec{x} = \sqrt{w}\vec{b}$ and has the solution $\vec{x} = (A^T\sqrt{w}^T\sqrt{w}A)^{-1}A^T\sqrt{w}^T\sqrt{w}\vec{b} = (A^T wA)^{-1}A^T w\vec{b}$.

Optical-flow reliability is defined as the smallest eigenvalue of the $A^T wA$ matrix [145, 146], and was used to remove flow vectors that were created by noise or an ill-defined least-squares calculation. The threshold used can be adapted to best suit the experimental data and scientific questions of interest by only keeping the most reliable vectors while measuring the motion of more regions of the cell. The optical-flow weight matrix for MCF10A cells was a 27 $\times$ 27 pixel Gaussian with a σ of 4.5 pixels (0.63 μm). The optical-flow weight matrix for HL60 cells was 19 $\times$

19 pixel Gaussian with a σ of 3 pixels (0.63 μm). With other imaging modalities, magnifications, or fluorescent markers, it may be appropriate to change the size of this weight matrix based on the size of features of interest and noise in the image.

4.5.5 von Mises model of flow distribution

Optical-flow distributions were modeled with a modified bimodal von Mises distribution (von Mises distributions are a continuous and differentiable analogue of normal distributions on a circle with similar statistical properties). The model was defined as

$$f(\theta|\theta_\mu,\kappa) = p_1 VM(\theta|\theta_\mu,\kappa) + p_2 VM(\theta+\pi|\theta_\mu,\kappa) + (1-p_1-p_2)\frac{1}{2\pi} \tag{4.1}$$

where $VM(\theta|\theta_\mu,\kappa)$ is the von Mises distribution

$$VM(\theta|\theta_\mu,\kappa) = \frac{e^{\kappa\cos(\theta-\theta_\mu)}}{2\pi I_0(\kappa)} \tag{4.2}$$

and $I_0(\kappa)$ is the modified Bessel function of the first kind. The maximum likelihood estimates of the parameter κ were used for statistical analyses.

4.5.6 Cluster-tracking analysis

Regions of actin fluorescence were clustered using the direction of optical-flow vectors together with an optical-flow reliability threshold and by requiring that actin intensity change over time (see Figure 4.5 for a visualization of this workflow). The dot products between optical-flow vectors around a point p (i.e., vectors $\vec{v}_1, \vec{v}_2, \ldots, \vec{v}_{p-1}, \vec{v}_{p+1}, \ldots, \vec{v}_N$) were calculated and accumulated using a Gaussian weighting scheme to a single scalar alignment metric. The alignment metric was defined as

$$a_p = \sum_{i=1}^{N} w_i(\vec{v}_p \cdot \vec{v}_i) \tag{4.3}$$

where w is a renormalized $N \times N$ centered Gaussian matrix with a center manually set to 0. This calculation was carried out for each pixel. To require that the actin intensity change over time, a mask of the thresholded difference image between subsequent frames was calculated. For every pair of adjacent frames, I_t and $I_{t+\Delta t}$, the resulting mask took value 1 where $I_{t+\Delta t} > I_t$ and 0 otherwise. For our analysis, Δt = 30 sec for MCF10A and 6 sec for HL60. To calculate the final clustered regions, the alignment metric a_p, optical-flow reliability λ_p, and difference-image mask were multiplied in an element-wise manner to create a final cluster image. The cluster image was inputted into a peak-finding algorithm to locate peaks in the resulting intensity profile, and the Crocker-Grier particle-tracking algorithm [131] was used

to track coordinates of the resulting peaks over time.

The clustering weight matrix for MCF10A was a 27 × 27 pixel Gaussian with a SD of 4.5 pixels (0.63 μm). The clustering weight matrix for HL60 cells was 19 × 19 pixel Gaussian with a SD of 3 pixels (0.63 μm). The diameter of the peaks used during peak finding was 15 pixels (2.1 μm) for MCF10A cells and 10 pixels (2.1 μm) for HL60 cells. The maximum displacement used during tracking was 11.5 pixels (1.54 μm) for MCF10A cells and 7 pixels (1.47 μm) for HL60 cells. Tracks measured in the movies of MCF10A cells were considered only if they were tracked for more than three frames (30 sec) and tracks measured in movies of HL60 cells were only considered if they were tracked for more than three frames (6 sec).

4.5.7 Statistical methods

Measurements of for MCF10A cells (Figure 4.4) and actin-wave speeds for both cell types (Figure 4.6) were compared on flat versus nanoridged surfaces using two-sample t-tests with unequal variances. A two-tailed t-distribution was used to calculate the reported p-values. As the measurements κ of for HL60 cells violated the normality assumption for a t-test, we used a nonparametric Wilcoxon rank-sum test to compare these values.

Chapter 5: Systematic Analysis and Simulations of Topography-Induced Guidance of Actin Waves

This chapter was adapted from a work in preparation by Campanello*, Guven*, Driscoll, Sun, Carlsson, Fourkas, and Losert. Can Guven and Xiaoyu Sun performed the experiments, Can Guven and Anders Carlsson performed the simulations, Leonard Campanello designed and performed the optical-flow analysis, and Leonard Campanello and Can Guven wrote the paper.

5.1 Overview

The cytoskeleton of a living cell is one of the most versatile examples of active matter in nature. Through polymerization and depolymerization, the continuous remodeling of the cytoskeleton drives a multitude of biological processes, such as cell division, migration, and the development of multicellular organisms. Although a broad range of models aim to capture detailed biomechanical properties of the cytoskeleton, and especially the actin component, the experimental data and computational techniques required to perform detailed quantitative benchmarking are often lacking. Here, we directly link experimental observations of cytoskeletal remodeling

in *Dictyostelium discoideum* to simulations that include biophysically realistic dynamics of actin filaments. Using an optical-flow-based analysis, we perform detailed measurements on simulated and experimentally observed actin dynamics. To provide cells with biologically realistic extracellular environments, we employ uniformly spaced nanotopographic ridges similar in size to collagen fibers. In both experiments and simulations, the nanoridges generate guided waves of actin polymerization with reproducible direction, speed, and shape, allowing for deep, quantitative comparisons. Analysis of the simulations reveals that a model assuming redistribution of a fixed pool of nucleation promoting factors provides better agreement with experiments than does a model that posits local enhancement of nucleation. By varying the spacing between the ridged nanotopographic features, we demonstrate that maximum guidance by ridges occurs on spacings that are $\sim$1 to 2 microns apart and diminishes guidance for ridges greater than 3 microns apart. Neither the ridge spacing nor the concentration of available actin monomers alters the speed of actin waves, but these parameters do alter the length of actin filaments. Together, experiments and simulations of topography-induced guidance of actin waves provide a robust framework for understanding the mechanisms of texture sensing in the natural world.

5.2 Background

Cytoskeletal rearrangements underlie many critical cell behaviors. Through controlled polymerization and depolymerization, coordinated force generation of the

cytoskeleton results in polarization and migration [3], immune-cell activation [27,40], and crucial physiological functions such as tissue development, immune response, and wound healing [147–149].

Topographic features in the extracellular environment influence cytoskeletal dynamics and cell behavior. Collagen-fiber environments in the extracellular matrix (ECM), which are topographically complex [150], play an important role in functions such as differentiation [23], immune response [2], and cancer progression (Chapter 6). *In vitro* topographical features that are similar in size to typical ECM structures can also modulate morphology [28, 151] and migration [29]. Furthermore, ridge patterns with broken symmetry along the ridge axis, e.g., sawteeth, induce cell-type-dependent unidirectional guidance in epithelial cells [24], amoeboid *Dictyostelium discoideum* cells (which feature pseudopod-driven migration), and neutrophil-like HL60 cells (which feature lamellipod-driven migration) [38]. Despite the influence of physical topography on cytoskeletal dynamics and cell behaviors, the coupling between extracellular features and cytoskeletal signaling is poorly understood.

The primary cytoskeletal component responsible for remodeling and force generation is actin. In concert with other signaling proteins, such as PIP3 and PI3K, the actin cytoskeleton operates as an excitable system that can rapidly switch among a variety of dynamic states [9, 152, 153], such as propagating waves and oscillatory bursts [9,71]. Through continuous polymerization at the leading edge and depolymerization at the trailing edge, excitable actin rearrangements are manifested in wave-like propagations that push on the cell membrane and other cytoskeletal structures to generate forces [154, 155].

Actin excitability enables cells to respond to extracellular stimuli [9,152], and has been implicated in the development of subcellular protrusions [156,157] and in whole-cell behavior such as chemotaxis and electrotaxis [158–160]. However, the mechanisms by which actin excitability on nanotopography can guide subcellular and whole-cell behaviors are not well understood. For example, we have previously shown that actin flux and cell migration on nanotopographic sawteeth can change directions based on sawtooth pitch [38] and cell type [24,38]. Although the activity of actin nucleation-promoting factors (NPFs) contribute to topography sensing [15, 16], the connection between subcellular dynamics and whole-cell behavior is poorly understood.

In Chapter 4, I introduced an optical-flow-based approach to quantify actin flux. Using this method, we were able to identify quantitative similaritities of actin wave guidance by nanotopography between neutrophil-like cells (HL60) and epithelial cells (MCF10A), despite wave speeds and imaging conditions varying significantly between cell types. In this chapter, I employ this optical-flow analysis for a quantitative comparison of actin waves from experiments of *D. discoideum* to those in a dendritic-growth model of filament assembly and disassembly with realistic biochemical rates, NPFs, and filament-severing dynamics [41].

5.3 Results

5.3.1 Optical-flow analysis of actin waves revealed that ridges preferentially nucleate and guide actin dynamics.

Using limE-Δcoil-GFP *D. discoideum*, which overexpress the fluorescently-labeled actin-binding reconstruct limE-Δcoil [161, 162], we investigated the relationship between actin polymerization and nanotopography via time-lapse imaging on surfaces with evenly spaced, parallel ridges of different spacings (Figure 5.1). The characteristic length scale of actin polymerization waves in *D. discoideum* is between 1 and 2 μm [29, 154]. Thus, we investigated actin-wave dynamics on ridges with spacings ranging from 0.8 μm to 5 μm (Figure 5.1A–B). Dark regions in the bright-field images are ridges with a fixed width (200–300 nm) and height (0.4–1 μm), and the bright regions are the grooves between adjacent ridges. Cells were incubated with 2 mM caffeine to block the intracellular activation of cAMP synthesis and thus prohibit intercellular signal relay [163].

Topography-induced guidance of actin waves has been shown to bias the flow of new actin polymerization (Chapter 4). Similarly, in both representative time-lapse images from Figure 5.1A–B, the direction of actin polymerization appears to be biased in the ridge direction, i.e., from blue to yellow, and the nucleation of new actin polymerization appears to be enhanced at the ridges. Furthermore, as shown in Figure 5.1A, we observed continuous nucleation of actin waves on narrowly spaced ridges. On the other hand, as the spacing between ridges increased, as in

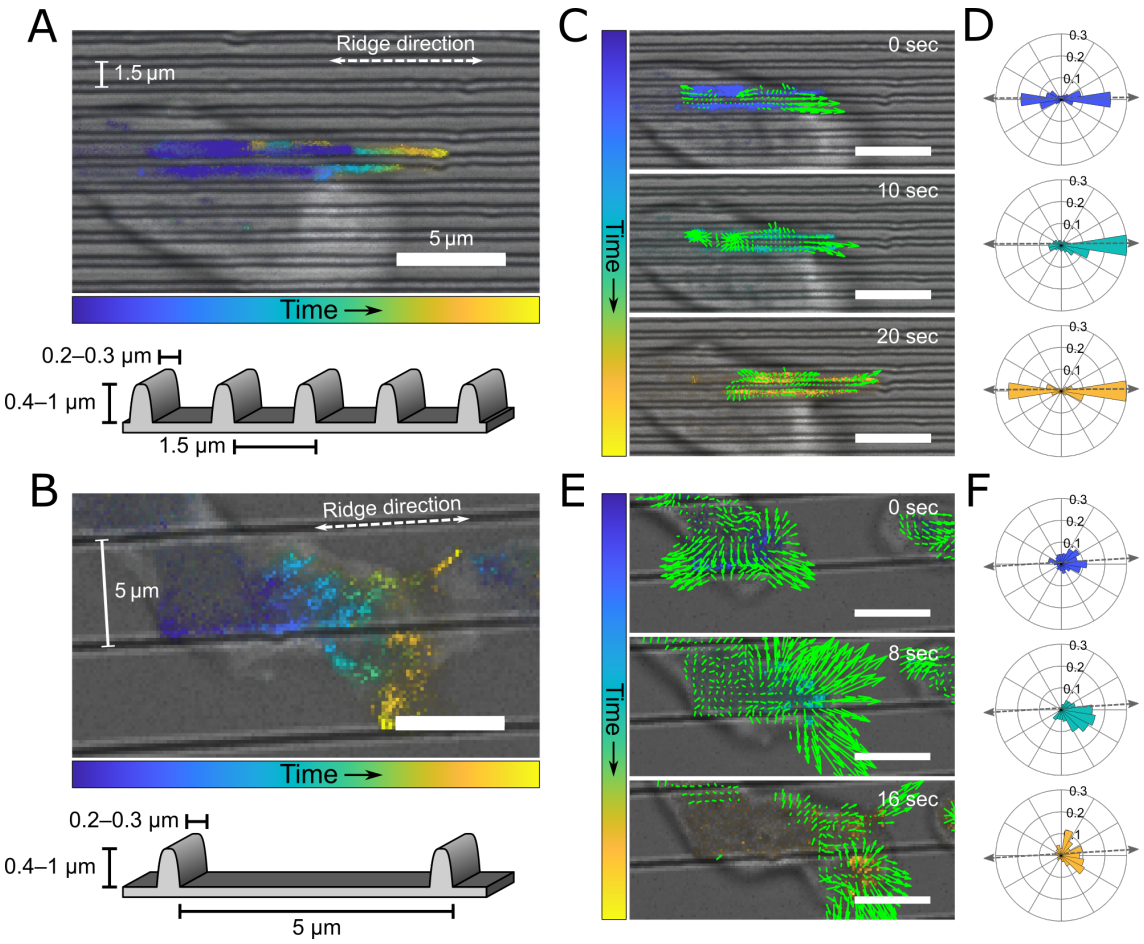

Figure 5.1: Actin-wave nucleation is enhanced at ridges and actin-wave dynamics are more complex with increased ridge spacing. Time-lapse montage of *D. discoideum* with fluorescently labeled actin-binding protein limE-Δcoil on (A) 1.5-μm-spaced ridges and (B) 5 μm spaced ridges. The polymerization of new actin waves is enhanced near ridges. (C) Three snapshots 10 sec apart on 1.5-μm-spaced ridges with optical-flow vector fields superimposed on images; the actin polymerization dynamics are aligned with the ridges. (D) Normalized optical-flow-direction distributions corresponding to each frame in (C). The distributions show that actin polymerization dynamics are polarized and strongly guided by ridges. (E) Three snapshots 8 sec apart on 5 μm-spaced ridges with optical-flow vector fields superimposed on images; the actin polymerization dynamics are biased in the ridge direction but are also complex and chaotic. (F) Normalized optical-flow-direction corresponding to each frame in (E). The distributions show that actin polymerization dynamics are more weakly guided by the ridges and are more variable than those in (D). Ridge directions are indicated by dashed lines and arrows. All scale bars are 5 μm.

Figure 5.1B, the number of polymerization events decreased.

To quantify these dynamics, we applied a modified version of the Lucas-Kanade optical-flow algorithm [87,89], which has been shown to perform better than competing flow-field-analysis techniques on fluorescent images [84]. Optical flow provides pixel-scale information about the flow of intensity in a time series of images, and we have previously shown that the distribution of optical-flow directions can be used to quantify the guidance of actin-wave dynamics by ridges (Chapter 4). On the narrowly spaced ridges, the direction of actin flow was more polarized by ridges (Figure 5.1C), which resulted in flow-direction distributions having large amplitudes and narrow peaks in the ridge direction (Figure 5.1D). On the widely spaced ridges, actin dynamics were slightly biased by the ridges, but were also more chaotic and variable than on the narrowly spaced ridges (Figure 5.1E). Consequently, the distributions of optical-flow-direction distributions on widely spaced ridges were broad, with a weak guidance in the ridge direction (Figure 5.1F).

Although the dominant behavior of actin waves was guidance along ridges, freely nucleated waves (i.e., those that did not nucleate at the site of ridges) exhibited a wider range of behaviors. On the 1.5-μm-spaced ridges, where nucleation of waves mostly happened along the ridges (Figure 5.1A), the optical-flow direction distributions showed that actin dynamics were strongly guided by the nanotopography (Figure 5.1D). On 5-μm-spaced ridges, where nucleation occurred throughout the space between ridges (Figure 5.1B), the actin dynamics were less guided by the nanotopography and exhibited a wider array of dynamic behavior (Figure 5.1F). Thus, actin waves that did not nucleate on the high-curvature regions of 5-μm-spaced

ridges displayed more complex dynamics.

5.3.2 Modeling optical flow of actin-wave dynamics can quantify the influence of ridges.

The shape of the optical-flow-direction distributions indicates the strength of actin-wave guidance caused by differently spaced ridges. We employed a statistical model of bidirectional guidance to parameterize the optical-flow-direction distributions and quantify the strength of actin-wave guidance induced by ridges (Figure 5.2). The actin dynamics in *D. Discoideum* on ridges with spacings of 0.8 (Figure 5.2A) and 1.5 μm (Figure 5.2B) were strongly guided along the ridges, as indicated by the cumulative distributions of optical-flow directions. On the other hand, the actin-wave dynamics in *D. Discoideum* on ridges with spacings of 3 μm (Figure 5.2C) and 5 μm (Figure 5.2D) were guided more weakly by the ridges.

Ridge-induced guidance can be quantified using a modified bimodal-von-Mises model with constant offset (Chapter 4). Model fitting of the direction distributions yielded five fit parameters: the mean direction, θ; the concentration of motion, κ; and weights p_1, p_2, and p_3, which are the proportions of motion that are in the θ direction, in the $\theta+\pi$ direction, and uniformly distributed, respectively (Figure 5.2E, Methods, Chapter 4). The representative fits in Figure 5.2E accurately captured the nature of the corresponding distributions in Figure 5.2A–D. Guided actin dynamics in *D. Discoideum* on ridge spacings of 0.8 and 1.5 μm were highly concentrated in the ridge direction, with an average κ between 10 and 15 (Figure 5.2F). On the other

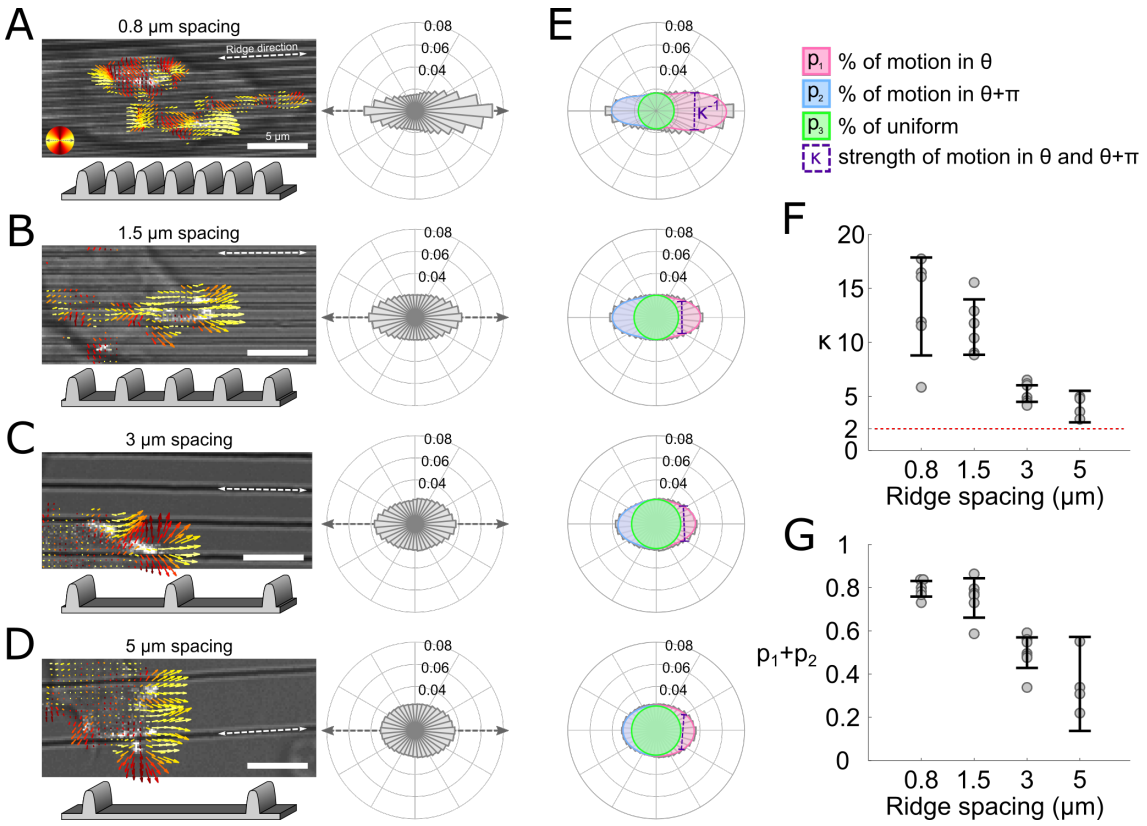

Figure 5.2: Actin-wave dynamics were more strongly guided by narrowly spaced ridges. (A) Representative snapshot of *D. discoideum* on 0.8-μm spaced ridges and the actin-wave-direction distribution measured by optical flow for the whole movie. The same procedure was performed for *D. discoideum* on (B) 1.5-μm-spaced ridges, (C) 3-μm-spaced ridges, and (D) 5-μm-spaced ridges. Stronger guidance was observed on narrower ridge spacings. (E) Cumulative actin-wave-direction distributions fit to a five-parameter modified-bimodal-von-Mises model. The model captured the nature of the distributions. (F) Concentration of motion (κ) in the modified bimodal-von-Mises model for each cell. Actin on 0.8- and 1.5-μm-spaced ridges had significantly larger κ than 3- and 5-μm-spaced ridges. $\kappa < 2$ (red dashed line) is not statistically distinguishable from a uniform distribution. (G) Proportion of actin guided by ridges ($p_1 + p_2$). $p_1 + p_2$ on 0.8- and 1.5-μm-spaced ridges that were guided by the ridges were significantly larger than the proportions on 3- and 5-μm-spaced ridges. Ridge directions are indicated by dashed lines and arrows. Optical-flow-vector directions relative to the ridge direction are indicated by color: light yellow is parallel to ridges and dark red is perpendicular to ridges. All error bars are the 95% confidence interval and all scale bars are 5 μm.

hand, guided actin dynamics on ridge spacings of 3 and 5 μm were weakly guided in the ridge direction with an average κ between 3 and 5. Note that fits for which $\kappa < 2$ are statistically indistinguishable from a uniform distribution (indicated by the dashed red line).

Whereas κ indicated how concentrated the guided actin dynamics were, the sum of the weights, p_1+p_2, indicated the proportion of dynamics that were subjected to the guidance. On ridges with spacings of 0.8 and 1.5 μm, roughly 80% of the actin dynamics were guided by ridges (Figure 5.2G). In contrast, roughly 50% of the actin dynamics on 3-μm-spaced ridges were guided, and about 35% of the actin dynamics on 5-μm-spaced ridges were guided (Figure 5.2G). Taken together, the two complementary parameters κ and $p_1 + p_2$ provide a quantitative means for making comparisons between actin dynamics on narrowly and widely spaced ridges; actin dynamics on narrowly spaced ridges were strongly guided with comparatively large κ and $p_1 + p_2$, whereas actin dynamics on widely spaced ridges are weakly guided with comparatively small κ and $p_1 + p_2$.

5.3.3 Greater actin-nucleation rate in a ridge pattern recapitulated topography-guidance behavior.

To investigate the nature of interactions between actin waves and ridges, we employed a dendritic-growth simulation of actin-filament assembly and disassembly with realistic biochemical rates, NPFs, and actin-filament-severing dynamics [41]. Nanotopography modulates actin dynamics via the enhancement of NPFs on regions

of high curvature [15, 16]. Thus, to capture the observed variation in actin-filament nucleation due to nanotopography, in the simulations we increased the activity of NPFs along periodic stripes that were the same widths as the ridges from Figures 5.1 and 5.2. This approach attempted to mimic the effect of ridges on actin polymerization dynamics without requiring the explicit inclusion of nanotopography in the simulations.

We employed the optical-flow analysis introduced in Figure 5.2 to measure the strength of pixel-scale guidance of actin waves in the simulations (Figure 5.3). The biomechanical simulations included individual actin monomers, filaments, branching, capping, and contacts between actin and the cell membrane. Thus, we employed a coarse-graining technique that converted z-projections of the simulated volume to what would be expected if the images had been acquired on a microscope with optical resolution of ∼250 nm [41] (Figure 5.3A).

Actin waves in the simulations on ridges with spacings of 1.5, 3, and 5 μm all had clear, leading-edge-driven waves that were identified by optical flow (Figure 5.3B). Notably, the wave fronts in Figure 5.3B were uniformly bright between the ridges, in contrast with wave fronts in Dicty shown in Figure 5.2A–D that were sparse. Although high-curvature textures induce increased NPF activity [15, 16], it is unclear whether the increase of NPF activity on ridges leads to a simultaneous decrease in NPF activity between ridges. Thus, to probe the mechanism behind topography-induced guidance, we performed two complementary sets of simulations, which we labeled as unconstrained (Figure 5.3C) and constrained (Figure 5.3D). Unconstrained simulations had an increased NPF activity along the high-curvature

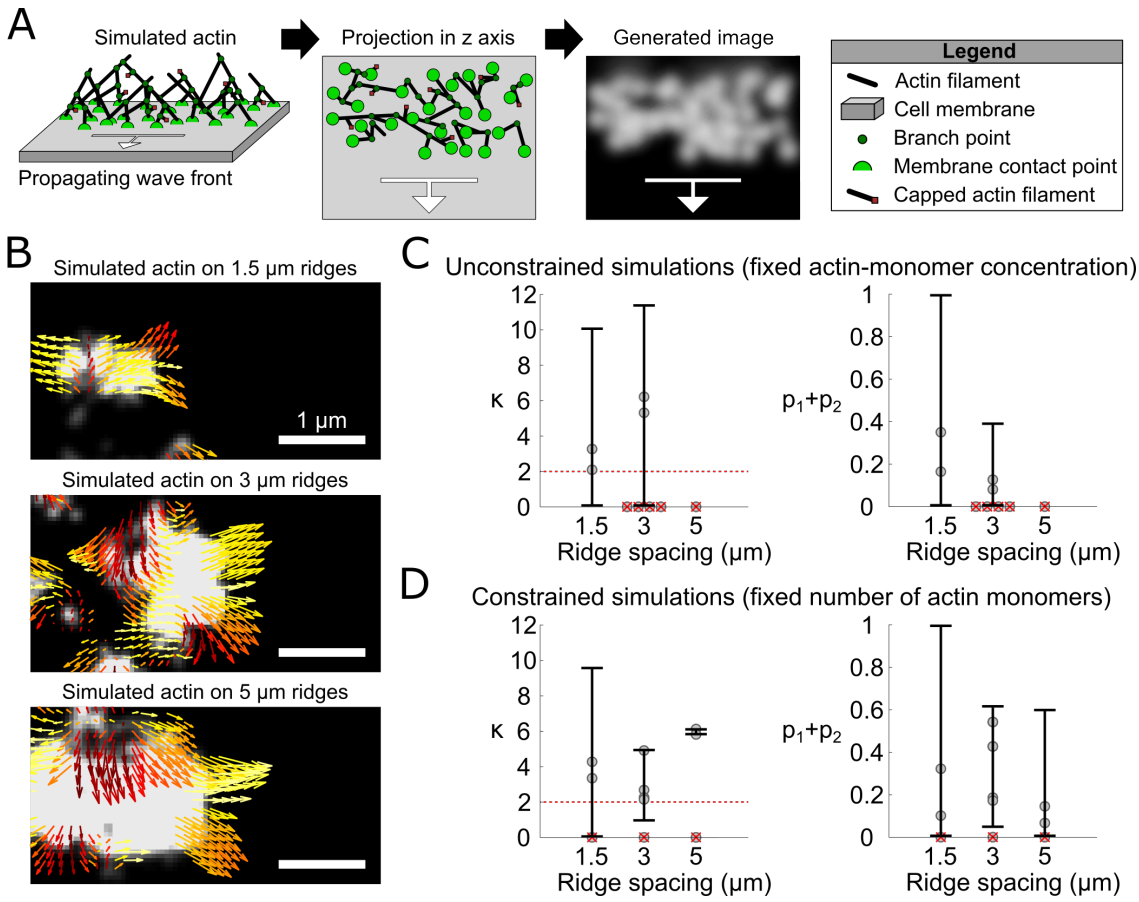

Figure 5.3: Patterning of simulated-nucleation-promoting-factors captures aspects of experimental topography-guidance phenotypes. (A) Actin simulations were coarse-grained to generate images akin to those expected from a microscope with ∼250 nm optical resolution. (B) Representative snapshots of experimental and simulated actin waves on ridges with spacings of 1.5, 3, and 5 μm. Optical-flow vectors are colored by direction: yellow is aligned with ridges and red is perpendicular. Two types of simulation conditions were used: unconstrained (C), which used upregulated NPF activity on ridges, and constrained (D), which used globally constrained NPF activity, (i.e., upregulation on ridges and downregulation between ridges) to mimic a redistribution of NPFs to ridges. Optical-flow distributions were fit to a bimodal-von-Mises model to quantify guidance strength. (C) Parameters from unconstrained simulations on ridges with spacings of 1.5, 3, and 5 μm. Weak-to-moderate guidance was observed. (D) Parameters from the constrained simulations on ridges with spacings of 1.5, 3, and 5 μm. The guidance in these simulations was stronger than that in the unconstrained simulations. Error bars are the 95% confidence interval and scale bars are 1 μm.

parts of the simulated nanoridges, which resulted in an overall global increase in NPF activity through the simulation space and thus an increase in overall actin-polymerization activity. To balance the increased NPF activity on ridges, NPF activity between adjacent ridges in the constrained simulations was reduced such that the total NPF activity remained constant. In practice, these two cases mimic two possible mechanisms for nanotopography-induced increases in polymerization activity. Unconstrained simulations mimic an upregulation of NPF activity due to curvature, whereas constrained simulations mimic a redistribution of NPFs, which would lead to having fewer NPFs between high-curvature regions while leaving the total NPF activity unchanged.

The fitting procedure used on the data in Figure 5.2 was applied to the optical-flow-direction distributions from the unconstrained and constrained simulations (Figure 5.3C and D, respectively). In the unconstrained simulations, guided actin dynamics on ridges with spacings of 1.5 and 3 μm exhibited weak guidance, whereas 4 out of 6 simulations on a 3 μm spacing and the simulation on a 5 μm spacing exhibited no guidance (Figure 5.3C). Around 30% of the actin dynamics on 1.5-μm-spaced ridges were weakly biased in the ridge direction, with $\kappa = 3$. About 15% of the actin dynamics on 3 μm spaced ridges were moderately guided, with $\kappa = 6$. In contrast, the constrained simulations exhibited a greater degree of ridge-induced bias in guided dynamics (Figure 5.3D). About 25% of the simulated actin on the 1.5 μm spacing was guided with $\kappa = 4$, about 40% of the dynamics on 3 μm spacing was guided, with $\kappa = 3$, and about 10% of the dynamics on 5 μm spacing was guided, with $\kappa = 6$. Note that a fit with $\kappa < 2$ is statistically indistin-

guishable from a uniform distribution. Thus, one of the simulations for each of the ridge spacings exhibited no bias in the ridge directions. In sum, the actin dynamics in the simulations were not as strongly guided as those in the experimental data, but there were some guided dynamics in simulations on each of the ridge spacings. Constrained simulations exhibited more biologically realistic guidance phenotypes.

5.3.4 Simulated and experimental actin-wave speeds were similar, and were unaffected by varying ridge spacing.

For further quantification of the similarities between experimental observations and simulations, we measured the speed of the actin waves in both the experimental and simulated images (Figure 5.4). Representative kymographs of actin waves in *D. Discoideum* on ridges with 0.8 μm and 3 μm spacings, indicated wave speeds on the order of 10 to 20 μm/min (Figure 5.4A). The polymerizing edge of the actin wave is variable and chaotic, which is especially clear on the 3 μm spacing where there are various protrusions that grow independently from the leading edge. Furthermore, depolymerization on the back end of the actin waves on both 0.8 and 3 μm spacings was slow, and thus remains bright in the kymograph. Representative kymographs of simulated actin waves on ridges with 0.8 and 3 μm spacings indicate wave speeds on the order of 5 to 10 μm/min (Figure 5.4B). The leading edge of simulated waves appeared to be coherent and move uniformly as compared to that in the experimental data. Furthermore, the depolymerizing (trailing) edge of the actin wave was well constructed and moved roughly as fast as the leading edge.

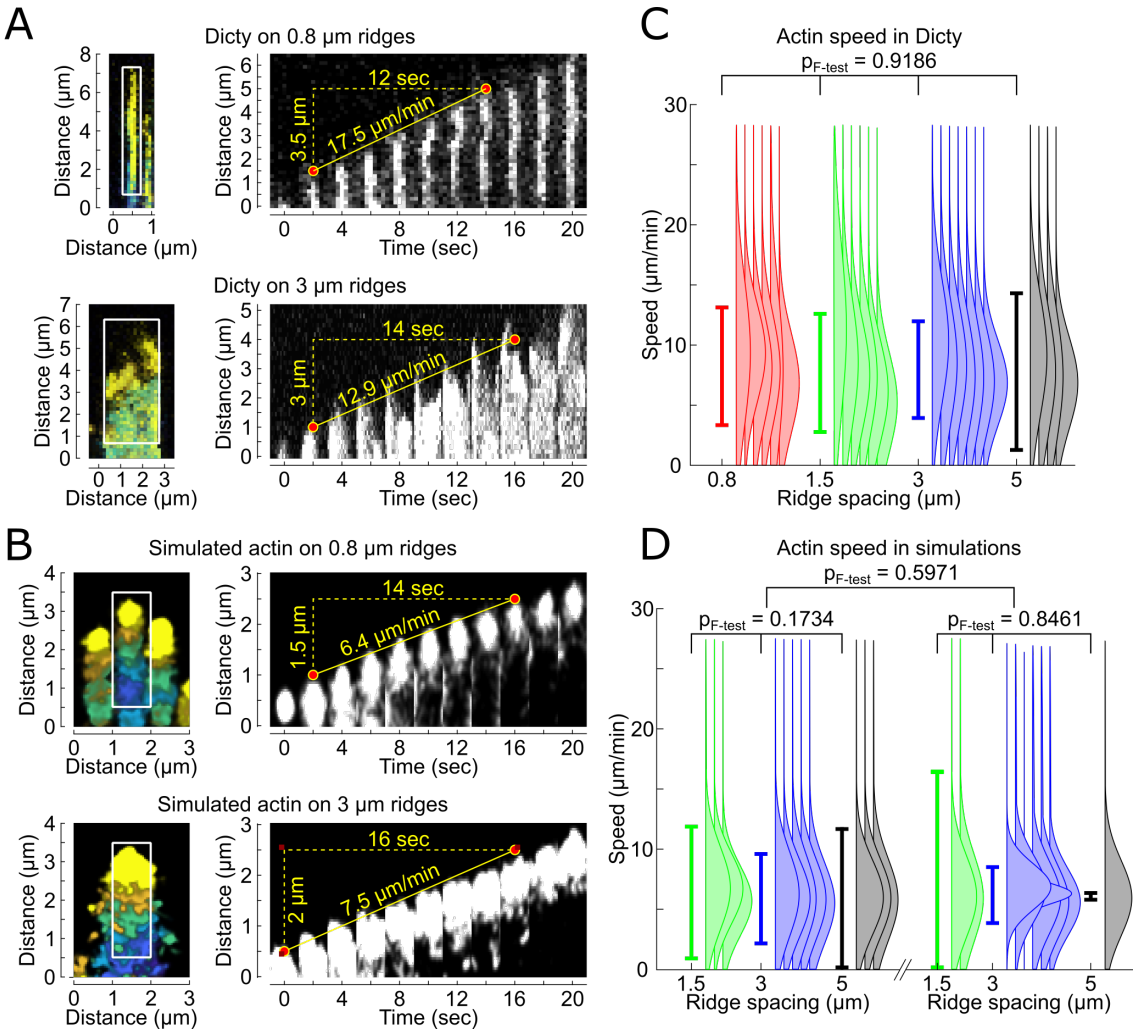
A
Dicty on 0.8 μm ridges
Distance (μm)
Distance (μm)
12 sec
17.5 μm/min
3.5 μm
Time (sec)
Dicty on 3 μm ridges
14 sec
12.9 μm/min
3 μm
B
Simulated actin on 0.8 μm ridges
14 sec
6.4 μm/min
1.5 μm
Simulated actin on 3 μm ridges
16 sec
7.5 μm/min
2 μm
C
Actin speed in Dicty
$p_{F\text{-test}}$ = 0.9186
Speed (μm/min)
Ridge spacing (μm)
D
Actin speed in simulations
$p_{F\text{-test}}$ = 0.5971
$p_{F\text{-test}}$ = 0.1734
$p_{F\text{-test}}$ = 0.8461
Speed (μm/min)
Ridge spacing (μm)
Ridge spacing (μm)

Figure 5.4: Experimental actin-wave speeds were unaffected by varying ridge spacings, which was recapitulated in simulations. (A) Representative time-lapses and kymographs of actin in *D. discoideum* on 0.8- and 3-μm-spaced ridges. The leading edge of actin waves was variable and chaotic but moved somewhat uniformly between ridges over time. Depolymerization at the back of the wave was slow and remained bright. (B) Representative time-lapses and kymographs of simulated actin on 0.8- and 3-μm-spaced ridges. The leading edge of simulated waves were uniform, sharply pointed, and moved in a spatially coordinated manner. Depolymerization on the back end of the wave was rapid with occasional afterburns that manifested in bright puncta behind the depolymerized edge. (C) The speeds of the actin-wave fronts according to optical-flow-based clustering and tracking. There was no statistically significant difference between actin-wave speeds on different ridge spacings ($p = 0.9186$, calculated using one-way ANOVA). (D) The speeds of the simulated-actin-wave fronts according to optical-flow-based clustering and tracking. There was no statistically significant difference between actin-wave speeds on different ridge spacings in the constrained simulations (left, $p = 0.1734$, calculated using one-way ANOVA), unconstrained simulations (right, $p = 0.8461$, calculated using one-way ANOVA), or between the two groups ($p = 0.5971$, calculated using two-way ANOVA).

To analyze all actin waves systematically in both the experimental and simulated images, we used optical-flow-based clustering and tracking (Chapter 4). Actin-wave speeds in *D. discoideum* on different ridge spacings were all centered around 8 to 9 μm/min, and there was no statistically significant difference between speeds on any spacings ($p = 0.9186$, calculated using one-way ANOVA) (Figure 5.4C). Similarly, simulated-actin-wave speeds on 1.5, 3, and 5 μm spacings were centered around 7 μm/min in both unconstrained (Figure 5.4D Left, $p = 0.1734$, calculated using one-way ANOVA) and constrained simulations (Figure 5.4D Right, $p = 0.8461$, calculated using one-way ANOVA). Furthermore, there was no difference in actin-wave speeds between constrained and unconstrained groups ($p = 0.5871$, calculated using two-way ANOVA). Finally, there was no significant difference in speeds between experimental data and unconstrained simulations or between the experimental data and constrained simulations. In sum, experimental and simulated actin-waves in all datasets moved in qualitatively different ways (i.e., polymerized edges were either chaotic or uniform, and depolymerized edges were either nonexistent or well formed), but at similar speeds.

5.3.5 Simulations of the actin cytoskeleton enable new quantitative measures of, and biomechanical insights into, actin-polymerization dynamics.

Latrunculin A is a drug that influences actin dynamics via the sequestration of cytosolic actin monomers. Latrunculin-A treatments have been shown to modify

polymerization-depolymerization dynamics [164] and impede or inhibit cell functions such as B-cell signaling [39]. Here, we use optical-flow-based analyses to perform a quantitative comparison of Latrunculin-A-treated and wild-type (WT) Dicty on 1.5 μm spaced ridges, and also to compare these experiments against simulations data of varying actin monomer concentrations (Figure 5.5). Topography-induced guidance was observed to be weaker in cells treated with Latrunculin A than in WT cells (Figure 5.5A). In Latrunculin-A-treated cells, optical-flow-direction distributions had an average κ on the order of 8 and $p_1 + p_2$ on the order of 0.7. Both κ and $p_1 + p_2$ were significantly smaller than those measured in WT Dicty on 1.5-μm-spaced ridges (p ¡ 1×10^{-3} in both cases). Furthermore, optical-flow-cluster tracking indicated that Latrunculin A caused a significant decrease in actin-wave speeds in treated cells (Figure 5.5C, $p = 3.45 \times 10^{-4}$).

To compare actin in Latrunculin-A-treated Dicty to simulated actin, we tested several maximum-free-actin concentrations in the simulations. Given that stronger guidance phenotypes were observed in constrained simulations (Figure 5.3), we used constrained conditions in further comparisons between simulations and experiments. There was no statistically significant difference between the κ and $p_1 + p_2$ values across simulated actin waves with different actin concentrations.

5.4 Discussion

In this work, we explored the dynamic behavior of the actin cytoskeleton in *D. discoideum* and in simulations on differently spaced nanoridges. We employed

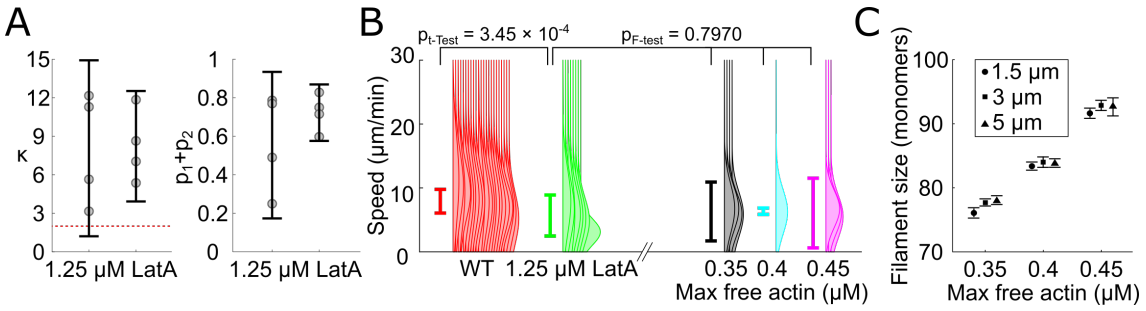

Figure 5.5: Latrunculin-treated Dicty was less guided and slower that WT Dicty on nanoridges. *D. discoideum* was treated with 1.25 μM Latrunculin A and imaged on 1.5-μm-spaced ridges; Latrunculin A is known to bind to actin monomers, and thus inhibits the polymerization of new actin filaments. (A) Systematic analysis of the optical-flow-direction distributions in Latrunculin-A-treated Dicty from four experiments on two separate days. Average κ on each day was on the order of 8 and $p_1 + p_2$ was on the order of 0.7. Both measures are less than those observed in WT Dicty on ridges with the same spacing. To try to recapitulate actin-monomer sequestration in simulations, the maximum concentration of free actin was systematically varied. (B) The speeds of the actin-wave fronts according to optical-flow-based clustering and tracking. Red is all WT experimental data on all ridge spacings, green is Latrunculin-A-treated Dicty, and black, teal, and pink are simulated actin at variable monomer concentrations. There was a statistically significant difference between actin-wave speeds in WT and Latrunculin-A-treated cells ($p = 3.45 \times 10^{-4}$), whereas no significant difference was found between simulated actin-wave speeds and Latrunculin-A-treated cells ($p = 0.7970$, calculated using one-way ANOVA). (C) Average actin-filament length in monomers measured from simulated actin at 0.35, 0.4, and 0.45 μM concentrations; this measurement is only available in the simulations. As the concentration of available actin monomers was increased the average filament length increased. Notably, the average filament length was unaffected by the ridge spacing. Error bars in (B) and (C) are the 95% confidence interval and in (D) are the standard error of the mean.

optical-flow-based modeling, clustering, and tracking to perform robust and systematic comparisons between experiments and simulations. We were able to quantify actin-wave dynamics in experiments and simulations despite apparent qualitative differences, particularly regarding the chaotic and variable leading edge in experiments and lack of a trailing edge in the simulations.

We parameterized optical-flow-direction distributions utilizing a bimodal-von-Mises model. The influence of nanoridges on actin dynamics can be assessed using two key parameters from these fits: the concentration of motion, κ, and the guidance proportion, $p_1 + p_2$. We found that nanoridges with spacings of 0.8 and 1.5 μm strongly biased the direction of actin polymerization, whereas widely-spaced nanoridges with spacings of 3 and 5 μm weakly biased the direction of actin polymerization, consistent with prior studies on whole-cell behaviors during guided cell migration [29].

To elucidate further the biomechanical interactions between cytoskeletal dynamics and nanotopography, we employed dendritic-growth simulations of filament assembly and disassembly with realistic biochemical rates, nucleation-promoting factors (NPFs), and filament-severing dynamics [41]. To simulate the effect of nanotopographic ridges on cytoskeletal dynamics, we contrasted two conditions. In unconstrained conditions, we upregulated NPF activity on ridges consistent with previous experimental data [15, 16]. The enhanced activation of NPFs in a ridge pattern could be altering signaling thresholds of biomechanical excitability [9, 71], which has been shown to induce rapid changes in cytoskeletal dynamics and overall cell behavior [3]. In constrained conditions, we both upregulated NPF activity on

ridges and downregulated NPF activity between ridges, which mimicked a redistribution of a fixed pool of NPFs preferentially to ridge locations. Although these simulation conditions don't specifically allow for the direct inference of the interaction between nucleation and nanotopography, they provide insight into the core mechanisms governing texture-induced guidance of actin.

Using optical flow and the bimodal-von-Mises model, we showed that actin-wave guidance was achieved in both unconstrained and constrained conditions. Guidance in the constrained conditions was stronger than the unconstrained conditions, but in both types of simulations the actin waves were less guided than in experiments. On the other hand, the speed of actin waves in simulations was comparable to those measured in the experiments. This observation is particularly noteworthy because (1) the simulations were adopted without substantial changes to the parameters from prior studies and (2) although speeds are determined by micron-scale motion, the biochemical rates and components in the simulations are on the order of several nanometers. In effect, because small errors in the biochemistry lead to substantive changes in micron-scale motion, quantitative agreement of actin-wave speed is particularly profound.

As a further test of the agreement between experiments and simulations, we compared responses to a chemical perturbation of the actin cytoskeleton. A decrease in the concentration of actin monomers—the fuel for polymerization—can be directly simulated and also experimentally achieved through treatment of cells with Latrunculin A. The simulations allowed for extraction of information that cannot be obtained from the experiments. In particular, we found that the average length

of actin filaments decreased roughly linearly with a decrease in actin-monomer concentration. In both experiments and simulations, we did not see a large decrease in the speed of actin waves, although a small decrease was noted in experiments.

In addition to this small discrepancy between simulations and experiments, simulations systematically exhibited less guidance than experiments and the simulated actin waves were typically shorter than the experimental waves (i.e., depolymerizing after a delay time and yielding a polymerized region of constant size). On the other hand, in experiments the actin waves exhibited a long tail after the leading polymerization edge. These observations suggest that that the ridges may stabilize the actin network and inhibit depolymerization. Indeed, prior work has demonstrated that extracellular structures can modulate micron-scale actin structures [125, 165], although the effect on filament-scale actin dynamics is unclear. On the other hand, our observations could also indicate that the dynamics of actin-network disassembly are not yet fully captured in the model.

Linked together by the robust quantification of optical-flow-based analyses, experiments and simulations on guided actin waves provided a robust framework for probing the mechanisms of texture sensing and contact guidance, which are ubiquitous processes in the natural world.

5.5 Materials and Methods

5.5.1 Cell Culture and Imaging

The limE-Δcoil overexpressing *Dictyostelium discoideum* cells (in an AX3 background) were cultured in HL-5 medium at 1–4 $\times 10^6$ cells/mL with 50 mg/mL hygromyocin B (Sigma-Aldrich H3274). We imaged cells in the pre-aggregate state. Cells were harvested at 4×10^6 cells/mL and shaken at 150 rpm in a beaker with a density of 2×10^7 cells/mL. Cells were then developed for 4 hours in development buffer (5 mM Na_2HPO_4, 5 mM NaH_2PO_4, pH 6.2, 2 mM $MgSO_4$ and 0.2 mM $CaCl_2$). During development, cells were stimulated every 6 minutes with pulses of 50 nM cAMP. The cells were then washed twice in phosphate buffer (5 mM Na2HPO4, 5 mM NaH2PO4, pH 6.2). To inhibit cell-cell communication, cells were treated with 2 μM caffeine (Sigma-Aldrich C1778) for 30 min, while being shaken at 150 rpm. For imaging, 300 μL of cell solution with density 5×10^5 cells/mL was added to a multi-well plate. After waiting 5 min for the cells to adhere to the surface, 50 μM of cAMP (Sigma A3262) was added to cells to initiate chemokinesis. Latrunculin A (Sigma L5163) perturbations were performed via the addition of the drug to a final concentration of 1.25 μM (and a final concentration of 0.05% DMSO by volume) after cells adhered to the substrate.

Fluorescence and bright field images were obtained on a Leica TCS SP5 confocal microscope (Leica TCS SP2 for Latrunculin A experiments) with a 100× objective, and a frame rate of 0.5 frames/second.

5.5.2 Ridge Fabrication

Structures were fabricated according to the protocols described previously [29]. We used a Ti:sapphire laser (Coherent Mira 900F) to perform multiphoton absorption polymerization. A region of total size 300 μm $\times$ 300 μm was patterned with 200- to 300-nm-wide ridges with uniform spacings of 0.8, 1.5, 3, or 5 μm. The ridges were fabricated using an acrylic resin containing 49 wt% tris-(2-hydroxyethyl) isocyanurate triacrylate (SR368, Sartomer), 49 wt% dipentaerythritol pentaacrylate (SR399, Sartomer), and 2 wt% Lucirin TPO-L (Ciba). This process yielded a master structure, which was then developed in dimethylformamide and ethanol. In experiments, we made replicas of the master structure using a composite PDMS mold [166].

5.5.3 Image Analysis

Images were processed with modified MATLAB software from Chapter 4. Optical flow was calculated using the Lucas-Kanade method [89] with a gaussian-weighted window with $\sigma = 0.642$ μm. Distributions of optical-flow-vector directions were fit with a bimodal-von-Mises model and the fit parameters κ, p_1, and p_2 were used to interpret the model output.

Actin-wave speeds were calculated according to Chapter 4 with a clustering parameter threshold of 0.1, and global reliability threshold for each time-series image chosen empirically.

5.5.4 Actin Simulations

Simulations were performed using a custom C++ program created by modifying the one published previously [41]. A rectangular simulation domain of size 8 μm $\times$ 5 μm was used. From the simulation results, we measured the actin filament density within 200 nm from the cell membrane with a planar resolution of 10 nm $\times$ 10 nm and a temporal resolution of 0.5 seconds.

We compared the simulation results with recorded images of limE-Δcoil-GFP polymerization by transforming the simulated F-actin density via convolution with a Gaussian kernel matching the resolution of our confocal microscopy images of $\sim$250 nm.

Chapter 6: Analysis of Actin Dynamics in a Biological Context: Actin Dynamics During Cancer Metastasis

This chapter is an adapted excerpt from Ilina, Campanello, Gritsenko, Vullings, Wang, Bult, Losert, and Friedl [167]. Text and figures were adapted and reproduced under a CC BY 4.0 license. Olga Ilina and Pavlo Gritsenko performed the experiments, Leonard Campanello performed the image processing and analysis, and Olga Ilina, Leonard Campanello, and Pavlo Gritsenko wrote the paper.

6.1 Overview

Cancer invasion programs adapt by switching between collective and single-cell dissemination. However, current intravital microscopy models for epithelial cancer in mice fail to recreate such invasion plasticity reliably. We microimplanted breast-cancer spheroids into the murine mammary fat pad and performed live-cell imaging of the microenvironmental conditions and cytoskeletal adaptation during the collective-to-single-cell transition *in vivo*. E-cadherin-expressing 4T1 and E-cadherin-negative MMT tumors both initiated collective invasion along stromal structures, reflecting invasion patterns in 3-D organotypic culture and human pri-

mary ductal and lobular carcinoma. Collectively invading cells developed weakly oscillatory actin dynamics, yet provided zones for single-cell transitions with accentuated, more chaotic actin fluctuations. These studies indicate that collective invasion *in vivo* is a dynamic niche and an efficient source for single-cell release.

6.2 Background

Progression and fatal outcome of breast-cancer disease result from the emergent ability of cancerous cells to invade tissue, to cope with complex tissue microenvironments, and to adapt their metastatic dissemination by switching between collective-migration and individual-cell-migration programs [168]. Early steps and molecular drivers of single-cell dissemination of epithelial cancers *in vivo* were identified by intravital microscopy (IVM) in rodent models, including oncogenic mutations in Wnt, EGFR, p53 (also known as Trp53) and TGF-β signaling pathways [169–171]. IVM has further revealed how tumors co-evolve, with the reactive tumor stroma and undergo anatomic, molecular, and functional reprogramming, and had underscored the significance of tumor-associated macrophages directing local invasion and systemic dissemination [172, 173].

In epithelial cancers assessed by histopathological analysis, collective cell patterns are abundant at the invasion front [174–176]. Collective invasion occurs in cell groups or strands connected and coordinated by adherens and other cell-cell junctions that mediate multicellular polarity, actomyosin contractility, and cell-cell signaling [172]. Subsequent to local epithelial cancer invasion, persisting cell-cell

interactions can support collective metastasis by tumor-cell clusters circulating in peripheral blood and collective organ colonization [177, 178]. However, to date, IVM models of epithelial cancers, including breast cancer and colorectal cancer, have not been able to detect and mechanistically interrogate collective invasion reliably [169, 179, 180]. As a consequence, *in vivo* insights into collective invasion in epithelial cancers, the guidance of collective invasion by tissue structures, and the mechanisms enabling transitions between collective and single-cell invasion remain lacking.

Here, we applied microsurgical implantation of multicellular breast cancer spheroids into the mammary fat pad, followed by intravital mammary window imaging. Our experiments enabled us to identify principles of collective invasion, transitions to single-cell dissemination and associated modulation of cytoskeletal states.

6.3 Results

6.3.1 Implantation and window-based monitoring as a model system of primary mammary carcinoma and metastasis

To create a model for monitoring collective invasion of breast cancer cells by intravital microscopy, the mammary imaging model [171] was adapted for microimplantation of multicellular spheroids at the collagen-containing border of the 4th mammary fat pad (Figure 6.1A). Up to 10 4T1 and MMT spheroids, which contained intercellular junctions including E-cadherin (4T1), -catenin and p120 catenin (4T1, MMT), were implanted in the same fat pad in order to mimic multifocal

disease [181]. The integrity of spheroids, connective and adipose tissues, and vascular networks was preserved after implantation (Figure 6.1B), consistent with minimally invasive microsurgery. Multifocal tumors developed spontaneous micro and macrometastasis (Figure 6.1C) and grew exponentially for periods up to 3 weeks (Figure 6.1D). 4T1 cells were separately injected as suspensions and established bulky tumors without signs of collective invasion. Thus, the mammary imaging model recapitulated the growth of primary carcinoma lesions and the subsequent distant metastasis.

6.3.2 Intravital microscopy of invasion and individualization

Collective cell invasion in both 4T1 and MMT tumors initiated within 1-2 days after implantation irrespective of differences in E-cadherin expression (Figure 6.2A–B). 4T1 (i.e., E-cadherin expressing) cells invaded as solid collective strands with detectable leader cells (Figure 6.2C). MMT cells that lacked E-cadherin but expressed N-cadherin invaded in a less-organized manner, which is consistent with previous reports [182], but nevertheless formed collective networks with multicellular organization, head-to-tail cell alignment, and actin enrichment along cell-cell junctions (Figure 6.2D).

Both 4T1 and MMT cells were able to detach and migrate individually, with elongated, spindle-shaped morphology that involved substantial actin activity (Figure 6.2A–B). However, individualization was more abundant in MMT compared with 4T1 tumors, which developed more frequent tip and detached cells, despite

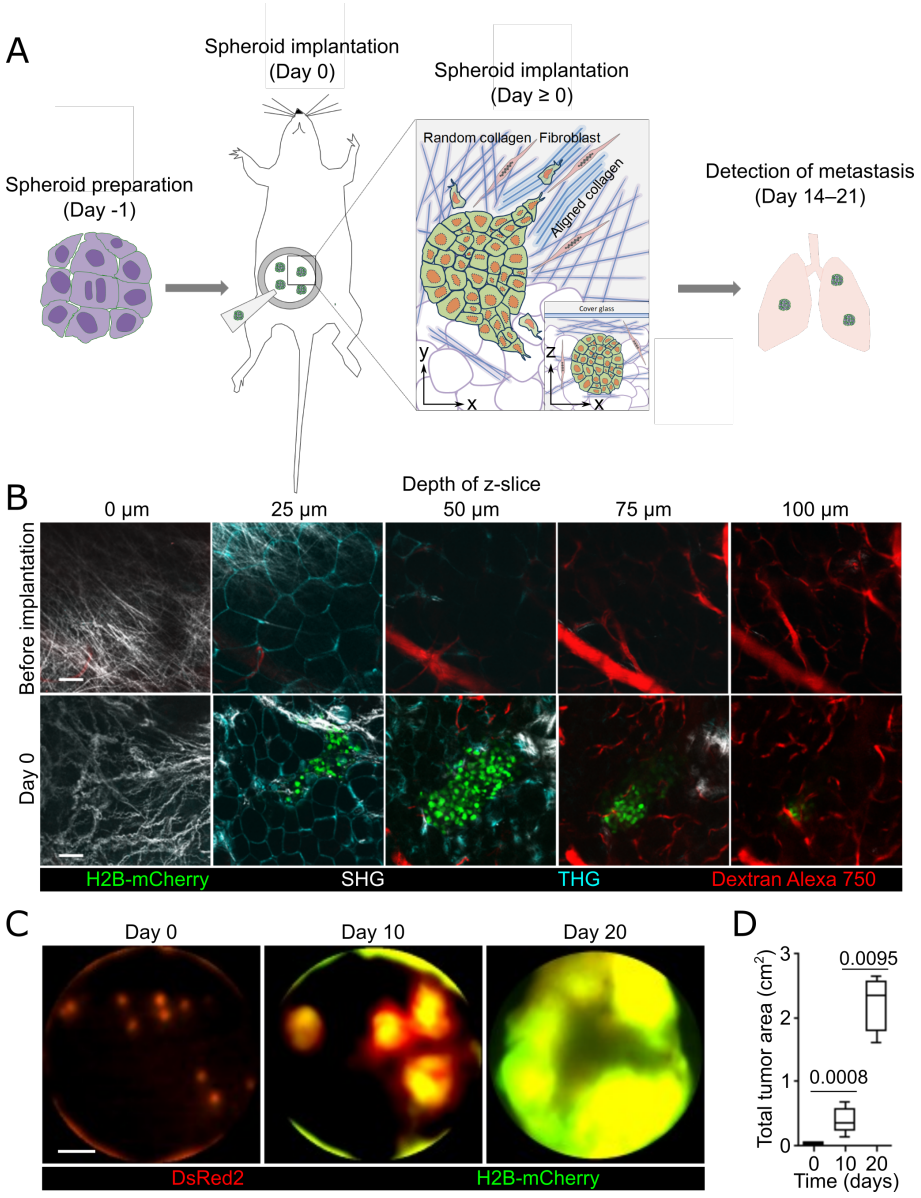

Figure 6.1: Microimplantation of tumor spheroids recapitulated the growth of primary carcinoma and subsequent distant metastasis. (A) 4T1 and MMT spheroids were prepared *in vitro* and implanted in the 4th mammary fat pad, and went on to form metastatic lesions 2–3 weeks after implantation. (B) The integrity of the spheroids, surrounding connective and adipose tissues, and vascular networks was preserved after the minimally invasive microsurgery. (C, D) Spheroids spontaneously developed metastatic tumors over 2–3, weeks which grew in size exponentially.

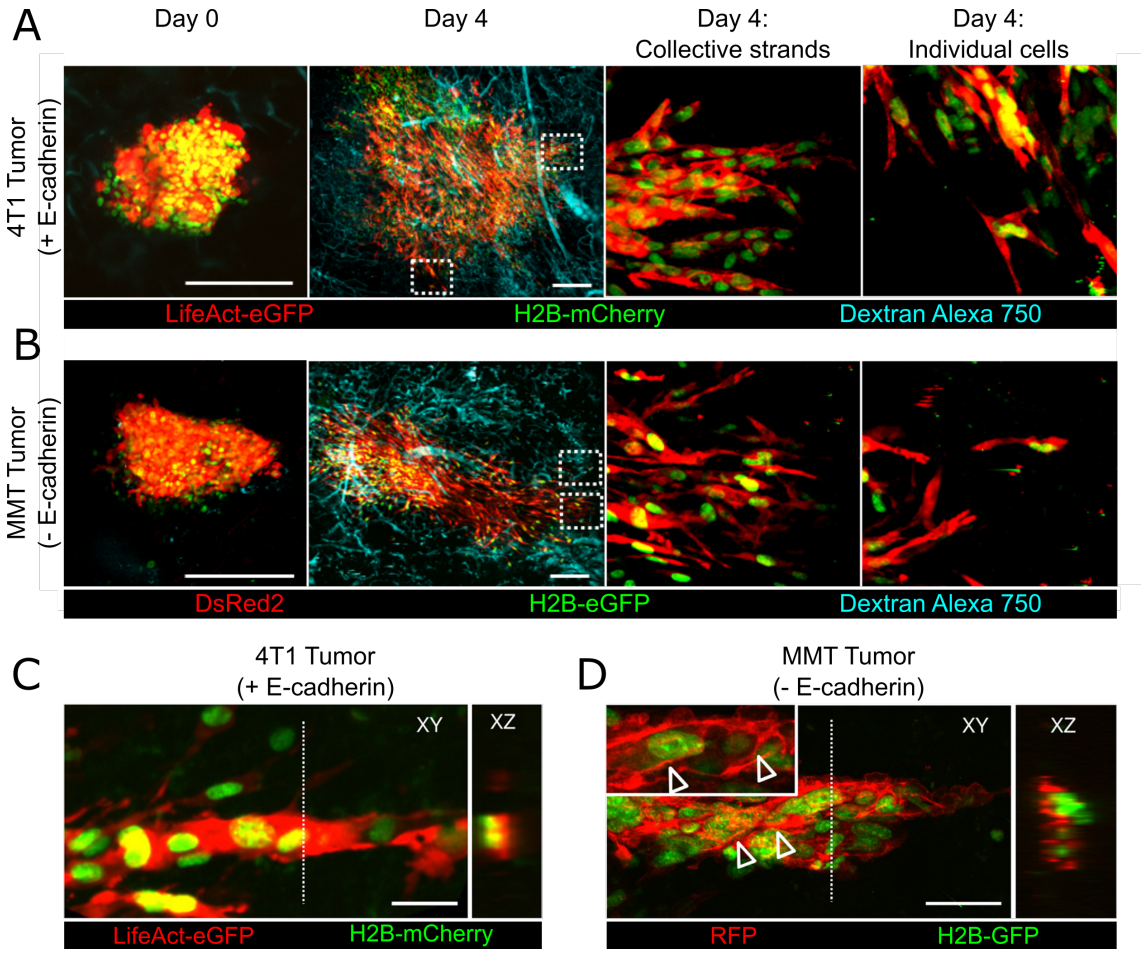

Figure 6.2: Collective and individual-cell invasion patterns and angiogenesis in the mammary tumor imaging model.Time-course of (A) 4T1- and (B) MMT-tumor growth and angiogenesis monitored by two-photon microscopy. Images are montaged maximum-intensity projections of three channels; z-stacks were obtained in 5 μm intervals. Dotted-line ROIs were used to show close-ups of collectively invading strands and single cells. Zoomed-in ROIs of (C) 4T1 and (D) MMT cells in the mammary fat pad 4 days after spheroid implantation. Both cell types exhibited collective-invasion phenotypes. Dashed lines mark the position of cross-section planes for orthogonal views and arrowheads indicate enrichment of Lifeact-eGFP along cell-cell junctions.

having an apparent reduction in actin expression. The inverse association between cell individualization and E-cadherin expression in the spheroid implantation model *in vivo* is consistent with increased single-cell release in 3-D organotypic culture of MMT compared with 4T1 spheroids and in patient samples from human lobular carcinoma compared with ductal breast carcinoma [176].

6.3.3 Investigating actin and cell-shape dynamics during the collective-to-single-cell transition

Plasticity of cancer cell invasion is associated with an adaptive actin cytoskeleton. Cortical actin networks *in vitro* define the shape, polarity, and force transmission in individually moving cells [183], and further stabilize adherens junctions and transmit long-range forces across connected cells during collective migration [184]. To address whether actin dynamics in individual and collective invasion differ *in vivo*, the intensity fluctuations of Lifeact-eGFP in 4T1 tumors transiting from collective to single-cell migration were quantified (Figure 6.3).

Individual cells in and around the tumor were identified and categorized as detached (1), tip (2), or bulk (3) (Figure 6.3A). Boundary outlines were traced and analyzed using a semi-automatic cell-shape-analysis workflow to measure the dynamic behavior of actin along the cell boundary [29, 185] (Figure 6.3B). Actin-intensity profiles were captured in equally spaced wedges along the cell boundary. Wedges were associated frame-to-frame with a minimum-squared-distance criterion to create time-lapse profiles of actin intensity on a per-wedge-per-frame basis (Fig-

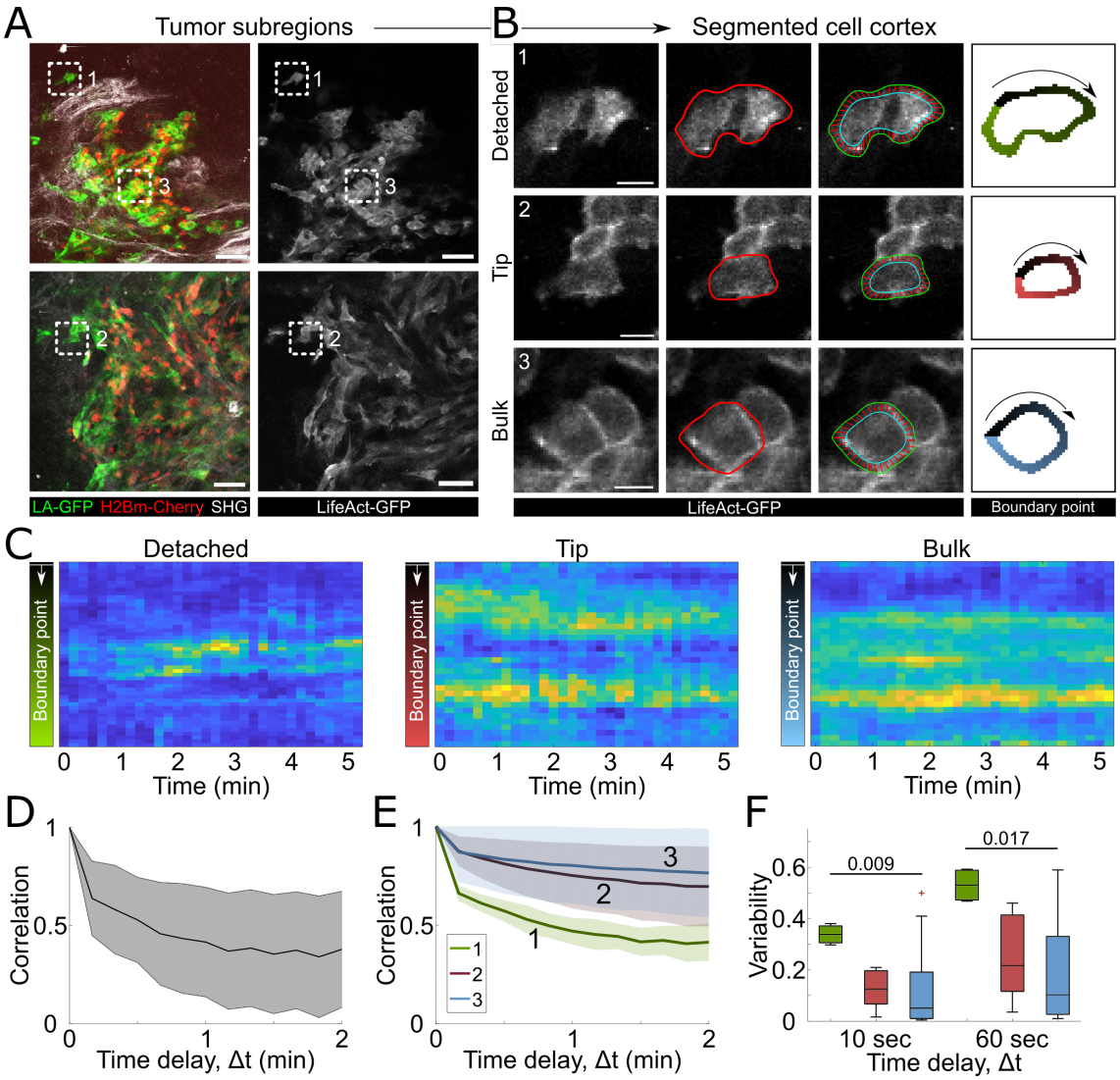
A
Tumor subregions
B
Segmented cell cortex
Detached
Tip
Bulk
LA-GFP H2Bm-Cherry SHG
LifeAct-GFP
LifeAct-GFP
Boundary point
C
Detached
Tip
Bulk
Boundary point
Time (min)
D
Correlation
Time delay, Δt (min)
E
Correlation
Time delay, Δt (min)
F
Variability
0.009
0.017
10 sec
60 sec
Time delay, Δt

Figure 6.3: Actin dynamics during collective and single-cell invasion. The time-dependent shape of each cell was extracted by semi-automatic shape segmentation from sequential single-imaging planes, and the Lifeact-eGFP intensity along the cell periphery was obtained from equal segments 2.07 μm inward from the cell boundary. (A) 4T1 cells at different invasion position *in vivo* 4 days after implantation. Segmented cells were categorized as detached (1), tip (2), and bulk (3), and series of boundary wedges were calculated and tracked for time-dependent analysis of actin intensity. (C) Mean-actin-intensity kymographs from wedges. Wedges were associated frame-to-frame using a minimum-squared-distance criterion. Detached cells exhibited rapid fluctuations, whereas tip and bulk cells exhibited slower and less-intense fluctuations. (D) Time-delay autocorrelation of the actin-intensity profile for the detached cell from (B). Time-delay autocorrelations indicate how correlated an intensity profile is with a time-shifted copy of itself. The time-delay autocorrelation equals 1 when the time-delay parameter, Δt is 0, and decays based on how quickly the two intensity profiles diverge. The black line is the mean and the gray region is the standard deviation calculated at each time delay, Δt. (E) Aggregated time-delay-autocorrelation curves of actin intensity from 4 detached (green), 8 tip (red), and 15 (bulk) cells, respectively, from 3 independent tumors. Intensity profiles from detached cells diverged more quickly than tip and bulk cells. (F) Intensity variability for intervals of 10 s (representing fast fluctuations) and 60 s (slow fluctuations) within detached (green), tip (red), and bulk cells (blue). Significant differences were found when comparing the mean variability between detached and bulk cells. The box plots in (F) are of the median (black line), IQR (box), and range (whiskers). P-values were obtained with the Tukey-Kramer multiple comparisons test. Scale bars were 50 μm in (A) and 10 μm in (B).

ure 6.3C). Intensity-over-time profiles in detached cells exhibited rapid fluctuations at different times and spatial locations along the cell periphery. Tip and bulk cells exhibited slower and less frequent intensity spikes (6.3C).

The extracted actin-intensity profiles were characterized and parameterized by time-delay autocorrelations in a wedge-by-wedge manner (Figure 6.3D). The error bars represent the standard deviation of the time-delay autocorrelation for each value of Δt. Time-delay autocorrelations indicate how similar an intensity profile is with a time-delayed replica of itself. When the time-delay parameter, Δt, is equal to zero then the correlation value is 1, and the autocorrelation decay rate indicates how quickly the intensity profiles diverge. Time-delay autocorrelations for the representative cells in Figure 6.3A–C demonstrate how rapidly intensity fluctuations decorrelate over time. Detached cells quickly diverge in actin-intensity behavior, whereas tip and bulk cells do not (Figure 6.3E).

Amoeboid cells moving along extracellular-matrix-like substrates *in vitro* developed actin waves reaching speeds of $\approx 10\mu$m/min [29], with calculated changes in polymerization on timescales of seconds [186]. On the other hand, cell protrusions, such as ruffles or pseudopods, remodel on a timescale of minutes [186]. To test whether actin dynamics *in vivo* have similar dynamic properties, we probed the intensity variations for 10 and 60 sec time delays in collective and single-cell migration *in vivo*. Systematic measures of variability, which were defined as 1 minus the time-delay autocorrelation for a particular time-delay, Δt, indicated that autocorrelations at 10 and 60 sec were significantly different between detached cells and bulk cells (Figure 6.3F). Taken together, the data in Figure 6.3 indicate an upregulation

of actin variability after collective-to-single-cell individualization from the invasion zone.

To connect the dynamic behavior of actin to cell shape, we measured and analyzed fluctuations in the extracted cell boundaries over time (Figure 6.4). Detached cells exhibited a significant amount of protrusive motion, whereas bulk cells were more quiescent (Figure 6.4A). Interactions between the cytoskeleton and ECM are most efficient for protrusions and features on the order of 2 μm in size [29]. We observed that detached cells exhibited many protrusions greater than 2 μm in size between adjacent frames, whereas bulk cells were relatively quiescent and had few large protrusions (Figure 6.4B). The gray regions indicate the standard deviation of boundary motion, thus when the gray regions fall above the 2 μm line, at least 15% of the boundary motion is of magnitude greater than 2 μm. The aggregate and high-percentile behavior in all detached, tip, and bulk cells is similar (Figure 6.4C), which indicates that boundary fluctuations are roughly the same size in all cases. However, boundary motion with magnitude $\geq$ 2 μm occurred significantly more frequently in detached and tip cells than in bulk cells (Figure 6.4D).

6.4 Discussion

Although collective invasion patterns are abundant in clinical samples of epithelial cancers, including breast carcinoma [174–176], current intravital-microscopy models of breast cancer were insufficient to detect and mechanistically interrogate collective invasion reliably [170, 171, 179]. Reasons for this model insufficiency are

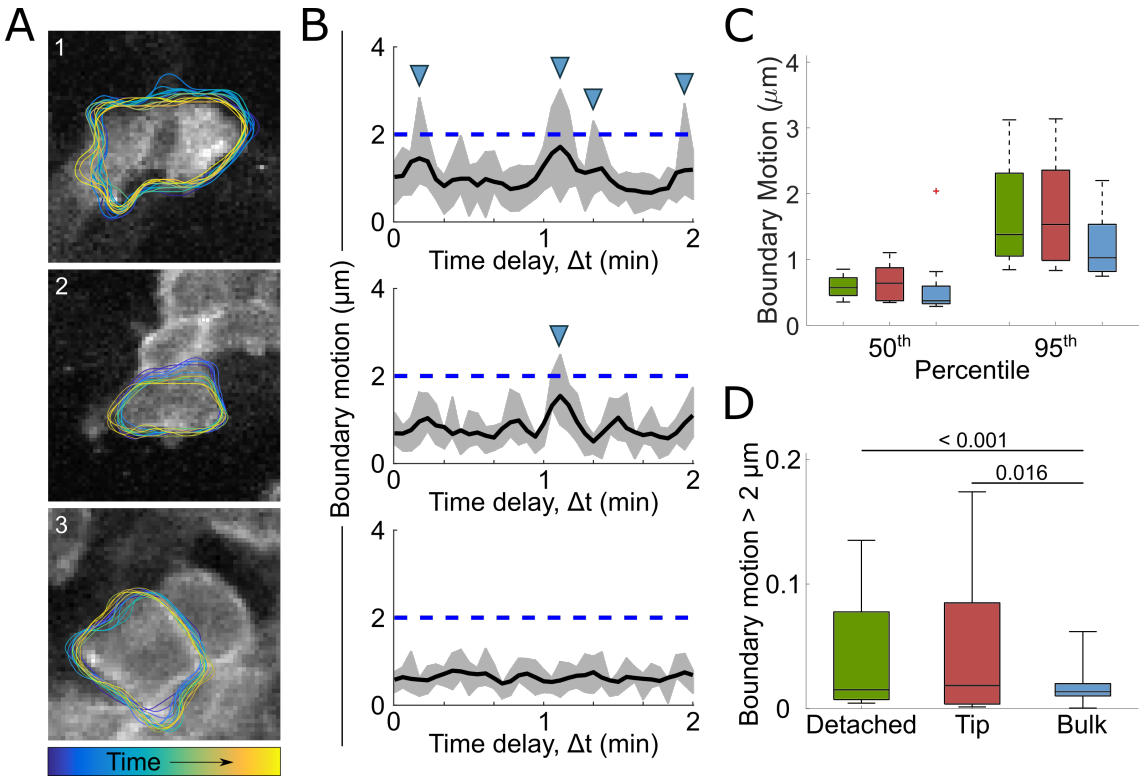

Figure 6.4: Detached and tip cells exhibited significantly more large-amplitude membrane fluctuations. (A) Cell boundary motion traces and their obtained from time-lapse sequences for detached (1), tip (2) and bulk (3) cells. (B) Boundary motion distributions over time for the representative cells in (A). Each cell exhibited similar background behavior, but detached and tip cells experienced a higher frequency of large-amplitude protrusion events than bulk cells. (C) Box plots of background (median) and high-percentile behavior (95^{th} percentile). Both background and high-percentile behavior is similar in all cell types. (D) The percentages of motion with a magnitude greater than 2 μm, the characteristic length scale of membrane fluctuations, for all detached, tip, and bulk cells. There are significantly more > 2 μm events in detached an tip cells than in bulk cells. Box plots in (C), (E) and (F) show the median (black line), IQR (boxes), and range (whiskers). P-values were obtained with the Tukey-Kramer test for multiple comparisons.

likely multifactorial, based on (1) lack of cell-cell junctions when tumor-cell suspensions are implanted; (2) excessive growth, which might cause circular tissue compression and disable multicellular invasion; and (3) a bias in genetic mouse models, which disable or minimize cadherin-based cell-cell junctions and possibly favor individual-cell, but not collective, behaviors. To overcome this problem, we used orthotopic microimplantation of multicellular spheroids of murine breast cancer cells into the mammary fat pad/stroma interface, monitored by intravital microscopy, as a reliable model of collective invasion followed by a transition to individual cell detachment *in vivo*.

Using spheroid microimplantation at the edge of the mammary fat pad, this intravital microscopy approach captured critical early steps of collective invasion and cytoskeletal plasticity in breast-cancer tumors. With transition from collective to single-cell migration, individually disseminating cells exhibited oscillatory behavior of the actin cytoskeleton and abandoned strict alignment along collagen fibers. Such collective-to-single-cell transitions arguably broaden the ability of tumor cells to cope with different tissue topologies and escape from the primary site [172].

In both E-cadherin-positive and E-cadherin-negative cells, implanted spheroids supported tumor-like topology and cell-cell cohesion for emerging collective invasion followed by gradual individualization. E-cadherin is considered an important gatekeeper of epithelial functions. Because single-cell events are enhanced in epithelial tumors when E-cadherin is downregulated [176], E-cadherin was initially considered to counteract local tissue invasion and metastatic spread [187]. However, in clinical breast cancer, the E-cadherin status does not predict metastatic outcome and prog-

nosis [176, 188]. Similar to these clinical data, E-cadherin-negative MMT tumors, albeit developing more frequent cell individualization compared with E-cadherin-expressing 4T1 tumors, did not give rise to increased rates of distant metastasis. Beyond mechanical cell-cell cohesion, other pathways might control the metastatic outcome in MMT and 4T1 cells, including oncogenic signaling, sensitivity to growth factors and mechanoregulation [170, 172, 173].

Our data further reveal plasticity of the actin cytoskeleton during the collective-to-single-cell transition *in vivo*, as predicted from *in vitro* and *in silico* models [183, 189]. A relatively quiescent actin cytoskeleton in the collective invasion zone possibly fulfills a dual function in (1) controlling both the stability and turnover of cell-cell junctions, and (2) providing a starting point for actin-rich protrusions at the invasion front. Leader cells that extended outwards to the stroma still retained overall quiescent actin dynamics comparable to those of bulk cells, but developed large protrusions at rates comparable to those in individual cells. Likely as a consequence of detachment, actin dynamics in individually moving cells rapidly switch dynamic character, suggesting that the actin cytoskeleton in invading tumor cells is an excitable system with dynamic focalization and protrusive bursts similar to traveling actin waves in moving *Dictyostelium discoideum* amoebae and fibroblasts migrating on 2D substrate *in vitro* [185, 186]. We consider spheroid microimplantation, combined with fate tracing of distinct invasion modes, as a potentially suitable model to barcode invasion mechanisms and stromal niches in primary lesions, and assess the relevance of these mechanisms for distant metastasis formation and resistance to therapy [190, 191].

When benchmarking *in vitro* and *in vivo* analyses of cancer cell invasion, the spheroid microimplantation strategy closes a validation gap by reflecting invasion types and plasticity derived from both 3-D organotypic culture and clinical samples [174, 176]. Multiple spheroids can be implanted in the same mouse to increase the surface area of the tumor-stroma interface and collect larger data sets. Multiple microlesions further increase the tumor mass, and enable spontaneous distant metastasis from these lesions, and this reduces animal consumption and improves data quality from the same mouse. Because intact spheroids are implanted, the strategy will be amenable for epithelial cancer organoids or dissected tumor microtissues from patients to create mouse avatars for personalized medicine.

6.5 Materials and Methods

6.5.1 Experimental methods

For a detailed explanation of experimental methods, including the antibodies and reagents, cell lines and culture, spheroid generation, immunohistochemistry, and confocal and two-photon microscopy, please refer to [167].

6.5.2 Analysis of actin and cell-shape dynamics

Actin dynamics were measured via Lifeact-eGFP fluorescence intensity in space and time from single imaging planes through the center of the cell body without signs of drift. Using a custom MATLAB code based on [29, 185], cell outlines were semiautomatically segmented from source images, and the boundary traces

were calculated on a subpixel basis using 200 boundary points using an active-contour algorithm. Source images had a pixel resolution of either 3.02 μm or 1.45 μm and an adjusted signal-to-noise ratio.

Wedges based on the cell boundary were calculated by applying morphological erosion on the segmented cell boundaries, using an active-counter algorithm with 200 boundary points to generate a boundary trace, and generating a mapping between the original boundary and eroded boundary in a minimum-least-squares fashion [185]. Separations between wedges were 1.73 μm, which was larger than the average fluctuation in measured boundary position. Thus, this separation was sufficient to capture cortical actin with accuracy. The mean intensity per wedge boundary region was plotted over time on a wedge-by-wedge basis as a kymograph and used for calculating the time-delay autocorrelation.

For the n^{th} boundary index with average background intensity $\bar{I}$, time-delay autocorrelation for time delay Δt was defined as

$$c_n(\Delta t) = \frac{\sum_{t=0}^{T}[I_n(t+\Delta t) - \bar{I}] \cdot [I_n(t) - \bar{I}]}{\sqrt{\sum_{t=0}^{T}[I_n(t+\Delta t) - \bar{I}]^2 \cdot \sum_{t=0}^{T}[I_n(t) - \bar{I}]^2}}. \tag{6.1}$$

The mean background fluorescence of the cell, $\bar{I}$, was determined based on the eroded cell boundary which was the dimmest part of the intensity image. Thus, the time-delay autocorrelation is limited to $[0, 1]$. The time-delay autocorrelations for each cell were used to calculate the mean and standard deviation independently at each Δt. Intensity variability was defined as 1 minus the time-delay autocorrelation.

$c_n(\Delta t) = 1$ indicates complete stability of cortical actin dynamics over time, and this is therefore equivalent to variability equal to zero.

6.5.3 Statistics

Statistical analysis was performed with one-way ANOVA and the Tukey-Kramer test for multiple comparisons. P-values were subjected to a Bonferroni correction for multiple comparisons where necessary. P-values less than 0.05 were considered significant.

Chapter 7: Summary and Future Directions

7.1 Summary

Cells actively detect and respond to physical, chemical, and biological stimuli in extracellular environments. In this dissertation, I combined experimental data, image analysis, statistical models, and computational simulations to link the geometry, organization, and dynamics of intracellular signaling networks with cell function.

Activation mechanisms of effector T cells must be highly sensitive to biochemical cues to ensure a rapid immune response, but must also be self-regulating to prevent the deleterious consequences of immune-system autoreactivity. In Chapter 3, I explored the organization and geometry of Bcl10 self-assembly and degradation, which are key mediating steps in effector-T-cell activation and regulation. By using computational image-analysis tools to quantify Bcl10-filament lengths and Bcl10-autophagosome contacts, I demonstrated that Bcl10 filaments shortened over time and that autophagosomes were more likely to be attached to Bcl10-filament ends or Bcl10 puncta. To assess the statistical validity of these results, I introduced a novel bootstrap-like resampling method for image data and showed that the number of Bcl10-autophagosome contacts and their spatial distributions were

highly non random. To probe Bcl10 dynamics further, I developed a stochastic Monte Carlo simulation of nucleation-limited growth and degradation, and showed that tuning the simulations parameters modulated both the heterogeneity and character of the simulation outputs. The results of these studies demonstrated that the TCR-to-NF-κB signaling pathway exhibits characteristics of an excitable system, including a digital activation facilitated by Carma1 nucleation of Bcl10, and the coupled positive- and negative-feedback loops between Bcl10-filament growth, cell activation, and Bcl10 degradation.

Other cell functions also rely on physical and biochemical cues in the extracellular environment. During wound healing, cells in the immune system, such as neutrophils, become activated and migrate towards the site of wounds to detect and eliminate pathogens, and epithelial cells migrate in a collective fashion to close the wound. In Chapter 4, I explored the effect of nanotopographic ridged substrates on cytoskeletal dynamics in both neutrophil-like HL60 and epithelial MCF10A. Nanotopographies such as collagen fibers are ubiquitous *in vivo*. To explore the dynamic behavior of the cytoskeleton on and off the nanotopographies, I developed an image-analysis suite based on optical flow. Using the raw, pixel-based optical-flow-direction distributions, I systematically measured the influence of nanoridges on cytoskeletal dynamics and showed that nanoridges bias waves of cytoskeletal polymerization in both cell types. To parameterize these distributions, I designed a statistical bimodal-von-Mises model and showed that both immune cells and epithelial cells were similarly affected by ridged substrates despite having different migratory modes and phenotypes (epithelial vs. amoeboid). To quantify the influence of ridges on the

micron scale, I clustered and tracked similarly-oriented optical-flow vectors. Using optical-flow-cluster tracking, I showed that the speed of actin polymerization waves were unchanged on and off ridges.

Although I demonstrated that nanotopographic ridges bias cytoskeletal dynamics, the mechanisms that facilitate this bias are not completely understood. In Chapter 5, I utilized the optical-flow-analysis suite introduced in Chapter 4 to probe the interaction between textures and the cytoskeleton via the use of differently spaced nanoridges and *Dictyostelium discoideum*. In Dicty, I showed that ridges of narrow spacings biased the direction of actin-wave polymerization along the ridges, but that actin-wave speeds were unaffected by ridge spacing. Motivated by recent experimental data which showed that curvature promotes actin nucleation [15,16], I showed that evenly spaced ridge-like patterns of upregulated nucleation-promoting-factor activity are sufficient to generate biased actin waves in the ridge direction. Interestingly, upregulating NPF activity on ridges coupled with a downregulation of NPF activity off ridges produced better actin-wave guidance than upregulation alone, which suggests that a redistribution of NPFs rather than enhancement is responsible for topography-induced guidance. Remarkably, the actin-wave speeds in the experiments and simulations were similar despite simulation parameters being developed under different experimental conditions. Lastly, although full quantitative agreement wasn't achieved, the simulations also provided additional measurements of actin-filament length that would not be possible to measure experimentally. Taken together, robust quantification with optical-flow-based analyses and guided actin waves on nanotopographic ridges provided a robust framework for probing the

mechanisms of texture sensing and contact guidance.

The tools and techniques that I developed can also be applied to detect and quantify dynamics *in vivo*. In Chapter 6, I shared an *in vivo* application for measurements of self-assembly and disassembly and how they can provide deep insight into cell behavior. I used a modified cell-shape-analysis framework [29, 185] to measure the dynamics of actin waves before, during, and after the epithelial-to-mesenchymal transition in cancer metastasis. I showed that mesenchymal cancer cells exhibited distinguishable dynamic hallmarks: rapid periods of actin activity in seemingly random locations around the cell periphery and large but short-lived protrusions around 2 μm in size. Interestingly, cells which were on the leading edge of a tumor exhibited a mix of both hallmarks, which indicated that cells with mesenchymal-like qualities either tended to migrate towards the edge of the tumor, or that the epithelial-to-mesenchymal transition led to more variable and dynamic cytoskeletal activity.

In sum, the work presented in this dissertation introduced ways that an excitable systems framework and quantification of the organization and dynamics of signaling-network components can provide deep, phenomenological, and quantitative insights into variety of biological systems.

7.2 Future Directions

7.2.1 Extracting Biological Information from Waves and Oscillations

The actin-polymerization dynamics studied in Chapters 4, 5, and 6 all demonstrated that amorphous concentration fields of actin encode biological information in the form of waves and oscillations. In each chapter, I presented computational techniques to measure the dynamic behavior of actin, and connected these measurements to cell behavior. One recurring technique that I used was optical flow. Here, I expand upon the future directions of optical-flow-based analysis techniques and suggest other applications for their use.

In Chapters 4 and 5, I showed that optical flow uses image gradients to measure the dynamics of actin in a time series of images. In both chapters, I parameterized the distribution of optical-flow directions, however, the fhe fit parameters that were analyzed in Chapters 4 and 5 were derived from accumulated-over-time data. Thus, the fit parameters did not include how actin, and overall cell behavior, might be changing in time. One way to expanding the capabilities of the optical-flow analysis is to fit the direction distributions for each frame in the time series independently (or moving window of frames in a given time interval). This over-time extension of the current analysis technique can provide insight into how a system dynamically responds to a static or changing environment. Due to the piecewise nature of such an analysis, the over-time behavior of model parameters will need to be interpreted carefully and/or fit to their own time-series model.

In independently fitting the von-Mises model in a frame-by-frame manner, the model can also be adapted to parameterize directly the time-series behavior of optical-flow distributions. The model, which for a single distribution of optical-flow directions (i.e., without considering time) is shown in Equation 4.5.5, can be augmented via substitutions for each of the model parameters of the form $\kappa = \kappa(t) = \sum_i f_i(t, \vec{\alpha}_i)$. The set of functions $f(t, \vec{\alpha})$ can be simple (e.g., $at + b$) or complex (e.g., terms of a Fourier series). Each of the other parameters, including θ, p_1, p_2, and p_3 would undergo a similar transformation with their own set of functions and parameters. Under such a substitution, the components of $\vec{\alpha}$ would vary to maximize the likelihood function, and optimum values for the components of $\vec{\alpha}$ will produce over-time functions for the interpretable von-Mises-model parameters. Notably, such a model can also include nonlinear functions such as Heaviside functions, which could parameterize discrete switches in external environments, such as a switching electric field.

Building statistical models of optical-flow direction distributions can also provide insight into coarse-grained behavior within flow fields. As described previously, the Lucas-Kanade optical-flow method utilizes a window of predetermined size, and it is crucial that the span of the window is within the confines of the desired region. Once optical flow is calculated, optical-flow modeling can also be performed in a coarse-grain manner whereby the optical-flow directions in a moving-N-$\times$-N window are independently fit to some chosen model (e.g., von Mises distribution plus a constant offset). Upon such a calculation, the model-parameter field (e.g., field of κ, p_1, etc.) would contain information about coarse-grained uniformity or randomness

in the flow field. Such an advancement could augment, or be combined with, optical-flow-based-detection algorithms [192] to provide additional information about the motion of discrete objects in images.

Optical flow can also be used to connect, correlate, or causally relate dynamics that occur in different spatial regions. In the actin-wave dynamics in HL60 or Dicty (in Chapters 4 and 5, respectively) correlation-length or correlation-time measurements could be performed on actin waves that evolve in statistically similar ways. These measurements could address questions of actin-wave persistence on and off ridges, the spatial distance over which actin waves are correlated on and off ridges, and the effect of different ridge spacings on actin-wave correlation over a fixed distance. Beyond bioimage analysis, correlation of optical flow across spatial distances can help identify structures moving in ways that optical flow cannot determine easily. For example, the Lucas-Kanade optical-flow solution cannot distinguish global circular motion (e.g., a rotating wheel). However, the spatial correlation of optical flow between any pair of coordinates in a circularly moving region would be constant (e.g., opposite sides of the wheel would be maximally anticorrelated). Thus, spatial correlations of optical flow can provide insights into the structure or spatial connection between moving objects in a field of view.

The use of optical flow also extends beyond single-channel analyses. Although the techniques used in Chapters 4, 5, and 6 were performed on images of actin, they can also be used to measure, and elucidate relationships between, other cytoskeletal proteins and signaling molecules. For example, waves of signaling molecules like PTEN, PIP3, and PI3K all play a role in actin dynamics [9], and the dynamic

relationships between actin and upstream signaling components control a variety of cell functions and behaviors [3,71]. Because the waves and oscillations in fluorescent images of signaling molecules can also be measured with optical flow and downstream optical-flow techniques, simultaneously analyzing actin alongside other signaling molecules can measure spatial and temporal relationships, and assess the role of biochemical dynamics in overall cell behavior.

In addition to the analysis of biological images, there are numerous industry applications for optical flow that are currently in development or use. For example, optical-flow-based methods are being used in autonomous vehicles to segment and extract discrete objects in the foreground and background of images in a time series [193], and optical flow is being combined with neural-network models to predict emotional states from facial expressions [194, 195].

Adapting the optical-flow-based algorithms developed for industry applications can provide new ways to analyze and interpret bioimage data. For example, one common set of bioimage challenges are related to microscope jitter and drift, whereby the stationary background of an image series moves in random or regular patterns. Using foreground-background separation techniques outlined in [193], which was developed to identify vehicles, pedestrians, or other obstacles from a moving viewpoint, can help identify the true motion of cell that is being imaged in jittery conditions. Moreover, using optical-flow vectors (along with raw intensity) to train a convolutional-neural-network (CNN) can provide the network with additional information for training, and, ultimately, could yield better performance. Using training techniques similar to those outlined in [194, 195], which used optical

flow for the recognition of facial expressions, can allow for machine-learning models to classify images of WT versus perturbed cells, such as those in [9, 71].

One challenge in using optical-flow-based tools from industry (e.g., from autonomous vehicles [193]) is that industrial applications of optical flow often involve combining images, or a time series of images, from multiple viewing angles. The combination of two or more views of the same field allows for the deduction of 3-D motion [89,90] that cannot be measured directly in real-world conditions (i.e., mobile cameras often produce 2-D projections rather than 3-D volumetric scans). Realistic cell behaviors are not confined to two-dimensional planes (e.g., those seen in [196]), and, thus, require the analysis of 3-D motion. However, unlike industrial applications, advances in bioimaging technology have enabled isotropic, fast-frame-rate, 3-D imaging [197–200]. Despite such imaging advances, cutting-edge techniques on the analysis of 3-D objects is limited to the tracking and measurement of segmented volumes [201] and organization (shown in Chapter 3). Since optical flow relies on fast frame rates and accurate gradients, extending the optical-flow-based tools presented in this dissertation into 3-D can provide a substantial amount of new dynamic information and, ultimately, lead to new insights into 3-D biological behavior.

Extending optical flow to efficiently compute higher-dimensional motion is not trivial. For one, the eigenvalue problem for a 3×3 matrix is equivalent to finding the roots of a cubic polynomial, for which general solutions are complicated. Note that numerical solutions are slow and must be computed $ijkl$ times for a 3-D time series with dimension $i \times j \times k \times l$ where $i, j, k, l > 500$ is typical. Thus, hard-coded solutions are strongly preferred for efficient implementations.

One additional challenge lies in the Lucas-Kanade equations during the calculation of 3-D optical flow. During 3-D calculations, moving 3-D planes or two intersecting 3-D planes will produce low reliabilities [202]. Although such solutions are valid and realistic, the least-squares formulation of the Lucas-Kanade method will project all 3-D optical-flow calculations onto a 2-D plane, and the eigenvalue associated with the eigenvector normal to the plane will be small. Thus, all reliability measures must be carefully considered, and the traditional definition of reliability, the smallest eigenvalue of the structure tensor, may need to be redefined. One possible solution is to use the set of eigenvalues and eigenvectors of the structure tensor from the 3-D extension of Equation 2.6 to determine the high-reliability subspace of optical flow (i.e., the one- or two-dimensional eigenspace with large eigenvalues). Once the subspace is found, the structure tensor can be rotated such that one or two of the eigenvalues will be zero, and then optical-flow calculations can be repeated on the lower dimensional subspace.

If the challenges associated with 3-D optical flow are solved, then the extension of the optical-flow tools introduced in this dissertation can provide additional capabilities. One such capability is the 3-D extension of the von-Mises model. A 3-D von-Mises distribution would require two angles to parameterize the mean direction of flow, and theoretical calculations of the indistinguishable-from-uniform cutoff, which is $\kappa = 2$ in 2-D. Notably, there may even need to be two independent κ parameters that define the distribution widths in perpendicular directions. Fortunately, the clustering and tracking introduced in Chapter 4 could remain largely unchanged except to add an additional spatial dimension to the clustering kernel

in Equation 4.5.6, and to the tracking, which has already been implemented [131]. Notably, 3-D optical-flow clustering allows for the identification of similarly moving mesoscale structures in 3-D. In the context of bioimage analysis, optical-flow clustering can provide motion-based metrics to augment challenging tasks like object segmentation, which I will discuss at the end of Subsection 7.2.4.

7.2.2 Connecting Biological Excitability to Models and Simulations

As demonstrated in Chapters 3 and 5, models and simulations provide a way to probe the dynamics of a biological system that may not be able to be studied experimentally. In Chapter 3, I showed that different simulations parameters can alter the character and heterogeneity of outputs, and in Chapter 5, I showed that different configurations of biochemical-signaling components can be compared to and benchmarked against experimental data.

One simple, yet powerful, way to probe biological excitable-systems dynamics is through the use of forest-fire models. Although reaction-diffusion equations are not explicitly included in forest-fire models, the dynamic patterns observed exhibit many apparent similarities with observed reaction-diffusion systems [9, 71]. Such patterns include clearly-defined leading edges of a wave and slowly diffusing trailing edges, which in a forest-fire model is the growth of a tree in an empty region on the trailing edge.

With new understandings of the excitability of the actin signaling network [3, 9, 71], there are many ways in which a forest-fire model can be augmented to

be more biologically realistic. For example, one missing component is an inhibition signal/wave. Recapitulating a traveling wave in a forest-fire model minimally requires an activator (i.e., fire) and refractory period (i.e., regrowing of trees). However, experimental evidence and theoretical predictions suggest the existence of a mutual-inhibition-feedback loop between signaling molecules that promote versus inhibit actin polymerization [3, 9, 71, 158, 160]. The three primary challenges to incorporating an inhibition wave in a forest-fire model are: (1) determining the medium in which the inhibition wave travels (i.e., the fires travel on trees, so is there another set of trees for inhibition waves?); (2) determining the mechanisms by which inhibition waves are initiated; and (3) determining the result of the inhibition wave coming in contact with a tree and/or a fire. One possible way to incorporate inhibition of excitatory waves is through local excitation and global inhibition [203].

One drawback in the use of forest-fire models to recapitulate biological phenomena is the requirement that a fire will spread from neighboring pixels. During a cascade of actin-wave polymerization, there is no guarantee that polymerization will continue an additional step even if all biochemical components are in place. Thus, modifying a forest-fire model to facilitate more randomness in the spreading of fire can be accomplished with a spreading probability. Furthermore, inclusion of a spreading probability could allow a modified forest-fire model to recreate spatially patterned substrates. For example, because data suggest that biased actin-wave propagation on nanotopographic surfaces is facilitated by large-curvature regions [15, 16], the forest-fire substrate can upregulate the spreading parameter along equally-spaced stripes and leave it unchanged elsewhere. Alternatively, three-

dimensional forest-fire models could also be used to enable more complexities in the texture. In that case, such models could also incorporate the shapes of 3-D nanotopography in the simulations, such as sawteeth [24, 38].

Finally, exploring a large range of dynamic behavior in a forest fire could be accomplished via the inclusion of a cell membrane. Although it is unclear how the membrane will deform, and if/how there will be conservation of quantities such as cytosolic volume or surface area, solving these challenges could yield an easily implementable toy model for an excitable reaction-diffusion-like dynamic system that mimic aspects of cell behavior.

One alternative class of models that explicitly incorporate reaction-diffusion dynamics is phase-field models. Phase-field models were initially designed to capture the growth dynamics of crystals, but have recently been shown to capture cell-migration phenotypes accurately [73]. All suggested future directions for a forest-fire model could also be considered for a phase-field model. Notably, phase-field models implicitly include a cell membrane, and thus can incorporate additional membrane-dependent terms such as curvature and tension, albeit at a significantly greater computational cost (minutes-long phase-field simulations take hours to run on modern hardware).

An additional bonus is that a phase-field contains explicit polarity for separate coarse-grained regions through the simulated cell. This polarity could enable additional simulations in which external forces on the cell or intracellular component is directional, e.g. electric fields.

One important issue in both forest-fire and phase-field models is the analysis of

model outputs. Although the outputs are rich and dynamic, similar to image data, these outputs are difficult to quantify and analyze in a statistically robust way. Thus, the analysis techniques that were introduced in this dissertation can prove to be widely applicable in the analysis experimentally-derived and simulations-derived data.

7.2.3 Insights from the Spatial Organization of Biological Structures

Intracellular structures are organized into a wide range of shapes and sizes. In Chapter 3, I demonstrated how image-based bootstrap-like resampling is a powerful and generalizable way to determine whether a given arrangement of structures should be considered random or biased, e.g., preferentially co-localized with other structures. In essence, if measurements from an image are determined and image-based resampling is performed, a comparison of the measured and resampled distributions can determine whether the measurement results were a product of randomness.

In general, the bootstrap-like resampling of image structures can provide a baseline of what any type of spatial distribution would look like if the underlying driver of the distribution is uniformly random. Moreover, the random distribution of image structures can be augmented based on other distribution types, such as simple Gaussians or complex structure-based distributions based on other image features (e.g., Gaussians centered at the nearest objects in other imaging channels). Notably, the resampling can be augmented to such that only certain regions of the

space are eligible for placement of image structures, which could be particularly useful if there are restricted regions in the image. For example, in Chapter 3, I forced all random placements of autophagosomes to occur within the cell volume; one might also find it useful to exclude other biologically restricted regions, such as the cell nucleus.

7.2.4 Enhancement, Segmentation, and Skeletonization of 3-D Filaments, Planes, and Spheroids

The practice of segmenting three-dimensional objects with distinguishable geometric features is widely applicable in the image analysis of biological systems. Although sophisticated segmentation techniques can perform well on high-quality image data, such as those of Bcl10 and autophagosomes in Chapter 3 [201, 204], these algorithms can underperform when structures are not continuous or uniformly bright (e.g., similar to those seen in [205, 206] where segmentation and tracing were performed by hand).

One generalizable way to improve and enhance raw image data is through the use of carefully constructed filters, such as Laplacian-of-Gaussian (LoG) filters (Figure 7.1). In the case of a 2-D Laplacian and a 3-D Gaussian, the LoG filter takes the form of a cylinder (cylindrical LoG). Parameterized by radial and length parameters (Figure 7.1A), filamentous objects can be extracted from images by tuning the radius parameter to an appropriate value to match the size of the object of interest. Note, this tuning could be used to segment thick and thin filaments

separately by tuning the radius range. Furthermore, tuning can also be customized to match the unique shape of some biological structures, such as 3-way (shaped like a "T") or 4-way ("X") junctions. Ultimately, enhancing images can be achieved by taking a max projection through the newly introduced angular degrees of freedom (Figure 7.1B). As a representative example of this method, the data from [205, 206] were enhanced with LoG cylinders by identifying the argmax over all possible filter angles, segmented via empirically chosen thresholds, and then skeletonized (Figure 7.1C). The difference between automatically traced data and hand-traced data was small.

In addition to enhancing the image, carefully constructed filters that span a filter-parameter space can also be used to extract geometric information about the objects of interest. For example, in the case of the cylindrical Laplacian-of-Gaussian filters, the filter-parameter space consisted of angles θ and ϕ, which represented the orientation of the cylinder. Given an image I, and filter f, a filtered image J can be expressed as $J(x, y, z) = I(x, y, z) \otimes f(x, y, z|\theta, \phi)$. Thus, at a chosen voxel (x, y, z), if the filter spans an entire (θ, ϕ) subspace, the output will be a 2-D, θ vs. ϕ heatmap where the global maximum in the 2-D heatmap is located at the (θ, ϕ) coordinate that represents alignment with the structure centered around the (x, y, z) voxel (similar to the heatmap in Figure 7.1B). This process could be relevant to extracting angular information (i.e. the orientation of filaments or orientations normal to surfaces) or geometric information like the radii of filaments or thicknesses of membranes. However, the most impactful and powerful use of this method could be to generate medial-axis skeletons from grayscale images, which is an ongoing

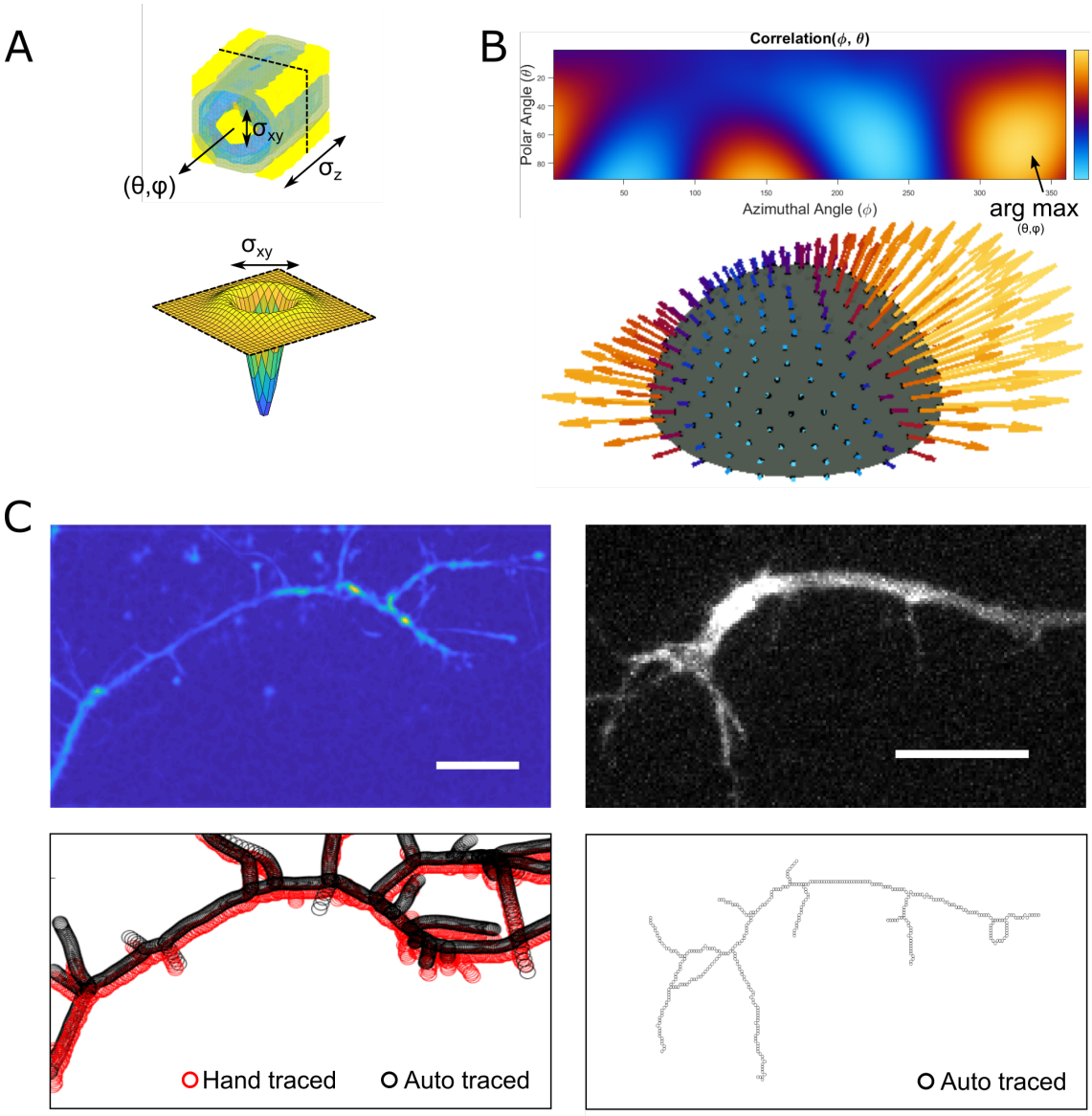

Figure 7.1: Using LoG cylinders to filter, segment, and trace filamentous objects. (A) A representative segment of a typical LoG cylinder and a xy cross section. The filter size is parameterized by radial and length parameters, σ_{xy} and σ_z. The orientation of the filter is parameterized by the polar and azimuthal angles, θ and ϕ. (B) (θ,ϕ) heatmap produced by filtering with the LoG cylinder in A at all angles in the space. The semi-sphere representation indicates direction of maximum correlation with image features. (C) Representative skeletonization from enhanced images using the LoG-cylinder filtering.

challenge with no clear general solution. In all cases, in addition to cylinders where $\nabla^2 = D_x^2 + D_y^2$, LoG filters could also be used to extract and measure planes or spheroids, where $\nabla^2 = D_x^2$ or $D_x^2 + D_y^2 + D_z^2$, respectively. The robustness of this scheme can be widely applied to the analysis of 3-D volumes of sparse or densely packed filament networks, such as axons and dendritic spines.

Enhancement of 2-D and 3-D structures can also be used as a preprocessing step before calculating optical flow. In estimating the optical flow of a discrete object, enhancing the object via carefully constructed filters can increase the accuracy and continuity of image gradients, and, thus, make the optical-flow calculation more robust. Furthermore, the mesoscale clustering described in Chapter 4 and Subsection 7.2.2 can also be combined with spatial information from Laplacian-of-Gaussian filtering to ensure that optical-flow vectors and mesoscale clusters are properly contained with the object volume.

Bibliography

[1] Peter N Devreotes and Sally H Zigmond. Chemotaxis in eukaryotic cells: a focus on leukocytes and dictyostelium. *Annual review of cell biology*, 4(1):649–686, 1988.

[2] Tim Lmmermann, Philippe V. Afonso, Bastian R. Angermann, Ji Ming Wang, Wolfgang Kastenmller, Carole A. Parent, and Ronald N. Germain. Neutrophil swarms require LTB4 and integrins at sites of cell death in vivo. *Nature*, 498(7454):371–375, June 2013.

[3] Peter N. Devreotes, Sayak Bhattacharya, Marc Edwards, Pablo A. Iglesias, Thomas Lampert, and Yuchuan Miao. Excitable Signal Transduction Networks in Directed Cell Migration. *Annual Review of Cell and Developmental Biology*, 33(1):103–125, 2017.

[4] Min Zhao. Electrical fields in wound healingAn overriding signal that directs cell migration. *Seminars in Cell & Developmental Biology*, 20(6):674–682, August 2009.

[5] Zhengyu Ma, Gina G. Turrigiano, Ralf Wessel, and Keith B. Hengen. Cortical Circuit Dynamics Are Homeostatically Tuned to Criticality InVivo. *Neuron*, 104(4):655–664.e4, November 2019.

[6] RachelM Lee, Leonard Campanello, MattJ Hourwitz, Phillip Alvarez, Ava Omidvar, JohnT Fourkas, and Wolfgang Losert. Quantifying topography-guided actin dynamics across scales using optical flow. *Molecular Biology of the Cell*, pages mbc.E19–11–0614, February 2020. Publisher: American Society for Cell Biology (mboc).

[7] Jeremy S. Rossman, Natalia G. Stoicheva, Felicia D. Langel, George H. Patterson, Jennifer Lippincott-Schwartz, and Brian C. Schaefer. POLKADOTS Are Foci of Functional Interactions in T-Cell Receptormediated Signaling to NF-B. *Molecular Biology of the Cell*, 17(5):2166–2176, May 2006.

[8] Liron David, Yang Li, Jun Ma, Ethan Garner, Xinzheng Zhang, and Hao Wu. Assembly mechanism of the CARMA1BCL10MALT1TRAF6 signalosome. *Proceedings of the National Academy of Sciences*, page 201721967, January 2018.

[9] Yuchuan Miao, Sayak Bhattacharya, Marc Edwards, Huaqing Cai, Takanari Inoue, Pablo A. Iglesias, and Peter N. Devreotes. Altering the threshold of an excitable signal transduction network changes cell migratory modes. *Nature Cell Biology*, 19(4):329–340, April 2017.

[10] Luca Cardamone, Alessandro Laio, Vincent Torre, Rajesh Shahapure, and Antonio DeSimone. Cytoskeletal actin networks in motile cells are critically self-organized systems synchronized by mechanical interactions. *Proceedings of the National Academy of Sciences*, 108(34):13978–13983, August 2011.

[11] James E. Komianos and Garegin A. Papoian. Stochastic Ratcheting on a Funneled Energy Landscape Is Necessary for Highly Efficient Contractility of Actomyosin Force Dipoles. *Physical Review X*, 8(2):021006, April 2018. Publisher: American Physical Society.

[12] Elliot Dine, Agnieszka A. Gil, Giselle Uribe, Clifford P. Brangwynne, and Jared E. Toettcher. Protein Phase Separation Provides Long-Term Memory of Transient Spatial Stimuli. *Cell Systems*, 6(6):655–663.e5, June 2018.

[13] Osame Kinouchi and Mauro Copelli. Optimal dynamical range of excitable networks at criticality. *Nature Physics*, 2(5):348–351, May 2006.

[14] Loling Song, Sharvari M. Nadkarni, Hendrik U. Bdeker, Carsten Beta, Albert Bae, Carl Franck, Wouter-Jan Rappel, William F. Loomis, and Eberhard Bodenschatz. Dictyostelium discoideum chemotaxis: Threshold for directed motion. *European Journal of Cell Biology*, 85(9):981–989, September 2006.

[15] Viviana I. Risca, Evan B. Wang, Ovijit Chaudhuri, Jia Jun Chia, Phillip L. Geissler, and Daniel A. Fletcher. Actin filament curvature biases branching direction. *Proceedings of the National Academy of Sciences of the United States of America*, 109(8):2913–2918, February 2012.

[16] Hsin-Ya Lou, Wenting Zhao, Xiao Li, Liting Duan, Alexander Powers, Matthew Akamatsu, Francesca Santoro, Allister F. McGuire, Yi Cui, David G. Drubin, and Bianxiao Cui. Membrane curvature underlies actin reorganization in response to nanoscale surface topography. *Proceedings of the National Academy of Sciences of the United States of America*, 116(46):23143–23151, November 2019.

[17] Douglas J. Blackiston, Kelly A. McLaughlin, and Michael Levin. Bioelectric controls of cell proliferation: Ion channels, membrane voltage and the cell cycle. *Cell Cycle*, 8(21):3527–3536, November 2009. Publisher: Taylor & Francis _eprint: https://doi.org/10.4161/cc.8.21.9888.

[18] Maria Manuela Rosado, Myrtill Simk, Mats-Olof Mattsson, and Claudio Pioli. Immune-Modulating Perspectives for Low Frequency Electromagnetic Fields in Innate Immunity. *Frontiers in Public Health*, 6, 2018. Publisher: Frontiers.

[19] S. Clar, K. Schenk, and F. Schwabl. Phase transitions in a forest-fire model. *Physical Review E*, 55(3):2174–2183, March 1997. Publisher: American Physical Society.

[20] Krzysztof Krawczyk, Shuai Xue, Peter Buchmann, Ghislaine Charpin-El-Hamri, Pratik Saxena, Marie-Didie Hussherr, Jiawei Shao, Haifeng Ye, Mingqi Xie, and Martin Fussenegger. Electrogenetic cellular insulin release for real-time glycemic control in type 1 diabetic mice. *Science*, 368(6494):993–1001, May 2020. Publisher: American Association for the Advancement of Science Section: Research Article.

[21] Bagher Farhood, Masoud Najafi, and Keywan Mortezaee. CD8+ cytotoxic T lymphocytes in cancer immunotherapy: A review. *Journal of Cellular Physiology*, 234(6):8509–8521, 2019. _eprint: https://onlinelibrary.wiley.com/doi/pdf/10.1002/jcp.27782.

[22] Deok-Ho Kim, Paolo P. Provenzano, Chris L. Smith, and Andre Levchenko. Matrix nanotopography as a regulator of cell function. *Journal of Cell Biology*, 197(3):351–360, April 2012. Publisher: The Rockefeller University Press.

[23] Sumona Sarkar. Roles of Nanofiber Scaffold Structure and Chemistry in Directing Human Bone Marrow Stromal Cell Response. *Advances in Tissue Engineering & Regenerative Medicine: Open Access*, 1(1), August 2016.

[24] Song Chen, Matt J. Hourwitz, Leonard Campanello, John T. Fourkas, Wolfgang Losert, and Carole A. Parent. Actin Cytoskeleton and Focal Adhesions Regulate the Biased Migration of Breast Cancer Cells on Nanoscale Asymmetric Sawteeth. *ACS Nano*, 13(2):1454–1468, February 2019. Publisher: American Chemical Society.

[25] Lara M. Kingeter and Brian C. Schaefer. Loss of Protein Kinase C, Bcl10, or Malt1 Selectively Impairs Proliferation and NF-B Activation in the CD4+ T Cell Subset. *The Journal of Immunology*, 181(9):6244–6254, November 2008.

[26] Edward Judokusumo, Erdem Tabdanov, Sudha Kumari, MichaelL. Dustin, and LanceC. Kam. Mechanosensing in T Lymphocyte Activation. *Biophysical Journal*, 102(2):L5–L7, January 2012.

[27] King Lam Hui, Sae In Kwak, and Arpita Upadhyaya. Adhesion-dependent modulation of actin dynamics in Jurkat T cells. *Cytoskeleton*, 71(2):119–135, 2014.

[28] Desu Chen, Sumona Sarkar, Julin Candia, Stephen J. Florczyk, Subhadip Bodhak, Meghan K. Driscoll, Carl G. Simon, Joy P. Dunkers, and Wolfgang Losert. Machine learning based methodology to identify cell shape phenotypes associated with microenvironmental cues. *Biomaterials*, 104:104–118, October 2016.

[29] Meghan K. Driscoll, Xiaoyu Sun, Can Guven, John T. Fourkas, and Wolfgang Losert. Cellular Contact Guidance through Dynamic Sensing of Nanotopography. *ACS Nano*, 8(4):3546–3555, April 2014.

[30] Henry Y. Lu, Bradly M. Bauman, Swadhinya Arjunaraja, Batsukh Dorjbal, Joshua D. Milner, Andrew L. Snow, and Stuart E. Turvey. The CBM-opathies-A Rapidly Expanding Spectrum of Human Inborn Errors of Immunity Caused by Mutations in the CARD11-BCL10-MALT1 Complex. *Frontiers in Immunology*, 9:2078, 2018.

[31] Swadhinya Arjunaraja and Andrew L. Snow. Gain-of-function mutations and immunodeficiency: at a loss for proper tuning of lymphocyte signaling. *Current Opinion in Allergy and Clinical Immunology*, 15(6):533–538, December 2015.

[32] M. Paciolla, A. Pescatore, M. I. Conte, E. Esposito, M. Incoronato, M. B. Lioi, F. Fusco, and M. V. Ursini. Rare mendelian primary immunodeficiency diseases associated with impaired NF-B signaling. *Genes and Immunity*, 16(4):239–246, June 2015.

[33] Klaus-Michael Debatin. Apoptosis pathways in cancer and cancer therapy. *Cancer Immunology, Immunotherapy*, 53(3):153–159, March 2004.

[34] Felicity D. Herrington, Ruaidhr J. Carmody, and Carl S. Goodyear. Modulation of NF-B Signaling as a Therapeutic Target in Autoimmunity. *Journal of Biomolecular Screening*, 21(3):223–242, March 2016.

[35] Shao-Cong Sun, Jae-Hoon Chang, and Jin Jin. Regulation of NF-B in Autoimmunity. *Trends in immunology*, 34(6):282–289, June 2013.

[36] Suman Paul, AnujK. Kashyap, Wei Jia, You-Wen He, and BrianC. Schaefer. Selective Autophagy of the Adaptor Protein Bcl10 Modulates T Cell Receptor Activation of NF-B. *Immunity*, 36(6):947–958, June 2012.

[37] Suman Paul and Brian C. Schaefer. A new look at T cell receptor signaling to nuclear factor-B. *Trends in Immunology*, 34(6):269–281, June 2013.

[38] Xiaoyu Sun, Meghan K. Driscoll, Can Guven, Satarupa Das, Carole A. Parent, John T. Fourkas, and Wolfgang Losert. Asymmetric nanotopography biases cytoskeletal dynamics and promotes unidirectional cell guidance. *Proceedings of the National Academy of Sciences*, 112(41):12557–12562, October 2015.

[39] Christina M. Ketchum, Xiaoyu Sun, Alexandra Suberi, John T. Fourkas, Wenxia Song, and Arpita Upadhyaya. Subcellular topography modulates actin dynamics and signaling in B-cells. *Molecular Biology of the Cell*, 29(14):1732–1742, May 2018.

[40] King Lam Hui and Arpita Upadhyaya. Dynamic microtubules regulate cellular contractility during T-cell activation. *Proceedings of the National Academy of Sciences*, 114(21):E4175–E4183, May 2017. Publisher: National Academy of Sciences Section: PNAS Plus.

[41] Anders E. Carlsson. Dendritic Actin Filament Nucleation Causes Traveling Waves and Patches. *Physical Review Letters*, 104(22):228102, June 2010.

[42] B. Lindner, J. Garca-Ojalvo, A. Neiman, and L. Schimansky-Geier. Effects of noise in excitable systems. *Physics Reports*, 392(6):321–424, March 2004.

[43] J. Nagumo, S. Arimoto, and S. Yoshizawa. An Active Pulse Transmission Line Simulating Nerve Axon. *Proceedings of the IRE*, 50(10):2061–2070, October 1962. Conference Name: Proceedings of the IRE.

[44] Per Bak, Chao Tang, and Kurt Wiesenfeld. Self-organized criticality: An explanation of the 1/f noise. *Physical Review Letters*, 59(4):381–384, July 1987. Publisher: American Physical Society.

[45] B. Drossel and F. Schwabl. Self-organized critical forest-fire model. *Physical Review Letters*, 69(11):1629–1632, September 1992. Publisher: American Physical Society.

[46] Karin E. de Visser, Alexandra Eichten, and Lisa M. Coussens. Paradoxical roles of the immune system during cancer development. *Nature Reviews Cancer*, 6(1):24–37, January 2006.

[47] Ira Mellman, George Coukos, and Glenn Dranoff. Cancer immunotherapy comes of age. *Nature*, 480(7378):480–489, December 2011.

[48] Rachel S. Riley, Carl H. June, Robert Langer, and Michael J. Mitchell. Delivery technologies for cancer immunotherapy. *Nature Reviews Drug Discovery*, 18(3):175–196, March 2019.

[49] Hannah Garner and Karin E. de Visser. Immune crosstalk in cancer progression and metastatic spread: a complex conversation. *Nature Reviews Immunology*, pages 1–15, February 2020. Publisher: Nature Publishing Group.

[50] Argyrios N. Theofilopoulos, Dwight H. Kono, and Roberto Baccala. The multiple pathways to autoimmunity. *Nature Immunology*, 18(7):716–724, July 2017. Number: 7 Publisher: Nature Publishing Group.

[51] Mark Larch and David C. Wraith. Peptide-based therapeutic vaccines for allergic and autoimmune diseases. *Nature Medicine*, 11(4):S69–S76, April 2005.

[52] David Wraith. Antigen-specific immunotherapy. *Nature*, 530(7591):422–423, February 2016.

[53] Juan-Manuel Anaya, Carolina Duarte-Rey, Juan C. Sarmiento-Monroy, David Bardey, John Castiblanco, and Adriana Rojas-Villarraga. Personalized medicine. Closing the gap between knowledge and clinical practice. *Autoimmunity Reviews*, 15(8):833–842, August 2016.

[54] David A. Horwitz, Tarek M. Fahmy, Ciriaco A. Piccirillo, and Antonio La Cava. Rebalancing Immune Homeostasis to Treat Autoimmune Diseases. *Trends in Immunology*, 40(10):888–908, October 2019.

[55] Mamatha Serasanambati and Shanmuga Reddy Chilakapati. Function of Nuclear Factor Kappa B (NF-kB) in Human Diseases-A Review. *South Indian Journal of Biological Sciences*, 2(4):368, October 2016.

[56] Torben Gehring, Thomas Seeholzer, and Daniel Krappmann. BCL10 Bridging CARDs to Immune Activation. *Frontiers in Immunology*, 9, 2018.

[57] Chuan-Jin Wu and Jonathan D. Ashwell. NEMO recognition of ubiquitinated Bcl10 is required for T cell receptor-mediated NF-B activation. *Proceedings of the National Academy of Sciences*, 105(8):3023–3028, February 2008.

[58] Erika Scharschmidt, Elmar Wegener, Vigo Heissmeyer, Anjana Rao, and Daniel Krappmann. Degradation of Bcl10 induced by T-cell activation negatively regulates NF-kappa B signaling. *Molecular and Cellular Biology*, 24(9):3860–3873, May 2004.

[59] Shimin Hu, Ming-Qing Du, Sun-Mi Park, Allison Alcivar, Like Qu, Sanjeev Gupta, Jun Tang, Mathijs Baens, Hongtao Ye, Tae H. Lee, Peter Marynen, James L. Riley, and Xiaolu Yang. cIAP2 is a ubiquitin protein ligase for BCL10 and is dysregulated in mucosa-associated lymphoid tissue lymphomas. *The Journal of Clinical Investigation*, 116(1):174–181, January 2006.

[60] Hu Zeng, Lie Di, Guoping Fu, Yuhong Chen, Xiang Gao, Langlai Xu, Xin Lin, and Renren Wen. Phosphorylation of Bcl10 Negatively Regulates T-Cell Receptor-Mediated NF-B Activation. *Molecular and Cellular Biology*, 27(14):5235–5245, July 2007.

[61] Camille Lobry, Tatiana Lopez, Alain Isral, and Robert Weil. Negative feedback loop in T cell activation through IB kinase-induced phosphorylation and degradation of Bcl10. *Proceedings of the National Academy of Sciences*, 104(3):908–913, January 2007.

[62] Qi Qiao, Chenghua Yang, Chao Zheng, Lorena Fontn, Liron David, Xiong Yu, Clay Bracken, Monica Rosen, Ari Melnick, Edward H. Egelman, and Hao Wu. Structural Architecture of the CARMA1/Bcl10/MALT1 Signalosome: Nucleation-Induced Filamentous Assembly. *Molecular cell*, 51(6):766–779, September 2013.

[63] A. G. Uren, K. O'Rourke, L. A. Aravind, M. T. Pisabarro, S. Seshagiri, E. V. Koonin, and V. M. Dixit. Identification of paracaspases and metacaspases: two ancient families of caspase-like proteins, one of which plays a key role in MALT lymphoma. *Molecular Cell*, 6(4):961–967, October 2000.

[64] Florian Schlauderer, Thomas Seeholzer, Ambroise Desfosses, Torben Gehring, Mike Strauss, Karl-Peter Hopfner, Irina Gutsche, Daniel Krappmann, and Katja Lammens. Molecular architecture and regulation of BCL10-MALT1 filaments. *Nature Communications*, 9(1):4041, October 2018.

[65] Margot Thome, Jean Enno Charton, Christiane Pelzer, and Stephan Hailfinger. Antigen Receptor Signaling to NF-B via CARMA1, BCL10, and MALT1. *Cold Spring Harbor Perspectives in Biology*, 2(9):a003004, September 2010.

[66] King Lam Hui, Lakshmi Balagopalan, Lawrence E. Samelson, and Arpita Upadhyaya. Cytoskeletal forces during signaling activation in Jurkat T-cells. *Molecular Biology of the Cell*, 26(4):685–695, December 2014.

[67] Visar Ajeti, A. Pasha Tabatabai, Andrew J. Fleszar, Michael F. Staddon, Daniel S. Seara, Cristian Suarez, M. Sulaiman Yousafzai, Dapeng Bi, David R. Kovar, Shiladitya Banerjee, and Michael P. Murrell. Wound healing coordinates actin architectures to regulate mechanical work. *Nature Physics*, 15(7):696–705, July 2019. Number: 7 Publisher: Nature Publishing Group.

[68] Venkat Maruthamuthu, Yvonne Aratyn-Schaus, and Margaret L Gardel. Conserved F-actin dynamics and force transmission at cell adhesions. *Current Opinion in Cell Biology*, 22(5):583–588, October 2010.

[69] Kristen F. Swaney, Chuan-Hsiang Huang, and Peter N. Devreotes. Eukaryotic Chemotaxis: A Network of Signaling Pathways Controls Motility, Directional Sensing, and Polarity. *Annual Review of Biophysics*, 39(1):265–289, April 2010. Publisher: Annual Reviews.

[70] Luiza Stankevicins, Nicolas Ecker, Emmanuel Terriac, Paolo Maiuri, Rouven Schoppmeyer, Pablo Vargas, Ana-Maria Lennon-Dumnil, Matthieu Piel, Bin Qu, Markus Hoth, Karsten Kruse, and Franziska Lautenschlger. Deterministic actin waves as generators of cell polarization cues. *Proceedings of the National Academy of Sciences*, 117(2):826–835, January 2020. Publisher: National Academy of Sciences Section: PNAS Plus.

[71] Yuchuan Miao, Sayak Bhattacharya, Tatsat Banerjee, Bedri AbubakerSharif, Yu Long, Takanari Inoue, Pablo A Iglesias, and Peter N Devreotes. Wave patterns organize cellular protrusions and control cortical dynamics. *Molecular Systems Biology*, 15(3), March 2019.

[72] Paolo Maiuri, Jean-Franois Rupprecht, Stefan Wieser, Verena Ruprecht, Olivier Bnichou, Nicolas Carpi, Mathieu Coppey, Simon DeBeco, Nir Gov, Carl-Philipp Heisenberg, Carolina LageCrespo, Franziska Lautenschlaeger,

Mal LeBerre, Ana-Maria Lennon-Dumenil, Matthew Raab, Hawa-Racine Thiam, Matthieu Piel, Michael Sixt, and Raphal Voituriez. Actin Flows Mediate a Universal Coupling between Cell Speed and Cell Persistence. *Cell*, 161(2):374–386, April 2015.

[73] Falko Ziebert and Igor S. Aranson. Computational approaches to substrate-based cell motility. *npj Computational Materials*, 2(1):1–16, July 2016. Number: 1 Publisher: Nature Publishing Group.

[74] Aravind Chandrasekaran, Arpita Upadhyaya, and Garegin A. Papoian. Remarkable structural transformations of actin bundles are driven by their initial polarity, motor activity, crosslinking, and filament treadmilling. *PLOS Computational Biology*, 15(7):e1007156, July 2019. Publisher: Public Library of Science.

[75] David G. Spiller, Christopher D. Wood, David A. Rand, and Michael R. H. White. Measurement of single-cell dynamics. *Nature*, 465(7299):736–745, June 2010.

[76] A. Ponti, M. Machacek, S. L. Gupton, C. M. Waterman-Storer, and G. Danuser. Two Distinct Actin Networks Drive the Protrusion of Migrating Cells. *Science*, 305(5691):1782–1786, September 2004.

[77] Chenlu Wang, Sagar Chowdhury, Meghan Driscoll, Carole A. Parent, S. K. Gupta, and Wolfgang Losert. The interplay of cellcell and cellsubstrate adhesion in collective cell migration. *Journal of The Royal Society Interface*, 11(100):20140684, November 2014.

[78] Rachel M. Lee, Douglas H. Kelley, Kerstin N. Nordstrom, Nicholas T. Ouellette, and Wolfgang Losert. Quantifying stretching and rearrangement in epithelial sheet migration. *New Journal of Physics*, 15(2):025036, February 2013.

[79] R. M. Lee, C. H. Stuelten, C. A. Parent, and W. Losert. Collective cell migration over long time scales reveals distinct phenotypes. *Convergent Science Physical Oncology*, 2(2):025001, May 2016.

[80] Douglas H. Kelley and Nicholas T. Ouellette. Emergent dynamics of laboratory insect swarms. *Scientific Reports*, 3, January 2013.

[81] Deborah Hemingway. A BIOPHYSICAL PERSPECTIVE ON COLLECTIVE CELL MIGRATION AND MATHEMATICAL MODELING IN PHYSICS FOR THE LIFE SCIENCES. 2018. Accepted: 2019-02-08T06:33:10Z.

[82] Michael Murrell and Margaret L. Gardel. Actomyosin sliding is attenuated in contractile biomimetic cortices. *Molecular Biology of the Cell*, 25(12):1845–1853, June 2014.

[83] Benedict Hebert, Santiago Costantino, and Paul W. Wiseman. Spatiotemporal Image Correlation Spectroscopy (STICS) Theory, Verification, and Application to Protein Velocity Mapping in Living CHO Cells. *Biophysical Journal*, 88(5):3601–3614, May 2005.

[84] DhruvK. Vig, AlexE. Hamby, and CharlesW. Wolgemuth. On the Quantification of Cellular Velocity Fields. *Biophysical Journal*, 110(7):1469–1475, April 2016.

[85] Wei-Chiu Ma, Shenlong Wang, Rui Hu, Yuwen Xiong, and Raquel Urtasun. Deep Rigid Instance Scene Flow. pages 3614–3622, 2019.

[86] S L Happy and Aurobinda Routray. Fuzzy Histogram of Optical Flow Orientations for Micro-Expression Recognition. *IEEE Transactions on Affective Computing*, 10(3):394–406, July 2019. Conference Name: IEEE Transactions on Affective Computing.

[87] Berthold K. P. Horn and Brian G. Schunck. Determining optical flow. *Artificial Intelligence*, 17(1):185–203, August 1981.

[88] Andrs Bruhn, Joachim Weickert, and Christoph Schnrr. Lucas/Kanade Meets Horn/Schunck: Combining Local and Global Optic Flow Methods. *International Journal of Computer Vision*, 61(3):211–231, February 2005.

[89] Bruce D. Lucas and Takeo Kanade. An Iterative Image Registration Technique with an Application to Stereo Vision. In *Proceedings of the 7th International Joint Conference on Artificial Intelligence - Volume 2*, IJCAI'81, pages 674–679, San Francisco, CA, USA, 1981. Morgan Kaufmann Publishers Inc.

[90] E.P. Simoncelli, E.H. Adelson, and D.J. Heeger. Probability distributions of optical flow. In *Proceedings. 1991 IEEE Computer Society Conference on Computer Vision and Pattern Recognition*, pages 310–315, Maui, HI, USA, 1991. IEEE Comput. Sco. Press.

[91] Leonard Campanello, Maria K. Traver, Hari Shroff, Brian C. Schaefer, and Wolfgang Losert. Signaling through polymerization and degradation: Analysis and simulations of T cell activation mediated by Bcl10. *bioRxiv*, page 2020.05.28.120907, May 2020. Publisher: Cold Spring Harbor Laboratory Section: New Results.

[92] T. D. Gilmore. Introduction to NF-B: players, pathways, perspectives. *Oncogene*, 25(51):6680–6684, October 2006.

[93] Andrea Oeckinghaus and Sankar Ghosh. The NF-kappaB family of transcription factors and its regulation. *Cold Spring Harbor Perspectives in Biology*, 1(4):a000034, October 2009.

[94] Neil D. Perkins. Integrating cell-signalling pathways with NF-B and IKK function. *Nature Reviews Molecular Cell Biology*, 8(1):49–62, January 2007.

[95] Suman Paul, Maria K. Traver, Anuj K. Kashyap, Michael A. Washington, Joseph R. Latoche, and Brian C. Schaefer. T Cell Receptor Signals to NF-B Are Transmitted by a Cytosolic p62-Bcl10-Malt1-IKK Signalosome. *Sci. Signal.*, 7(325):ra45–ra45, May 2014.

[96] Jrgen Ruland and Lara Hartjes. CARDBCL-10MALT1 signalling in protective and pathological immunity. *Nature Reviews Immunology*, 19(2):118–134, February 2019.

[97] Karmel A. Allison, Eniko Sajti, Jana G. Collier, David Gosselin, Ty Dale Troutman, Erica L. Stone, Stephen M. Hedrick, and Christopher K. Glass. Affinity and dose of TCR engagement yield proportional enhancer and gene activity in CD4+ T cells. *eLife*, 5, 2016.

[98] Grgoire Altan-Bonnet and Ronald N. Germain. Modeling T cell antigen discrimination based on feedback control of digital ERK responses. *PLoS biology*, 3(11):e356, November 2005.

[99] Irena Stefanov, Bernhard Hemmer, Marco Vergelli, Roland Martin, William E. Biddison, and Ronald N. Germain. TCR ligand discrimination is enforced by competing ERK positive and SHP-1 negative feedback pathways. *Nature Immunology*, 4(3):248–254, March 2003.

[100] Jayajit Das, Mary Ho, Julie Zikherman, Christopher Govern, Ming Yang, Arthur Weiss, Arup K. Chakraborty, and Jeroen P. Roose. Digital Signaling and Hysteresis Characterize Ras Activation in Lymphoid Cells. *Cell*, 136(2):337–351, January 2009. Publisher: Elsevier.

[101] Mara N. Navarro, Carmen Feijoo-Carnero, Alba Gonzalez Arandilla, Matthias Trost, and Doreen A. Cantrell. Protein kinase D2 is a digital amplifier of T cell receptor-stimulated diacylglycerol signaling in nave CD8 T cells. *Science Signaling*, 7(348):ra99, October 2014.

[102] Jun Huang, Mario Brameshuber, Xun Zeng, Jianming Xie, Qi-jing Li, Yueh-hsiu Chien, Salvatore Valitutti, and Mark M. Davis. A single peptide-major histocompatibility complex ligand triggers digital cytokine secretion in CD4(+) T cells. *Immunity*, 39(5):846–857, November 2013.

[103] Arianne C. Richard, Aaron T. L. Lun, Winnie W. Y. Lau, Berthold Gttgens, John C. Marioni, and Gillian M. Griffiths. T cell cytolytic capacity is independent of initial stimulation strength. *Nature Immunology*, 19(8):849–858, 2018.

[104] Lara M. Kingeter, Suman Paul, Sean K. Maynard, Natalia G. Cartwright, and Brian C. Schaefer. Cutting edge: TCR ligation triggers digital activation of NF-kappaB. *Journal of Immunology (Baltimore, Md.: 1950)*, 185(8):4520–4524, October 2010.

[105] Qi Qiao and Hao Wu. Supramolecular organizing centers (SMOCs) as signaling machines in innate immune activation. *Science China. Life Sciences*, 58(11):1067–1072, November 2015.

[106] Andrew G. York, Panagiotis Chandris, Damian Dalle Nogare, Jeffrey Head, Peter Wawrzusin, Robert S. Fischer, Ajay Chitnis, and Hari Shroff. Instant super-resolution imaging in live cells and embryos via analog image processing. *Nature Methods*, 10(11):1122–1126, November 2013.

[107] Hui Xu, Xiaojing He, Hui Zheng, Lily J. Huang, Fajian Hou, Zhiheng Yu, Michael Jason de la Cruz, Brian Borkowski, Xuewu Zhang, Zhijian J. Chen, and Qiu-Xing Jiang. Structural basis for the prion-like MAVS filaments in antiviral innate immunity. *eLife*, 3:e01489, January 2014.

[108] Alvin Lu, Venkat Giri Magupalli, Jianbin Ruan, Qian Yin, Maninjay K. Atianand, Matthijn R. Vos, Gunnar F. Schrder, Katherine A. Fitzgerald, Hao Wu, and Edward H. Egelman. Unified polymerization mechanism for the assembly of ASC-dependent inflammasomes. *Cell*, 156(6):1193–1206, March 2014.

[109] Martin C. Moncrieffe, Daniel Bollschweiler, Bing Li, Pawel A. Penczek, Lee Hopkins, Clare E. Bryant, David Klenerman, and Nicholas J. Gay. MyD88 Death-Domain Oligomerization Determines Myddosome Architecture: Implications for Toll-like Receptor Signaling. *Structure (London, England: 1993)*, 28(3):281–289.e3, March 2020.

[110] Michal Caspi Tal, Miwa Sasai, Heung Kyu Lee, Brian Yordy, Gerald S. Shadel, and Akiko Iwasaki. Absence of autophagy results in reactive oxygen species-dependent amplification of RLR signaling. *Proceedings of the National Academy of Sciences of the United States of America*, 106(8):2770–2775, February 2009.

[111] Chong-Shan Shi, Kevin Shenderov, Ning-Na Huang, Juraj Kabat, Mones Abu-Asab, Katherine A. Fitzgerald, Alan Sher, and John H. Kehrl. Activation of autophagy by inflammatory signals limits IL-1 production by targeting ubiquitinated inflammasomes for destruction. *Nature Immunology*, 13(3):255–263, January 2012.

[112] Takeshi Into, Toshi Horie, Megumi Inomata, Jin Gohda, Jun-Ichiro Inoue, Yukitaka Murakami, and Shumpei Niida. Basal autophagy prevents autoactivation or enhancement of inflammatory signals by targeting monomeric MyD88. *Scientific Reports*, 7(1):1009, 2017.

[113] Zhangyuan Yin, Clarence Pascual, and Daniel J. Klionsky. Autophagy: machinery and regulation. *Microbial Cell (Graz, Austria)*, 3(12):588–596, December 2016.

[114] A. Goldbeter, G. Dupont, and M. J. Berridge. Minimal model for signal-induced Ca2+ oscillations and for their frequency encoding through protein phosphorylation. *Proceedings of the National Academy of Sciences*, 87(4):1461–1465, February 1990.

[115] Maria K. Traver, Suman Paul, and Brian C. Schaefer. T Cell Receptor Activation of NF-B in Effector T Cells: Visualizing Signaling Events Within and Beyond the Cytoplasmic Domain of the Immunological Synapse. *Methods in Molecular Biology (Clifton, N.J.)*, 1584:101–127, 2017.

[116] Harry Blum. A Transform for Extracting New Descriptors of Shape. pages 362–380, 1967.

[117] Philip Kollmannsberger, Michael Kerschnitzki, Felix Repp, Wolfgang Wagermaier, Richard Weinkamer, and Peter Fratzl. The small world of osteocytes: connectomics of the lacuno-canalicular network in bone. *New Journal of Physics*, 19(7):073019, July 2017.

[118] Mohit Kumar, Mario S. Mommer, and Victor Sourjik. Mobility of cytoplasmic, membrane, and DNA-binding proteins in Escherichia coli. *Biophysical Journal*, 98(4):552–559, February 2010.

[119] Jan Mller and Michael Sixt. Cell Migration: Making the Waves. *Current Biology*, 27(1):R24–R25, January 2017.

[120] Naoyuki Inagaki and Hiroko Katsuno. Actin Waves: Origin of Cell Polarization and Migration? *Trends in Cell Biology*, 27(7):515–526, July 2017.

[121] Dennis E. Discher, Paul Janmey, and Yu-li Wang. Tissue Cells Feel and Respond to the Stiffness of Their Substrate. *Science*, 310(5751):1139–1143, November 2005.

[122] Andrew D. Doyle, Francis W. Wang, Kazue Matsumoto, and Kenneth M. Yamada. One-dimensional topography underlies three-dimensional fibrillar cell migration. *The Journal of Cell Biology*, 184(4):481–490, February 2009.

[123] Pengfei Lu, Valerie M. Weaver, and Zena Werb. The extracellular matrix: A dynamic niche in cancer progression. *J Cell Biol*, 196(4):395–406, February 2012.

[124] Ryan J. Petrie and Kenneth M. Yamada. Fibroblasts Lead the Way: A Unified View of 3D Cell Motility. *Trends in Cell Biology*, 25(11):666–674, November 2015.

[125] Orion D Weiner, William A Marganski, Lani F Wu, Steven J Altschuler, and Marc W Kirschner. An Actin-Based Wave Generator Organizes Cell Motility. *PLoS Biology*, 5(9), September 2007.

[126] Maurizio Ventre, Carlo Fortunato Natale, Carmela Rianna, and Paolo Antonio Netti. Topographic cell instructive patterns to control cell adhesion, polarization and migration. *Journal of The Royal Society Interface*, 11(100):20140687, November 2014.

[127] Xiaoyu Sun, Matt J. Hourwitz, Eleni M. Baker, B. U. Sebastian Schmidt, Wolfgang Losert, and John T. Fourkas. Replication of biocompatible, nanotopographic surfaces. *Scientific Reports*, 8(1):564, January 2018.

[128] Katarina Wolf and Peter Friedl. Extracellular matrix determinants of proteolytic and non-proteolytic cell migration. *Trends in Cell Biology*, 21(12):736–744, December 2011.

[129] Guillaume Charras and Erik Sahai. Physical influences of the extracellular environment on cell migration. *Nature Reviews Molecular Cell Biology*, 15(12):813–824, December 2014. Number: 12 Publisher: Nature Publishing Group.

[130] Michael Melak, Matthias Plessner, and Robert Grosse. Actin visualization at a glance. *Journal of Cell Science*, 130(3):525–530, February 2017. Publisher: The Company of Biologists Ltd Section: CELL SCIENCE AT A GLANCE.

[131] John C. Crocker and David G. Grier. Methods of Digital Video Microscopy for Colloidal Studies. *Journal of Colloid and Interface Science*, 179(1):298–310, April 1996.

[132] W. H. Meyer and T. H. Howard. Actin polymerization and its relationship to locomotion and chemokinetic response in maturing human promyelocytic leukemia cells. *Blood*, 70(2):363–367, August 1987.

[133] Mikheil Azatov, Xiaoyu Sun, Alexandra Suberi, John T. Fourkas, and Arpita Upadhyaya. Topography on a subcellular scale modulates cellular adhesions and actin stress fiber dynamics in tumor associated fibroblasts. *Physical Biology*, 14(6):065003, 2017.

[134] I. Begemann, T. Saha, L. Lamparter, I. Rathmann, D. Grill, L. Golbach, C. Rasch, U. Keller, B. Trappmann, M. Matis, V. Gerke, J. Klingauf, and M. Galic. Mechanochemical self-organization determines search pattern in migratory cells. *Nature Physics*, 15(8):848–857, August 2019. Number: 8 Publisher: Nature Publishing Group.

[135] Viola Vogel and Michael Sheetz. Local force and geometry sensing regulate cell functions. *Nature Reviews Molecular Cell Biology*, 7(4):265–275, April 2006. Number: 4 Publisher: Nature Publishing Group.

[136] Harvey T. McMahon and Emmanuel Boucrot. Membrane curvature at a glance. *Journal of Cell Science*, 128(6):1065–1070, March 2015.

[137] Andrew A. Bridges, Maximilian S. Jentzsch, Patrick W. Oakes, Patricia Occhipinti, and Amy S. Gladfelter. Micron-scale plasma membrane curvature is recognized by the septin cytoskeleton. *The Journal of Cell Biology*, 213(1):23–32, April 2016.

[138] Joshua Zimmerberg and Stuart McLaughlin. Membrane curvature: how BAR domains bend bilayers. *Current biology: CB*, 14(6):R250–252, March 2004.

[139] Brian R. Graziano and Orion D. Weiner. Self-organization of protrusions and polarity during eukaryotic chemotaxis. *Current Opinion in Cell Biology*, 30:60–67, October 2014.

[140] H. Miki, H. Yamaguchi, S. Suetsugu, and T. Takenawa. IRSp53 is an essential intermediate between Rac and WAVE in the regulation of membrane ruffling. *Nature*, 408(6813):732–735, December 2000.

[141] Bianca Habermann. The BAR-domain family of proteins: a case of bending and binding? *EMBO reports*, 5(3):250–255, March 2004.

[142] M. J. Dalby, M. O. Riehle, D. S. Sutherland, H. Agheli, and A. S. G. Curtis. Morphological and microarray analysis of human fibroblasts cultured on nanocolumns produced by colloidal lithography. *European Cells & Materials*, 9:1–8; discussion 8, January 2005.

[143] Christopher N. LaFratta, John T. Fourkas, Tommaso Baldacchini, and Richard A. Farrer. Multiphoton Fabrication. *Angewandte Chemie International Edition*, 46(33):6238–6258, 2007. _eprint: https://onlinelibrary.wiley.com/doi/pdf/10.1002/anie.200603995.

[144] Linjie Li and John T. Fourkas. Multiphoton polymerization. *Materials Today*, 10(6):30–37, June 2007.

[145] Eero P Simoncelli, Edward H Adelson, and David J Heeger. Probability distributions of optical flow. 1991.

[146] J. L. Barron, D. J. Fleet, and S. S. Beauchemin. Performance of optical flow techniques. *International Journal of Computer Vision*, 12(1):43–77, February 1994.

[147] Peter Friedl and Katarina Wolf. Tumour-cell invasion and migration: diversity and escape mechanisms. *Nature Reviews Cancer*, 3(5):362–374, May 2003.

[148] Hisashi Haga, Chikako Irahara, Ryo Kobayashi, Toshiyuki Nakagaki, and Kazushige Kawabata. Collective movement of epithelial cells on a collagen gel substrate. *Biophysical Journal*, 88(3):2250–2256, March 2005.

[149] Laurent Blanchoin, Rajaa Boujemaa-Paterski, Ccile Sykes, and Julie Plastino. Actin dynamics, architecture, and mechanics in cell motility. *Physiological Reviews*, 94(1):235–263, January 2014.

[150] Laurent Bozec, Gert van der Heijden, and Michael Horton. Collagen Fibrils: Nanoscale Ropes. *Biophysical Journal*, 92(1):70–75, January 2007.

[151] Tobias P. Kunzler, Christoph Huwiler, Tanja Drobek, Janos Vrs, and Nicholas D. Spencer. Systematic study of osteoblast response to nanotopography by means of nanoparticle-density gradients. *Biomaterials*, 28(33):5000–5006, November 2007.

[152] Chuan-Hsiang Huang, Ming Tang, Changji Shi, Pablo A. Iglesias, and Peter N. Devreotes. An excitable signal integrator couples to an idling cytoskeletal oscillator to drive cell migration. *Nature Cell Biology*, 15(11):1307–1316, November 2013. Number: 11 Publisher: Nature Publishing Group.

[153] William M. Bement, Marcin Leda, Alison M. Moe, Angela M. Kita, Matthew E. Larson, Adriana E. Golding, Courtney Pfeuti, Kuan-Chung Su, Ann L. Miller, Andrew B. Goryachev, and George vonDassow. Activatorinhibitor coupling between Rho signalling and actin assembly makes the cell cortex an excitable medium. *Nature Cell Biology*, 17(11):1471–1483, November 2015. 00066.

[154] Gnther Gerisch. Self-organizing actin waves that simulate phagocytic cup structures. *PMC Biophysics*, 3(1):7, March 2010.

[155] Jun Allard and Alex Mogilner. Traveling waves in actin dynamics and cell motility. *Current Opinion in Cell Biology*, 25(1):107–115, February 2013.

[156] GillianL. Ryan, HeatherM. Petroccia, Naoki Watanabe, and Dimitrios Vavylonis. Excitable Actin Dynamics in Lamellipodial Protrusion and Retraction. *Biophysical Journal*, 102(7):1493–1502, April 2012.

[157] Gillian L. Ryan, Naoki Watanabe, and Dimitrios Vavylonis. A review of models of fluctuating protrusion and retraction patterns at the leading edge of motile cells. *Cytoskeleton*, 69(4):195–206, 2012. _eprint: https://onlinelibrary.wiley.com/doi/pdf/10.1002/cm.21017.

[158] Sayak Bhattacharya and Pablo A. Iglesias. The Regulation of Cell Motility Through an Excitable Network. *IFAC-PapersOnLine*, 49(26):357–363, January 2016.

[159] Peter J. M. van Haastert, Ineke Keizer-Gunnink, and Arjan Kortholt. Coupled excitable Ras and F-actin activation mediates spontaneous pseudopod formation and directed cell movement. *Molecular Biology of the Cell*, 28(7):922–934, April 2017.

[160] Sayak Bhattacharya and Pablo A. Iglesias. The threshold of an excitable system serves as a control mechanism for noise filtering during chemotaxis. *PLOS ONE*, 13(7):e0201283, July 2018. Publisher: Public Library of Science.

[161] Till Bretschneider, Stefan Diez, Kurt Anderson, John Heuser, Margaret Clarke, Annette Mller-Taubenberger, Jana Khler, and Gnther Gerisch. Dynamic Actin Patterns and Arp2/3 Assembly at the Substrate-Attached Surface of Motile Cells. *Current Biology*, 14(1):1–10, January 2004.

[162] Gnther Gerisch, Till Bretschneider, Annette Mller-Taubenberger, Evelyn Simmeth, Mary Ecke, Stefan Diez, and Kurt Anderson. Mobile Actin Clusters and Traveling Waves in Cells Recovering from Actin Depolymerization. *Biophysical Journal*, 87(5):3493–3503, November 2004.

[163] Michael Brenner and Stephen D. Thoms. Caffeine blocks activation of cyclic AMP synthesis in Dictyostelium discoideum. *Developmental Biology*, 101(1):136–146, January 1984.

[164] Ikuko Fujiwara, Mark E. Zweifel, Naomi Courtemanche, and Thomas D. Pollard. Latrunculin A Accelerates Actin Filament Depolymerization in Addition to Sequestering Actin Monomers. *Current Biology*, 28(19):3183–3192.e2, October 2018.

[165] Jan Faix and Klemens Rottner. The making of filopodia. *Current Opinion in Cell Biology*, 18(1):18–25, February 2006.

[166] Hyewon Kang, Jiyeon Lee, Joonhyung Park, and Hong H. Lee. An improved method of preparing composite poly(dimethylsiloxane) moulds. *Nanotechnology*, 17(1):197–200, December 2005. Publisher: IOP Publishing.

[167] Olga Ilina, Leonard Campanello, Pavel G. Gritsenko, Manon Vullings, Chenlu Wang, Peter Bult, Wolfgang Losert, and Peter Friedl. Intravital microscopy of collective invasion plasticity in breast cancer. *Disease Models & Mechanisms*, page dmm.034330, January 2018.

[168] Kevin J. Cheung and Andrew J. Ewald. A collective route to metastasis: Seeding by tumor cell clusters. *Science*, 352(6282):167–169, April 2016. Publisher: American Association for the Advancement of Science Section: Perspective.

[169] Arianna Fumagalli, Jarno Drost, Saskia J. E. Suijkerbuijk, Ruben van Boxtel, Joep de Ligt, G. Johan Offerhaus, Harry Begthel, Evelyne Beerling, Ee Hong Tan, Owen J. Sansom, Edwin Cuppen, Hans Clevers, and Jacco van Rheenen. Genetic dissection of colorectal cancer progression by orthotopic transplantation of engineered cancer organoids. *Proceedings of the National Academy of Sciences*, 114(12):E2357–E2364, March 2017. Publisher: National Academy of Sciences Section: PNAS Plus.

[170] Silvia Giampieri, Cerys Manning, Steven Hooper, Louise Jones, Caroline S. Hill, and Erik Sahai. Localized and reversible TGF signalling switches breast cancer cells from cohesive to single cell motility. *Nature Cell Biology*, 11(11):1287–1296, November 2009. Number: 11 Publisher: Nature Publishing Group.

[171] Dmitriy Kedrin, Bojana Gligorijevic, Jeffrey Wyckoff, Vladislav V. Verkhusha, John Condeelis, Jeffrey E. Segall, and Jacco van Rheenen. Intravital imaging of metastatic behavior through a mammary imaging window. *Nature Methods*, 5(12):1019–1021, December 2008. Number: 12 Publisher: Nature Publishing Group.

[172] Peter Friedl and Stephanie Alexander. Cancer Invasion and the Microenvironment: Plasticity and Reciprocity. *Cell*, 147(5):992–1009, November 2011.

[173] Allison S. Harney, Esther N. Arwert, David Entenberg, Yarong Wang, Peng Guo, Bin-Zhi Qian, Maja H. Oktay, Jeffrey W. Pollard, Joan G. Jones, and John S. Condeelis. Real-Time Imaging Reveals Local, Transient Vascular Permeability, and Tumor Cell Intravasation Stimulated by TIE2hi MacrophageDerived VEGFA. *Cancer Discovery*, 5(9):932–943, September 2015. Publisher: American Association for Cancer Research Section: Research Articles.

[174] P. Bronsert, K. EnderleAmmour, M. Bader, S. Timme, M. Kuehs, A. Csanadi, G. Kayser, I. Kohler, D. Bausch, J. Hoeppner, U. T. Hopt, T. Keck, E. Stickeler, B. Passlick, O. Schilling, C. P. Reiss, Y. Vashist, T. Brabletz, J. Berger, J. Lotz, J. Olesch, M. Werner, and U. F. Wellner. Cancer cell invasion and EMT marker expression: a three-dimensional study of the human cancer-host interface. *The Journal of Pathology*, 234(3):410–422, 2014. _eprint: https://onlinelibrary.wiley.com/doi/pdf/10.1002/path.4416.

[175] KevinJ. Cheung, Edward Gabrielson, Zena Werb, and AndrewJ. Ewald. Collective Invasion in Breast Cancer Requires a Conserved Basal Epithelial Program. *Cell*, 155(7):1639–1651, December 2013.

[176] Antoine A. Khalil, Olga Ilina, Pavlo G. Gritsenko, Peter Bult, Paul N. Span, and Peter Friedl. Collective invasion in ductal and lobular breast cancer associates with distant metastasis. *Clinical & Experimental Metastasis*, 34(6):421–429, October 2017.

[177] Nicola Aceto, Aditya Bardia, DavidT. Miyamoto, MariaC. Donaldson, BenS. Wittner, JoelA. Spencer, Min Yu, Adam Pely, Amanda Engstrom, Huili Zhu, BrianW. Brannigan, Ravi Kapur, ShannonL. Stott, Toshi Shioda, Sridhar Ramaswamy, DavidT. Ting, CharlesP. Lin, Mehmet Toner, DanielA. Haber, and Shyamala Maheswaran. Circulating Tumor Cell Clusters Are Oligoclonal Precursors of Breast Cancer Metastasis. *Cell*, 158(5):1110–1122, August 2014.

[178] Kevin J. Cheung, Veena Padmanaban, Vanesa Silvestri, Koen Schipper, Joshua D. Cohen, Amanda N. Fairchild, Michael A. Gorin, James E. Verdone, Kenneth J. Pienta, Joel S. Bader, and Andrew J. Ewald. Polyclonal breast cancer metastases arise from collective dissemination of keratin 14-expressing tumor cell clusters. *Proceedings of the National Academy of Sciences*, 113(7):E854–E863, February 2016. Publisher: National Academy of Sciences Section: PNAS Plus.

[179] Bojana Gligorijevic, Aviv Bergman, and John Condeelis. Multiparametric Classification Links Tumor Microenvironments with Tumor Cell Phenotype. *PLoS Biology*, 12(11), November 2014.

[180] Dmitriy Kedrin, Jeffrey Wyckoff, Erik Sahai, John Condeelis, and Jeffrey E. Segall. Imaging tumor cell movement in vivo. *Current Protocols in Cell Biology*, Chapter 19:Unit 19.7, June 2007.

[181] Syster Hofmeyer, Gyula Pekr, Mria Gere, Mikls Tarjn, Dan Hellberg, and Tibor Tot. Comparison of the Subgross Distribution of the Lesions in Invasive Ductal and Lobular Carcinomas of the Breast: A Large-Format Histology Study, October 2012. ISSN: 2090-3170 Library Catalog: www.hindawi.com Pages: e436141 Publisher: Hindawi Volume: 2012.

[182] Virginie Firlej, Franck Ladam, Guillaume Brysbaert, Patrick Dumont, Franois Fuks, Yvan de Launoit, Arndt Benecke, and Anne Chotteau-Lelievre. Reduced tumorigenesis in mouse mammary cancer cells following inhibition of Pea3- or Erm-dependent transcription. *Journal of Cell Science*, 121(20):3393–3402, October 2008. Publisher: The Company of Biologists Ltd Section: Research Article.

[183] Cristina Hidalgo-Carcedo, Steven Hooper, Shahid I. Chaudhry, Peter Williamson, Kevin Harrington, Birgit Leitinger, and Erik Sahai. Collective cell migration requires suppression of actomyosin at cellcell contacts mediated by DDR1 and the cell polarity regulators Par3 and Par6. *Nature Cell Biology*, 13(1):49–59, January 2011. Number: 1 Publisher: Nature Publishing Group.

[184] Guillermo A. Gomez, Robert W. McLachlan, and Alpha S. Yap. Productive tension: force-sensing and homeostasis of cellcell junctions. *Trends in Cell Biology*, 21(9):499–505, September 2011.

[185] Meghan K. Driscoll, Colin McCann, Rael Kopace, Tess Homan, John T. Fourkas, Carole Parent, and Wolfgang Losert. Cell Shape Dynamics: From Waves to Migration. *PLoS Computational Biology*, 8(3), March 2012.

[186] Grgory Giannone, Benjamin J. Dubin-Thaler, Olivier Rossier, Yunfei Cai, Oleg Chaga, Guoying Jiang, William Beaver, Hans-Gnther Dbereiner, Yoav Freund, Gary Borisy, and Michael P. Sheetz. Lamellipodial Actin Mechanically Links Myosin Activity with Adhesion-Site Formation. *Cell*, 128(3):561–575, February 2007.

[187] Bram De Craene and Geert Berx. Regulatory networks defining EMT during cancer initiation and progression. *Nature Reviews Cancer*, 13(2):97–110, February 2013. Number: 2 Publisher: Nature Publishing Group.

[188] Sonia Narendra, Sarah M. Jenkins, Andras Khoor, and Aziza Nassar. Clinical outcome in pleomorphic lobular carcinoma: a case-control study with comparison to classic invasive lobular carcinoma. *Annals of Diagnostic Pathology*, 19(2):64–69, April 2015.

[189] Veronika te Boekhorst, Luigi Preziosi, and Peter Friedl. Plasticity of Cell Migration In Vivo and In Silico. *Annual Review of Cell and Developmental Biology*, 32(1):491–526, 2016. _eprint: https://doi.org/10.1146/annurev-cellbio-111315-125201.

[190] Hailey E. Brighton, Steven P. Angus, Tao Bo, Jose Roques, Alicia C. Tagliatela, David B. Darr, Kubra Karagoz, Noah Sciaky, Michael L. Gatza, Norman E. Sharpless, Gary L. Johnson, and James E. Bear. New Mechanisms of Resistance to MEK Inhibitors in Melanoma Revealed by Intravital Imaging. *Cancer Research*, 78(2):542–557, January 2018. Publisher: American Association for Cancer Research Section: Translational Science.

[191] Eishu Hirata, MariaRomina Girotti, Amaya Viros, Steven Hooper, Bradley Spencer-Dene, Michiyuki Matsuda, James Larkin, Richard Marais, and Erik Sahai. Intravital Imaging Reveals How BRAF Inhibition Generates Drug-Tolerant Microenvironments with High Integrin 1/FAK Signaling. *Cancer Cell*, 27(4):574–588, April 2015.

[192] Yugui Zhang, Jin Zheng, Chi Zhang, and Bo Li. An effective motion object detection method using optical flow estimation under a moving camera. *Journal of Visual Communication and Image Representation*, 55:215–228, August 2018.

[193] Moritz Menze and Andreas Geiger. Object scene flow for autonomous vehicles. In *2015 IEEE Conference on Computer Vision and Pattern Recognition (CVPR)*, pages 3061–3070, June 2015. ISSN: 1063-6919.

[194] Benjamin Allaert, Ioan Marius Bilasco, and Chaabane Djeraba. Consistent Optical Flow Maps for full and micro facial expression recognition. volume 5, pages 235–242. SCITEPRESS - Science and Technology Publications, February 2017.

[195] Jianfeng Zhao, Xia Mao, and Jian Zhang. Learning deep facial expression features from image and optical flow sequences using 3D CNN. *The Visual Computer*, 34(10):1461–1475, October 2018.

[196] Nilesh Gupta, Jeffrey R. Liu, Brijeshkumar Patel, Deepak E. Solomon, Bhuvaneshwar Vaidya, and Vivek Gupta. Microfluidics-based 3D cell culture models: Utility in novel drug discovery and delivery research. *Bioengineering & Translational Medicine*, 1(1):63–81, 2016. _eprint: https://aiche.onlinelibrary.wiley.com/doi/pdf/10.1002/btm2.10013.

[197] Philipp J. Keller, Annette D. Schmidt, Joachim Wittbrodt, and Ernst H. K. Stelzer. Reconstruction of Zebrafish Early Embryonic Development by Scanned Light Sheet Microscopy. *Science*, 322(5904):1065–1069, November 2008. Publisher: American Association for the Advancement of Science Section: Research Article.

[198] Yicong Wu, Peter Wawrzusin, Justin Senseney, Robert S. Fischer, Ryan Christensen, Anthony Santella, Andrew G. York, Peter W. Winter, Clare M. Waterman, Zhirong Bao, Daniel A. Coln-Ramos, Matthew McAuliffe, and Hari Shroff. Spatially isotropic four-dimensional imaging with dual-view plane illumination microscopy. *Nature Biotechnology*, 31(11):1032–1038, November 2013. Number: 11 Publisher: Nature Publishing Group.

[199] Abhishek Kumar, Yicong Wu, Ryan Christensen, Panagiotis Chandris, William Gandler, Evan McCreedy, Alexandra Bokinsky, Daniel A. Coln-Ramos, Zhirong Bao, Matthew McAuliffe, Gary Rondeau, and Hari Shroff. Dual-view plane illumination microscopy for rapid and spatially isotropic imaging. *Nature Protocols*, 9(11):2555–2573, November 2014. Number: 11 Publisher: Nature Publishing Group.

[200] Abhishek Kumar, Ryan Christensen, Min Guo, Panos Chandris, William Duncan, Yicong Wu, Anthony Santella, Mark Moyle, Peter W. Winter, Daniel Coln-Ramos, Zhirong Bao, and Hari Shroff. Using Stage- and Slit-Scanning to Improve Contrast and Optical Sectioning in Dual-View Inverted Light Sheet Microscopy (diSPIM). *The Biological Bulletin*, 231(1):26–39, August 2016. Publisher: The University of Chicago Press.

[201] Meghan K. Driscoll, Erik S. Welf, Andrew R. Jamieson, Kevin M. Dean, Tadamoto Isogai, Reto Fiolka, and Gaudenz Danuser. Robust and automated detection of subcellular morphological motifs in 3D microscopy images. *Nature Methods*, 16(10):1037–1044, 2019.

[202] John L Barron and Neil A Thacker. Tutorial: Computing 2d and 3d optical flow. *Imaging science and biomedical engineering division, medical school, university of manchester*, 1, 2005.

[203] Yuan Xiong, Chuan-Hsiang Huang, Pablo A. Iglesias, and Peter N. Devreotes. Cells navigate with a local-excitation, global-inhibition-biased excitable network. *Proceedings of the National Academy of Sciences of the United States of America*, 107(40):17079–17086, October 2010.

[204] Ted W. Way, Lubomir M. Hadjiiski, Berkman Sahiner, Heang-Ping Chan, Philip N. Cascade, Ella A. Kazerooni, Naama Bogot, and Chuan Zhou. Computer-aided diagnosis of pulmonary nodules on CT scans: Segmentation and classification using 3D active contours. *Medical Physics*, 33(7Part1):2323–2337, 2006. _eprint: https://onlinelibrary.wiley.com/doi/pdf/10.1118/1.2207129.

[205] Akanni Clarke, Philip G. McQueen, Hsiao Yu Fang, Ramakrishnan Kannan, Victor Wang, Evan McCreedy, Stephen Wincovitch, and Edward Giniger. Abl signaling directs growth of a pioneer axon in Drosophila by shaping the intrinsic fluctuations of actin. *Molecular Biology of the Cell*, 31(6):466–477, January 2020. Publisher: American Society for Cell Biology (mboc).

[206] Akanni Clarke, Philip G. McQueen, Hsiao Yu Fang, Ramakrishnan Kannan, Victor Wang, Evan McCreedy, Tyler Buckley, Erika Johannessen, Stephen Wincovitch, and Edward Giniger. Dynamic morphogenesis of a pioneer axon in Drosophila and its regulation by Abl tyrosine kinase. *Molecular Biology of the Cell*, 31(6):452–465, January 2020. Publisher: American Society for Cell Biology (mboc).